Algorithm-driven design of conformal antenna arrays for Ultra-Wideband Direction-Of-Arrival estimation

Iñigo Liberal Olleta

June 11, 2009

Supervisor: Diego Caratelli

Thesis Advisor: Alexander Yarovoy

IRCTR-A-010-09
IRCTR, DELFT UNIVERSITY OF TECHNOLOGY

ABSTRACT

Due to its numerous applications, the problem of Direction-Of-Arrival (DOA) estimation of one or more incoming radio signals has attracted great attention in industrial and scientific research communities. Direction finding systems have been widely employed in civil and military applications, e.g. for navigation. However, due to recent wide spread of wireless technologies, a new broad range of civil applications has been opened. Ideally, radio direction finders (RDFs) should feature a reduced size, whilst still preserving an excellent performance in terms of DOA estimation accuracy, and broadband operation. Hence, the design of a RDF is a cumbersome task that involves several trade-offs. For example, a compact array is highly desirable, but low-frequency operating antennas are usually bulky. Moreover, the size of the array limits the estimation accuracy, and determines the level of antenna mutual coupling potentially resulting in a degradation of the system performance.

This work discusses the design of two RDFs operating in different frequency bands. The proposed design includes antenna modeling, signal processing for DOA estimation, and array calibration.

The elliptically shaped dipole antenna, also called butterfly antenna, is adopted as individual antenna element, due to its ultra-wideband properties, conformal shape, and relatively small size. Two different antennas are designed, one covering the frequency range between 250 and 950MHz, and the other one covering the band from 0.9 to 3.5GHz. An extensive parameter study has been carried out, proving that butterfly antennas feature robust circuital and radiation properties. In addition, a suitable antenna radome is adopted to enhance the front-to-back radiation ratio over the whole operational bandwidth, as well as to increase environmental durability of the structure.

The DOA estimation is performed using the MUSIC algorithm. This signal subspace narrow-band technique is widely used in direction finding applications, and thus makes the proposed system directly comparable with already available RDFs. In addition, MUSIC algorithm is compatible with some classes of wideband DOA estimation techniques, such as the Coherent Signal-Subspace Method (CSSM).

As for the antenna design, a Uniform Circular Array (UCA) configuration is adopted. Such configuration is preferable due to the complete angular coverage in the azimuthal direction. In particular, suitable design guidelines of the array, aimed to the enhancement of the accuracy in DOA estimation, are presented. To this end, physical limitations of the system, such as minimum separation between radio signals, minimum SNR, and maximum detectable number of signals, are properly taken into account.

Mutual coupling and errors in the antenna characteristics degrade severely the system performance. Therefore, array calibration techniques are also studied. Some of preexistent calibration techniques are combined and enhanced, creating a novel calibration technique that includes errors in the antenna characteristics, as well as mutual coupling effects between antenna elements.

ACKNOWLEDGEMENTS

First of, I wish to thank to Diego Caratelli for his excellent mentorship during the course of this thesis. I am really grateful for his advice, help, ideas and especially for being so patient answering all my doubts.

Antes que nada también tengo que darle las gracias a mi familia. Todo el mundo sabe que este trabajo no habría sido posible sin su apoyo incondicional. La verdad es que siempre me dieron más de lo que les pedí.

I would also like to express my gratitude to the people of the IRCTR, who have helped me during these months, and have let me feel part of the group, participating in brainstorms, following courses and visiting conferences.

I have to give especial thanks to the professors Miguel Angel Gomez and Massimiliano Simeoni for helping me with the paperwork and all the preparations that made possible my presence at Delft.

I cannot forget to give thanks to my professors at the Public University of NAvarre. I have employed nine months in developing this thesis, but the results are the consequence of a much more long period. During the past five years I have received not only an excellent technical background, but I have also learnt the meaning of engineering, science, and many other valuable things.

I cannot leave Delft without mentioning all the people that I have met here along this year. There are too many names to be included here, but all of them know that they have been my actual family here, and that I will always remember these months.

Finally, my special thanks go to my girlfriend Marta, whose patience always raised my morale when in need, and was of great help in difficult times.

Contents

Chapter 1

Introduction

1.1 Introduction to Direction Finding

A direction finding (DF) system, also called Radio Direction Finder (RDF), is basically an antenna-receiver combination arranged to determine the Angle Of Arrival (AOA) or Direction Of Arrival (DOA) of a distant emitter. In practice, however, the objective of most DF systems is to determine the location of the emitter. Virtually all DF systems derive the emitter location from an initial determination of the DOA of the received signal. Inversely, it is also possible to find the position of the receiver if the position of one or more emitters is known.

Although the DOA estimation is the core problem of the RDFs, these systems also estimate another parameters such as number of signals, EM field polarization, power, frequency and cross-correlation.

Perhaps, the most popular application of direction finding systems has been navigation, for both maritime and air traffic. However, due to their strategic importance, direction finding systems have been historically related with military applications.

In fact, the use of radio direction finding dates back to World War I, when both the Allies and the forces of the Central Powers used it to locate enemy positions on the ground. From this moment, RDF have been present in every army, taking more importance day by day, going from locating enemy positions to being able to identify number and positions of enemies, and track missiles. Direction finding reached one of its highest points during the Cold War, where a large worldwide network, called Iron Horse, was built.

Nowadays, anti-jamming systems, enemies location, missile guidance and missile detection are some of the potential military applications of RDFs.

However, the recent popularization of all sort of wireless applications is creating the demand of these systems for many civil applications. First of, the electromagnetic spectra is scarce, and is regulated by a license-based system. Therefore, Direction Finding systems are needed to control and locate illegal, secret or hostile transmitters.

Moreover, the DOA estimation presents a powerful combination with beamforming. On one hand, it is possible to increase the data rate of a transmission between several emitters creating independent spatial channels. On the other hand, the knowledge of the DOA and other characteristics of the incoming signals can enhanced the quality of the transmission in difficult environments such as multipath channels and scenarios with strong interference sources.

Last but not least, nowadays almost everybody has a wireless terminal in his pocket (for instance, mobile phone), which is constantly emitting electromagnetic radiation. Hence, the Direction Finding systems can be a very helpful tool in disaster response, locating victims...

Therefore, a list with some of the potential DF applications could be:

- Military applications
- Navigation
- Location of illegal, secret or hostile transmitters
- Disaster response
- Transmission in multipath/strong interference channels
- Wildlife tracking
- Sport
- ...

However, the design of direction finders is a cumbersome task. Firstly, a mobile DF system requires size and weight constraints, but at the same time, covering a wide bandwidth requires several subarrays, involving large antennas to cover the lowest frequency bands. Furthermore, it is necessary to employ large array with an elevated number of elements for an accurate detection of several signals.

Moreover, DF systems are usually installed in external surfaces, so strong and relative big structures are needed in order to maintain correct orientation and avoid damage caused by the environmental conditions and extreme driving. However, these structures suffer from electromagnetic coupling with the antennas, which is an important source of error, and metallic structures are easily detected by radar, so big structures should be avoided.

1.2 Overview of direction finding systems

Radio Direction Finders may be classified in two different types: manual direction finders and fixed antenna direction finders.

Manual direction finders are performed by rotating a highly directional antenna while the operator listens for a null. Minimum signal (ideally null) is preferred because transitions are stronger at this point, so it is desirable to have an antenna with a cardioid (heart-shaped) radiation pattern, see figure 1.1. It is the simplest direction finding system, but a motor is needed, and once a target is identified, the system is blind to other ones.

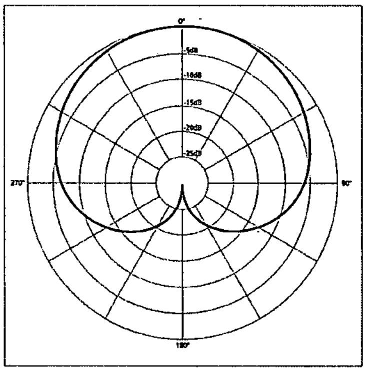

Figure 1.1: Heart shaped radiation pattern, it shows strong transitions around the null.

These are the simplest and most primitive systems. The first systems were built with horizontal dipoles and loops, although loops were more used because vertical polarization was more popular in that time. These antennas have a cosine shaped radiation pattern, that in combination with an omnidirectional antenna, are able to create the cardioid pattern. However, loop systems have errors in the presence of horizontal polarization, so they are mainly useful for low frequencies, where a surface waves dominate the transmission, and the horizontal component is absorbed by the ground. One loop antenna and its radiation pattern is shown in figure 1.2

The natural evolution of these antennas is the Adcock antenna (figure 1.3). Two dipoles, spaced a fraction of a wavelength apart, are connected so that their voltages, have the desired cosine polar diagram, which only respond to vertical polarization. Unfortunately, horizontal connecting feeding is a source of error with horizontal polarization. Updates that solve this problem are the Buried-U Adcock, Elevated-H Adcock and Balanced Coupled Adcock antenna.

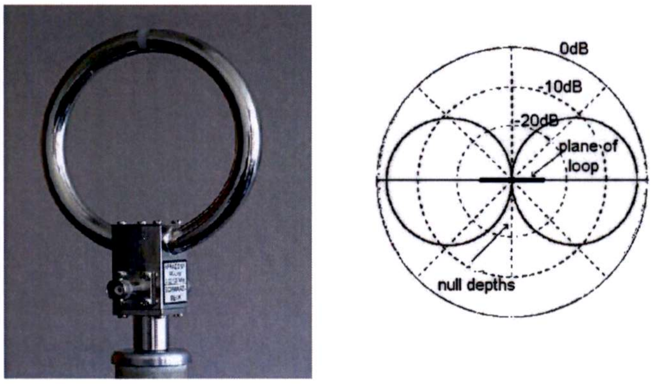

Figure 1.2: a) Loop antenna. b) Cosine radiation pattern.

Figure 1.3: Adcock antenna

Nowadays, there are wireless transmissions of different polarization, so current manual direction finders include rotating highly directional arrays and crossed loops. However, since simultaneous tracking of multiple signals is desirable and moving big antennas is difficult, fixed antenna direction finders are preferred.

The fixed antenna direction finders exist since the beginning of the twentieth century. The first fixed antenna RDF was invented by Bellini-Tosi and popularly called goniometer. The goniometer is composed by two fixed, perpendicular loops, so components that are function of the sine and cosine of the angle of arrival are collected. In order to recombine these components, two coils are mounted at right angles on a common axis, and a third coil that can be rotated inside the other two. The design of the coils is such that the voltage induced in the rotating coil by a given current in either of the fixed coils is proportional to the cosine of the angle between the fixed and rotating coils.

Based in the goniometer idea two popular antennas were developed, the Adcock Watson-Watt and the Wullenweber antennas (figure 1.4).

Nowadays, fixed antenna direction finders performed with antennas arrays are the most popular technology in DF systems. They have a high degree of accuracy for targeting or aiming purposes and offer the possibility of tracking several signals simultaneously. There are two basic groups of antenna arrays in current use: parallel-beam or high probability systems and switched beams or directed systems.

Figure 1.4: Wullenweber antenna, placed at Imperial Beach California in 1964.

Parallel-beam or high probability systems

Parallel-beam systems are distinguished by the fact that all the beams of the DF system exist in all instants of time. Therefore, the antenna system provides an instantaneous angular coverage equal to its field of view, offering the advantage of high intercept probability.

Signal processing techniques must be implemented in order to resolve the DOA of the incoming signals, due to the importance of DF finding applications, diverse DOA estimation algorithms have been extensively studied: Bartlett, Capon, Linear Prediction, Maximum entropy, Pisarenko harmonic decomposition, Minimum norm, Maximum Likelihood, Music, Root-MUSIC, ESPRIT. Between them MUSIC (Multiple Signal Classification) and ESPRIT (Estimation of Signal Parameters via Rotational Invariance Techniques) are the most popular, they are called superresolution algorithms, and are able to track several signals simultaneously, even if signals are spaced less than an antenna beamwidth, but the array must have more antennas than incoming signals.

Different array structures have been implemented in DF systems: linear, X, Y, L shaped, circular, dual ring, dual spiral... However, circular arrays are, in general, preferred. They provide potential advantages like 360º vision with constant performance, equal radiation coupling and the minimum coupling between the antenna and the supporting mast. Furthermore, they present the best performance, in terms of Cramer Rao Bound, in a comparative studio normalizing both array aperture and number of elements with other structures. In general, several subarrays are needed to cover all the required bandwidth, forming a cylindrical array.

Switched beams or directed systems

The directed beam group provides a single narrow high-gain beam that can be steered or pointed in a given direction either as part of planned scanning process such as a raster scan, randomly as a function of time, or in accordance with a frequency program based upon knowledge of an expected return. In general, the steered-beam approach can be made to provide sufficient gain to look into the back lobes of emitters, which compensates, in part for the reduced probability of detection due to the scanning process.

The beam scanning is commonly created with a phased array, but it requires expensive electronics and sophisticated algorithms to control the beam. there are other low cost options like using switched parasitic antennas (SPA). With high-speed Pin diode you can connect/disconnect the parasitic elements from the ground, varying the radiation pattern.

However, antenna arrays fixed direction finders have several drawbacks. Antenna arrays have strict spatial requirements and mutual coupling problems. In fact, mutual coupling between the array elements and the body structure (e.g. mast and arms) is a critical problem, specially when superresolution algorithms are involved. Calibration tests that obtain a true manifold of the array, including coupling between the antennas and scattering in the neighborhood, are use to solve this problem. Other techniques try to avoid these interferences, like the use of EBG substrates in order to eliminate the surface waves.

Although antenna arrays are the most popular of the fixed antenna direction finders, there is an alternative system called mode based direction finding. In mode based direction finding it is possible to determine the DOAS of the incoming signals by exploiting the directional properties of the higher order modes of the antenna. Since only one antenna element is used, the spatial requirements of an array of elements is are avoided as well as problems with mutual coupling between antenna elements. However, the performance of these systems is typically worse than antenna array, so they are not widely employed. The figure 1.5 shows a biconical antenna and its microwave circuitry employed in mode-based DOA estimation.

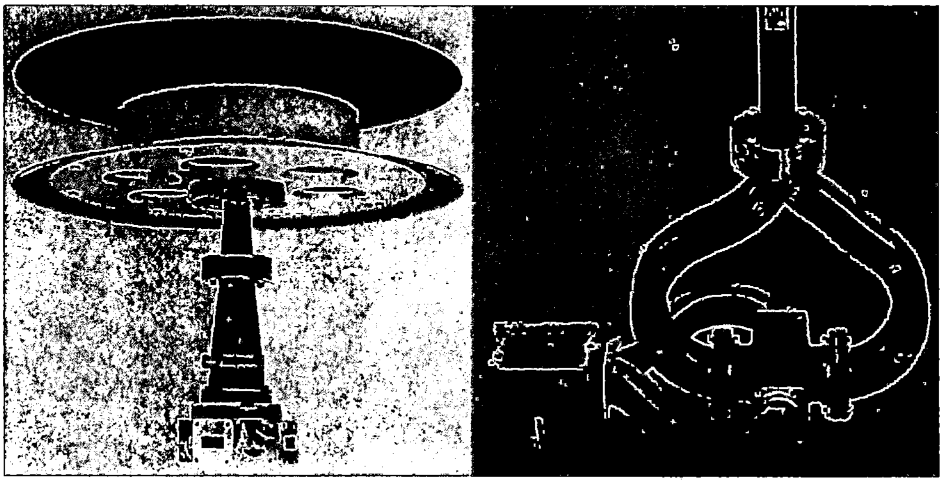

Figure 1.5: a) Biconical antenna. b) Microwave circuitry.

1.3 Antenna elements for direction finding

The antenna is the basic element of the DF system. It has a direct impact in the accuracy, and imposes the first limits to the system performance. Therefore, the design of the single antenna element is a difficult task with a great impact in the overall system performance.

However, the design of the single antenna element for Direction Finding systems is a cumbersome task, that involves many trade-offs. First of, large antennas are needed to cover low frequencies, but at the same time small antennas are needed to satisfy the size and weight restrictions of mobile units. Since it is interesting to cover as much bandwidth as possible, it is desirable an ultra-wideband behavior that avoids the use of excessive subarrays.

A directive radiation pattern can improve the accuracy in the DOA estimation and avoid coupling between the array elements and supporting structure. In spite of this, an excessive directive radiation pattern can limit the range of angles where the signals are detectable, specially in elevation, or present a certain number of blind angles. Furthermore, a frequency independent radiation pattern is also desirable.

A low dispersion profile is very helpful in the estimation of wideband signals. However, it is not mandatory for narrow-band processing. Moreover, the incoming signals can be diversely polarized so it is desirable an antenna that supports both horizontal and vertical polarization.

As anticipated, the first antennas used in DF were loops and dipoles, and their use lasted many years, and even RDF amateurs are using it nowadays. Loop and dipoles are a compact and cheap solution, that can present a good performance for some narrowband and low frequency applications. However, they cannot support broadband and multi-polarization requirements.

In spite of this, there have been a few attempts to improve the dipole performance, such as the composite dipole. The composite dipole is typically compound by a long dipole, a short dipole and the inner wire which provides the separation between them. If the short and long dipole are designed at the frequencies of interest, the system is improved without a dramatical increment in the size of the system.

However, the commercial direction finders cover bandwidths from tenths of MHz to several GHz, depending on the size restrictions, performance... In order to avoid massive arrays, ultra-wideband antennas must be employed. For a complete vision of the subject, an overview of the UWB antennas is included.

As introduced by Schantz [10], UWB antennas can be classified in four different groups: frequency-independent antennas, horn antennas, reflector antennas and small element-antennas.

Frequency-independent antennas

Frequency-independent antennas rely on a variation in geometry from a smaller-scale portion to a large-scale portion. The smaller-scale portion contributes to higher frequencies while the larger-scale portion contributes to lower frequencies. Because the effective source of the radiated field varies with frequency, these antennas tend to be dispersive. Examples of frequency independent antennas include spiral, log periodic, and conical spiral antennas. Figure 1.6 shows spiral antennas used in DF applications.

The dispersive nature of the frequency-independent antennas has limited its use in most of the UWB applications. In spite of this, most of the DF systems are based in narrow-band DOA estimation, and these antenna have been widely employed there.

Figure 1.6: Spiral antennas for missile guidance used in the Shrike missile program

Horn antennas

A horn antenna is an electromagnetic funnel concentrating energy in a particular direction. Horn antennas tend to have high gain and relatively narrow beams, presenting the usual trade-off between directionality and field of view. Horn antennas also tend to be relatively large, often a wavelength or more in dimension at a typical operating frequency. These antennas are well suited for point-to-point links or other applications where a narrow field of view is desired. Examples included Bose's original horn antennas (conical and pyramidal), and the coaxial tapered horns of Brillouin.

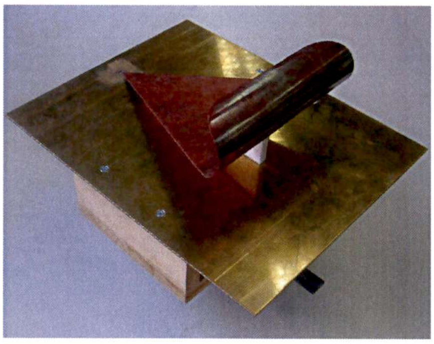

Figure 1.7: UWB horn antenna. The antenna include a rolled termination to avoid reflections and diffraction

Reflector antennas

A reflector antenna also concentrates energy in a particular direction. Also like horn antennas, they tend to have high gain and are relatively large. Reflector antennas tend to be structurally simpler than horn antennas and easier to modify and adjust by manipulating antenna feed. Planar, corner and parabolic cylinder are some of the simplest and easiest options to implement reflector antennas.

Both reflector and horn antennas present excellent UWB properties. However, its large size complicates its integration in circular arrays. Moreover, although a very directive radiation pattern yields in a higher resolution of the DOA estimation, an excessively narrow beam could limit the range of detectable DOAs.

Small-element antennas

These antennas tend to be small, omnidirectional antennas well suited for some commercial applications. There is a variety of small element antennas, magnetic and electric antennas.

Small-element magnetic antennas are physical realizations of an ideal Hertzian dipole, which yields an omnidirectional horizontal polarization pattern. These antennas involve one or more current loops. Magnetic antennas may be thought of as a current driven and have predominantly magnetic fields. Since electric fields tend to couple more strongly to nearby objects, magnetic antennas are better suited for embedded applications.

This family of small-element antennas includes large current radiators (LCR), monoloops, loops, and slot antennas. However, this antennas have difficulty in achieving low-dispersion, omnidirectional patterns. Although a omnidirectional pattern is not needed in DF, low dispersion can be desirable, so small electric small-element antennas seem to be best candidates. An example of small magnetic UWB antenna is presented in figure 1.8.

Small-element electric antennas are some of the most important UWB antennas, because they combine compact size, good impedance bandwidth and omnidirectional pattern useful in a wide variety of consumer electronics and other applications. Small element antennas can be classified in conical, monopole and dipole antennas.

Conical antennas are among the oldest of UWB small-element antennas having been pioneered by Lodge in the 1890s. This family includes biconical, monocone and discone antennas. However, although discone antennas present a multi-octave impedance bandwidth, they cannot support more than one octave radiation pattern. So biconical and monocone are preferred.

Owing to their broadband behavior (a one-wavelength-diameter biconical antenna can offers a excellent matching over a 6:1 range of frequencies), these antennas have been employed in DF applications with some modifications. As it is shown in the figure 1.9, monocone antennas have been employed in DOA estimations.

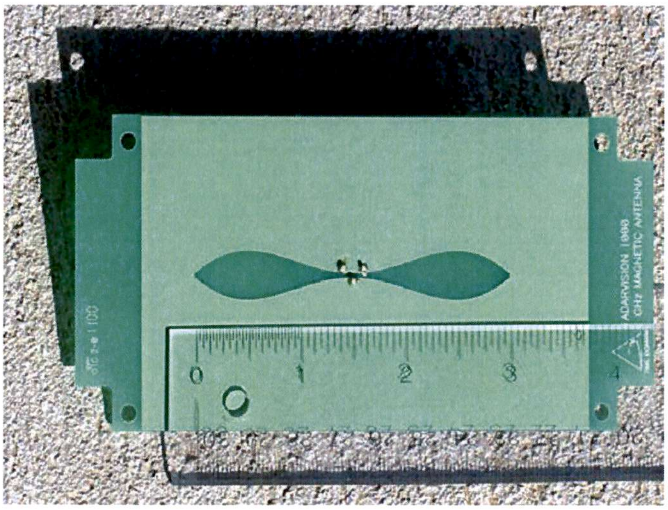

Figure 1.8: Barnes's UWB magnetic slot antenna. This antenna exhibited good performance in the Time Domain Corporation's RV1k through-wall UWB radar.

In this case, The monocones have been reduced to sectors to avoid the coupling between array elements and have been approximated by wires making them lighter and less vulnerable to wind. Moreover, they support the excitation of higher modes, so they are the best candidates for mode based DF systems.

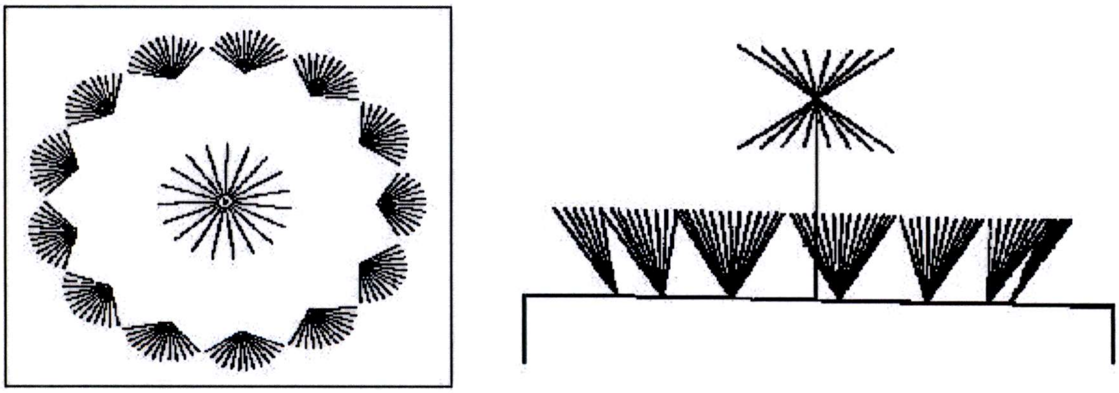

Figure 1.9: Circular array of monocone antennas.

Monopole small-electric antennas are very attractive for most of the UWB applications due to its simple geometry and ease of construction. Additionally, these antennas present an excellent performance as ultra-wideband antennas. Moreover, planar monopoles are a good alternative to reduce size, preserving acceptable performance, and can be implemented on a printed circuit board substrate making it inexpensive and readily manufacturable.

The most popular monopole antennas are disc, semi-disc, elliptical and inverted cone antenna (PICA). They are good UWB antennas, but there are two drawbacks related with the ground plane presence. First, DF systems are usually formed by circular arrays, and the ground plane geometry is difficultly compatible without increase dramatically the size. Second, the presence of the ground plane limits the the field of view of the system.

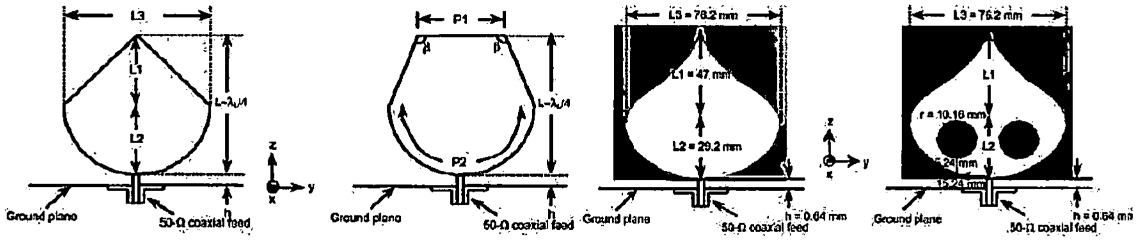

Figure 1.10: Geometries of PICA antenna (without holes) and two circular- hole PICA monopole antenna

Small-element dipole antennas present the most compact option to build circular arrays in DF systems due to its relatively small size and conformal shape. Furthermore, they are inexpensive. In general, these antenna present an omnidirectional pattern, which guarantee the DOA estimation over a large range of DOA.

There is a huge variety of shapes for UWB dipole antennas, but can be classified in planar conical and bulbous antennas:

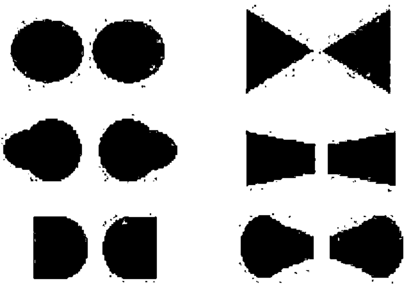

Figure 1.11: Different planar dipole shapes

Planar conical antennas include bow tie, diamond dipole and other angular antennas like bishops hat. Bow tie antennas are the most popular of this family of antennas and have been widely used in UWB applications, they were introduced by Lodge in 1890s. These antennas are basically the planar cross-section of a biconical antenna. Bow tie antennas have a constant gain over a 5:1 bandwidth, but they are difficult to match.

The diamond dipole antenna is an inverted bow tie antenna, it was introduced by Masters in 1947. This antenna has isosceles triangular elements whose height and base are scaled to be $\lambda/4$ at the center frequency of interest. The antenna has a quasi-Gaussian impedance bandwidth, so it radiates a uniformly shaped impulse response with the form of the third derivative of a Gaussian. However, this quasi Gaussian response is created by reflecting back significant energy. Moreover, the abrupt discontinuities are responsible of significant reflections and the antenna presents a poor matching (2,75:1).

Bulbous antennas include circles, semicircles, ellipses and ovoids. The elliptical dipole tends to have a more uniform gain response in band. Thus, for most applications elliptical dipoles, also called butterfly shaped dipoles, are preferred.

Planar elliptical dipoles allow matching with return loss in the order of −15 dB over a frequency band with a fractional bandwidth 10:1 or better. Despite their planar form factor, they also exhibit near omni-directional dipole-like patterns over a larger than 3 to 1 span in frequency. Planar elliptical dipoles elements are as small as 0.14λ at their lowest frequency of operation. These antennas also offer radiation efficiencies in excess of 90% in the band. In conclusion, elliptical dipoles are good candidates to form an antenna array.

1.4 Overview of the report

The report is organized as follow. The first chapter gives to the reader an introduction to the research area. To this end, the Radio Direction Finders (RDF) are introduced, explaining its multiple applications and difficulties. Special attention is paid in the description of the different systems employed, and the single antenna elements that form these systems.

The second chapter is about the numerical techniques employed to solve electromagnetic problems. In this section, the software employed in the resolution of the problem (CST) is introduced, explaining the adequacy of the technique for this problem, and checking the convergence and validity of the results.

The third chapter deals with single antenna element design. The elliptically shaped dipole antenna, also called butterfly antenna, is adopted as the elemental radiating unit and an extensive parameter study is carried out, proving that butterfly antennas feature robust circuital and radiation properties. In addition, a suitable antenna radome is adopted to enhance the front-to-back radiation ratio over the whole operational bandwidth, as well as to increase environmental durability of the structure.

The fourth chapter explains the algorithms employed for DOA estimation. Particularly, the MUSIC algorithm is widely described, including its many variations and its performance in different scenarios.

The algorithm-oriented array design is covered in the fifth chapter. A Uniform Circular Array (UCA) geometry is adopted, and suitable design guidelines of the array, aimed to the enhancement of the accuracy in DOA estimation are presented.

The sixth chapter includes a description of the most common sources of error of these systems: mutual coupling and errors in the antennas characteristics. Moreover, this chapter also includes an overview of the calibration techniques employed to alleviate these problems, and a novel calibration technique is presented.

Finally, the last chapter presents the conclusions and suggestions for future work.

Chapter 2

Numerical techniques for electromagnetics

2.1 Introduction

As any other area of science and engineering, antenna design requires the use of computational tools to deal with complex but necessary mathematical problems. The analytical methods of solving electromagnetic field problems are very useful for understanding the behavior of electromagnetic systems, but there are only special cases when they can be used in real engineering applications.

Therefore, the numerical methods that solve the Maxwell equations are numerous, and have attracted a great deal of attention in the scientific an engineering communities, as evidenced both by the great amount of published material and by the increasing number of conferences devoted to this subject.

Furthermore, computational electromagnetics has become a transversal discipline needed in a wide range of engineering areas, like modeling of electrical machines, microwave device modeling, semiconductor device design, the design of the modern particle accelerators and plasma fusion reactors, superconductor devices...

A first classification of the computational electromagnetics methods would be into:

- Differential methods (FEM, FD, TLM, FIM), based on the discretization of Maxwell's equations over the entire domain and compute the unknown variables over the entire domain. Note that the discretized Maxwell's equations can be in differential or integral form since they are basically equivalent.
- Integral methods (MOM), based on the discretization of certain specific integral equations involving the Green's function of the structure. As Green's functions are related to sources of the field the unknowns are, in most cases, discretized currents. And thus, the discretization takes place only on the metallic surfaces.

Moreover, these methods have different versions: static (if time variations are ignored), time domain, frequency domain, and eigensolver (the method only find the propagation modes of waveguides, cutoff frequencies, characteristic impedance and propagation constants).

Each method offers advantages and disadvantages depending on the class of problems. Therefore, the choice of the numerical tool is not trivial, and has a great impact in both, the resources consumed during the design process and the accuracy of the results. Furthermore, it is always desirable to check the results with more than one method, in order to prove the converge of the results to the actual solution.

The analysis of the antennas presented in this thesis has been carried out with Computer Simulation Technology MicroWave Studio (CST MWS 2008) [1] . The software is based on the Finite Integration Technique (FIT) with hexahedral-Perfect Boundary Approximation (PBA) mesh, that was first proposed by Weiland in 1977.

2.2 Selection of the numerical tool

As anticipated, there is a variety of methods employed in the solution of the Maxwell equations. Unfortunately, all methods have advantages and drawbacks for a given problem, so the numerical tool must be carefully chosen. In fact, an adequate selection of the software employed will save numerous resources in terms of time and memory, and more importantly, it will bring more accurate results.

Therefore, it is necessary a good description of the problem in order to chose the adequate numerical tool. The goal of this thesis is the design and full-wave analysis of conformal ultra-wideband antenna arrays. Hence, the characteristics of the problem can be summarize in the following points.

- 3D problem
- Wideband problem

- Excitation problem. Current, impedance, S_{11} parameters and radiated fields required
- External problem
- No strong resonant effects

Moreover, the description of complicated structures and contours is required, because conformal antennas are employed, and the chosen method has to be able to describe it accurately, and if its possible, without increment dramatically the computational burden.

FDTD and FIT are more efficient, in terms of memory and time, than integral methods in 3D, wideband, excitation problems without strong resonant effects. Furthermore, there are more reliable in the calculation of near-field parameters, such as the scattering parameters, surface currents and impedances, where the convergence of the results obtained with integral methods must be checked.

However, these methods have also drawbacks in this problem. First, a Near to Far Field Transform (NFFT) is needed for the computation of the radiation patterns, increasing the cost of the simulations. Second, the spatial domain must be finite, so a absorbing materials are needed to recreate external problems.

In this thesis, the electromagnetic tool employed is the commercial software Computer Simulation Technology MicroWave Studio (CST MWS 2009). It is Finite Integration Technique (FIT), whose characteristics for the resolution of the structures studied in the thesis have been discussed. The mesh generation of CST is based in the Perfect Boundary Approximation (PBA) technique, that it is able to describe complex structures without increase dramatically the computational burden.

For a better understanding of the reader, the FIT technique and other of the most popular numerical tools for electromagnetics are described in the appendix.

2.3 Simulation performance

Even the commercial softwares produce inaccurate results if they are not handle with care. Therefore, the convergence of the results must be checked. To this end, this subsection describes how the simulations with CST are monitorized, and the convergence of the results for a planar elliptically shaped dipole antenna. Moreover, even if the results converge, they could not converge to the actual solution, so it is necessary to compare the results with the physical intuition. Hence, all the results obtained in this thesis are analyzed from a physical point of view.

However, the simulations presents a trade-off between accuracy and computational load. Obviously, obtaining the accuracy of the results is the first priority, but there is no point in running unnecessary heavy simulations.

The accuracy of the simulation is mainly determined by both the mesh type and the mesh density. The hexahedral mesh with PBA has been chosen as the mesh type, which is known to give an accurate modeling of curved boundaries, with a relative low computational cost. Concerning to the mesh density, it is expected that the more dense the more accurate. However, increasing the mesh has a direct impact on the computational load. So the accuracy is restricted by practical issues like simulation time and memory available.

This compromise is specially important for the class of antennas analyzed in this thesis. The spatial domain is discretized in FIT. Hence, the grid must be dense enough to cover the smallest detail of the structure, and at the same time it is extended through the maximum dimension of the antenna. It yields to heavy computational burden for large structures with small details. Unfortunately, the antenna is relatively large because it is covering low frequencies, but the feeding needs quite small detail, so the aspect ratio of the structure is high, and the mesh complicated.

In CST, there are three ways to define the mesh: manually, automatically and adaptively. Manual generation is a not recommended and old-fashioned way. The adaptive mesh refinement runs the simulation repeatedly until the deviation between two successive simulations falls below a given accuracy level. This technique guarantees a high accuracy at the expense of simulation time. Furthermore, it is possible to run out of memory with complex structures.

The automatic mesh generation is probably the most effective way. The mesh generator determines the important features of your structure and automatically creates a mesh. This process is governed by a few settings:

- Lines per wavelength: defines the minimum number of lines per coordinate direction based on the highest frequency of evaluation.
- Lower mesh limit: defines a minimum distance between two mesh lines for the mesh by dividing the diagonal of the smallest bounding box face by this limit.
- Ratio limit: Defines ratio between the biggest and smallest distance between mesh lines. Increase for mesh quality when high aspect ratios exist.

The S_{11} parameter is a good measure of the quality of the mesh, because it is more sensitivity to lack of accuracy than other desired outputs like radiation patterns. Thus, the figure 2.1 shows the effect of the parameter "lines per wavelength" in the S_{11} parameter of the antenna. This parameter governs the mesh density so it has a great impact in the S_{11} parameter of the antenna. Excellent convergence is obtained for 40 lines and 50 lines. Nevertheless, it is clear that the differences are not so evident at low frequencies, and a good convergence can be obtained with 30lines up to 1.2GHz.

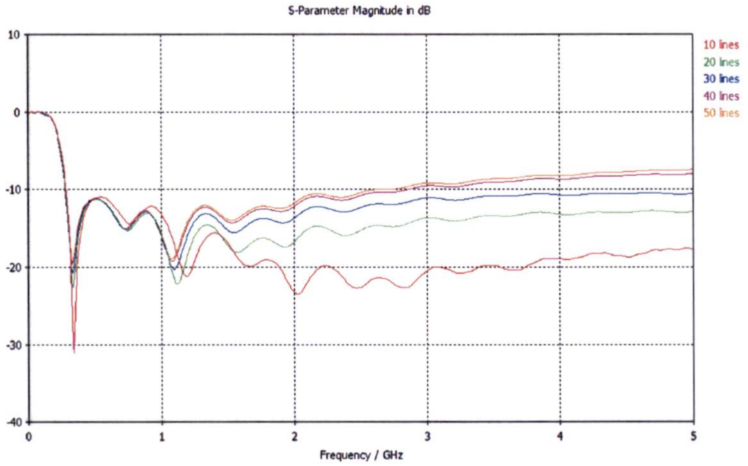

Figure 2.1: Antenna return losses with several mesh densities

However, increasing the number of lines per wavelength also increases exponentially both, the time and the memory required for the simulation, figure 2.2. The time required for the solver step is larger by far than the time required for the matrix calculation.

Additionally, it is also possible to set another parameter called "accuracy" in the transient solver. This parameter is useful when simulating short time domain pulses, and determines the lower bound of the remaining energy in the system before finish the simulation. Obviously, this parameter has great influence in the time per simulation. The effect of the "accuracy" parameter in the S_{11} parameter is shown in the figure 2.3. Contrary to the lines per wavelength, a bad choice of this parameter causes errors at low frequencies. Other typical consequences are values of the S_{11} parameter over 0dB near DC, what is physically impossible, and ringing in the values at high frequencies. The similar artifact is introduced if the PML material if the selection is not adequate.

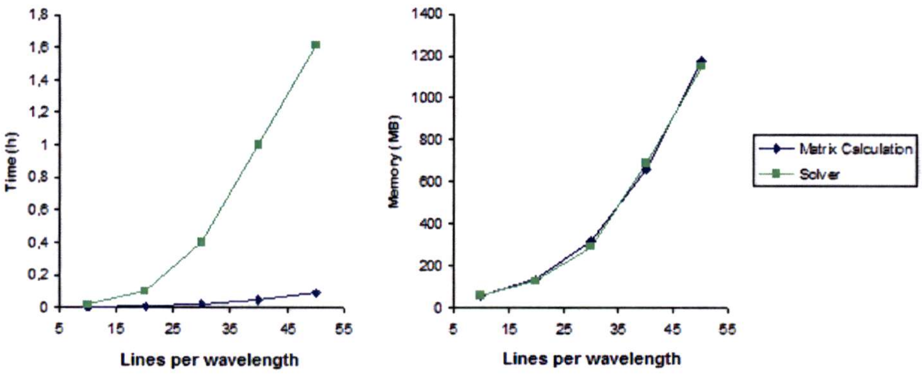

Figure 2.2: Computational burden, time and memory, vs number of lines per wavelength

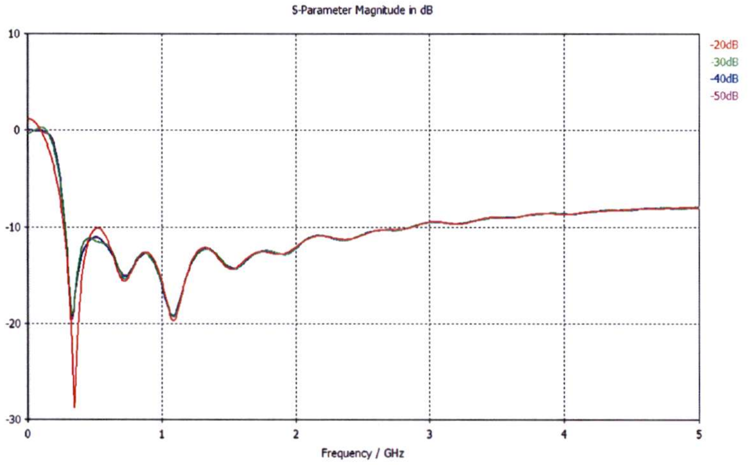

Figure 2.3: Antenna return losses vs frequency for several accuracy levels

The figure 2.4 shows the time and memory employed in the previous simulations. As expected, changing the accuracy level increases linearly the time employed in the solver step. The memory and the time spend in the matrix calculation remain unchanged.

The previous results give a good description of how the simulation of structures with CST is monitorized. However, in the practice the simulations can be optimized in order to save time and memory. For example, although simulate the antenna from DC to 5GHz is a good approach to analyze physical operation of the antenna and find the CST limitations, it is not a good strategy to design an antenna which is going to work from 250MHz to 1GHz. Thus, the bandwidth of the simulation is limited.

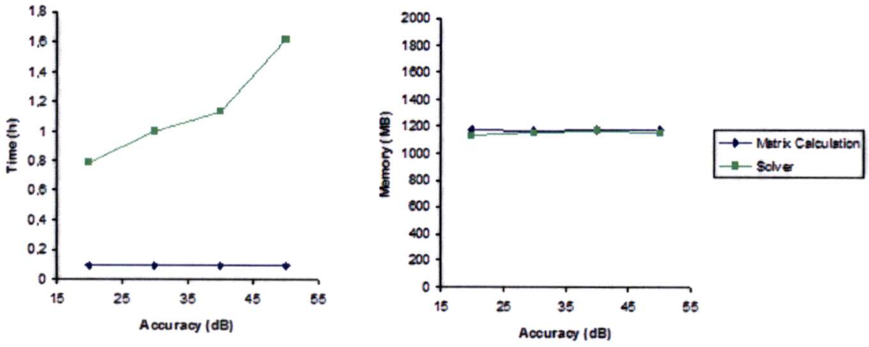

Figure 2.4: Computational burden, time and memory, vs accuracy level

Additionally, it is also possible to reduce the consumed resources taking into account the symmetry of the structure and placing planes to reduce the spatial domain. Particularly, if the antenna is placed in the YZ planes in this case, a perfect electric and magnetic planes can be placed in the XY and XZ planes, respectively. This configuration is shown in the figure 2.5, where the CST model of the structure is presented.

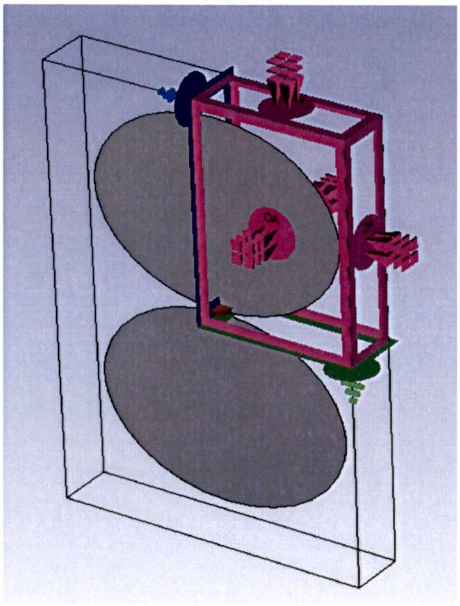

Figure 2.5: CST model with symmetry planes.

Chapter 3

Analysis of the elliptical dipole antenna

3.1 Introduction

Antennas for Direction Finding systems must meet some performance specifications. As direction finding applications involve the use of complex systems, like circular or cylindrical arrays, small and conformal antennas are needed to satisfy the size and weight and shape restrictions of mobile units. Moreover, incoming signal frequencies are, in general, unknown, hence it is interesting to cover as much bandwidth as possible, and it is desirable an ultra-wideband antenna behavior that avoids the use of excessive subarrays. Therefore, the ideal antenna must present a large impedance bandwidth and a stable radiation pattern along the bandwidth.

Furthermore, a directive radiation pattern can improve the accuracy in the angle-of-arrival (AOA) detection, reduce the probability of ambiguity and avoid coupling between the array elements and the supporting structure. However, an excessive directive antenna limits the range of detectable AOA, and blind angles could appear.

DF applications generally track narrowband signals, so although a large bandwidth is required, only a small fraction is used at one time. Therefore, it is not compulsory design a linear phase antenna or impose time domain restrictions. However, a short time domain antenna response is a desirable characteristic that can be very helpful in tracking wideband signals, so this characteristic should not be damaged gratuitously. Incoming signals can be diversely polarized so it is desirable an antenna that supporting both horizontal and vertical polarization.

As anticipated, planar elliptical dipoles are good candidates for DF systems. In this chapter, these antennas are analyzed, and a optimization for DF systems is presented. These antennas are known to perform well as UWB antenna. They allow matching with return loss level in the order of –10 dB over a frequency band with a fractional bandwidth 10:1 or better. Despite their planar geometry, they also exhibit near omni-directional dipole-like patterns over a larger than 3 to 1 span in frequency. Planar elliptical dipoles elements are as small as 0.14λ at their lowest frequency of operation. As it is a small antenna, a time domain antenna response with low dispersion is supposed, in fact, -40dB ringing after twice the duration of the pulse can be obtained.

Antenna gain is around 0-3dBi in the azimuth plane, and depends on antenna flair axial ratio. Due to the large flare angle in the vicinity of the feeding point, the antenna has low input impedance and can be well matched to a 100Ω feeding line. These antennas also offer radiation efficiencies in excess of 90% in the band. Planar elliptical dipoles can be implemented on printed circuit board substrates making them inexpensive and readily manufacturable.

One drawback of the elliptical dipole antenna, also called butterfly antenna, is that it is center fed, that is to say, a transmission line must couple to the gap between the elements. Necessarily this transmission line lies in the heart of the reactive fields surrounding the feed and is thus particularly vulnerable to undesired sheath coupling. This coupling is liable to distort the antenna pattern directly due to blockage and indirectly due to undesired cable currents.

In conclusion, elliptical dipole antennas present an excellent performance for UWB applications. In fact, they are largely employed in Ground Penetrating Radar (GPR) and Impulse Radio (IR) applications, and have been widely studied in that context. However, although there are several modifications that improve the performance of the elliptically shaped dipole in that applications, it is mandatory to consider if that improvements are really suitable for DF systems.

Planar elliptical dipole antennas are usually shielded [13]. In GPR applications radiation in the upper half-space (air) must be minimized and the influence of external signals from the upper half-space to the receive antenna must be reduced (e.g. TV, mobile phones, targets above ground). In IR applications it is necessary prevent radiation into the device or human body and avoid influence of the device or human body on antenna performance. Antenna shielding can also reduce the coupling effect between array elements in DF systems. However, the shield can decrease the antenna bandwidth or reduce the antenna gain, specially if absorbers are employed. Moreover, the size and weight of the system is increased.

One useful technique to enlarge the antenna bandwidth and reduce the late-time ringing is the application of the resistor loading. The well-known Wu-King profile can be use to determine the loading distribution along the antenna. However, resistor loading reduces drastically the radiation efficiency. More complex profiles, like resistor-capacitive (RC) loading with linear or non-linear profiles, are employed to deal with this drawback [16],[17].

3.2 Physical description of the elliptical dipole antenna

In the next sections, the planar elliptical dipole antenna is going to be analyzed and optimized. The influence of parameters like size, eccentricity and separation between antenna flairs is going to be studied, and finally, an optimization of the antenna will be presented.

However, in order to understand what is going on when "playing" with the antenna parameters, it is necessary understand how the antenna works and how the radiation mechanism takes place. To this end, this section gathers together some clarifying results.

The radiated field can be inferred from the current distribution. Therefore, one first step in understand how the radiation process takes place is analyze the current distribution over the antenna surface. Paying attention to the surface current distribution it is clear that the current is concentrated near the feed point, and is extended along the antenna edges. Due to the Hertz principle, the maximum current values are concentrated near the antenna edges, this effect becomes stronger as the frequency is increased.

This is the typical behavior of a travelling wave antenna. The signal is introduced at the feed point, and the field propagates along the antenna structure decreasing its magnitude, losing energy due to the radiation phenomena (and due to the conductor losses in a not so ideal case). If the field is enough weak at the end of the structure, the reflections are avoided.

It is well known that reflections must be avoided in order to obtain a large bandwidth. Otherwise, resonance effects appear. Since this antenna is working in that way, it presents a good impedance bandwidth.

However, if attention is paid at the antenna return losses, presented in figure 3.1. It is possible to notice that the travelling wave mode of operation is not perfect. In fact, the presence of resonances at 330MHz and 1.07GHz is evident. Actually, the wideband behavior of the elliptical dipole is based on a combination of resonant and travelling wave modes.

The resonant modes are dominant at low frequencies, as the frequency is increased the travelling wave modes take more importance. The reason is that at higher frequencies, the current oscillates more times before reach the the possible reflection points, since some energy is lost due to the radiation phenomena in each cycle, the field is weaker and the resonant effects are less important. Therefore, as the frequency increases the resonant effect are less important and the return losses spectra becomes flatter. Finally, at higher frequencies the capacity of the antenna to support travelling wave modes is degraded, and the antenna return losses are progressively increased.

The figure 3.2 shows the surface currents over the antenna and 3D radiation pattern, at frequencies 330MHz, 1.07GHz and 2GHz. The surface current and radiation pattern at 330MHz shows that the antenna is working closely to the classical dipole mode. The current is maximum at the feeding point, and its magnitude is decreased up to the top of the antenna, where it is nearly zero, due to the reflection in the antenna top. Although the current is maximal in the antenna edges, at this frequency the current is well-distributed and expanded along the antenna surface.

Consequently, the radiation pattern is also close to the dipole one. It is mainly donut shaped, but it is slightly not omnidirectional, and the radiation is concentrated in the front and back directions. The dipole-like behavior is hold at the lower frequencies of the band.

As the frequency is increased, the current is more concentrated near the antenna edges. Therefore, the reflection in top of the antenna is weakened, and the influence of this mode is reduced. The next dominat mode is governed by the currents circulating around the antenna envelop. The surface currents and the radiation pattern shown at 1.07 GHz describe this mode of operation. Since the radiation points are situated

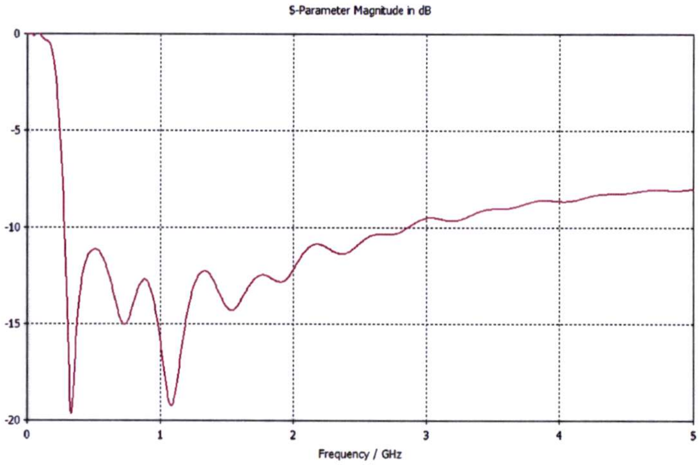

Figure 3.1: Antenna return losses vs frequency. Elliptically shaped dipole of minor ratio 95mm, eccentricity 1.4 and gap between the antenna flairs 2mm.

in the envelop, the main radiating directions are pointed towards the envelop humps, that is to say, $\theta = 45,\ 135\ ,225\, and\, 315^{o}$.

Finally, at the higher frequencies of the band the current is oscillating faster. Since some energy is lost in each period due to the radiation the fields are weaken sooner and the antenna is mostly working as a travelling wave antenna. At this frequencies the radiation fields are mainly directed in the $\phi = \pm 90^{o}$. Unfortunately, this pure travelling wavemode of operation is not well-suited for the integration of the antenna in Uniform Circular Arrays. Although reasonable values of gain are achieved, the maximum directions of radiation are pointed toward the other antennas of the array, and the mutual coupling will be too high.

From other point of view, Schantz introduced in 2002[8] other way to think of a planar elliptical dipole as a pair of opposing slotline horns. In fact, he showed that the results produced by employing a elliptical dipole of eccentricity 1.5, an exponential taper and a Klopfenstein taper are virtually identical.

Other characteristic of the elliptical dipole is a quite pure vertical polarization. However, from picture 3.2 it is clear that there is current in the y and z directions (where the antenna is contained YZ plane). Therefore, there should be field in that direction, so the sum of all current contributions have to annul the y-component of the radiated field.

An approximated model can be built inspecting the figure 3.2 it is possible to inferred the following symmetry . For each current element of the first quadrant (yz plane), there are other three elements in the other three quadrants that have the same current magnitude but different direction. If a differential current element is placed at the $[\Delta y, \Delta z]$ point, and follows the direction $[I_y \cdot \hat{y}, I_z \cdot \hat{z}]$. Then, the other current elements are placed at the $[-\Delta y, \Delta z]$, $[\Delta y, -\Delta z]$ and $[-\Delta y, -\Delta z]$ points, and follow the $[-I_y \cdot \hat{y}, I_z \cdot \hat{z}]$, $[I_y \cdot \hat{y}, -I_z \cdot \hat{z}]$ and $[I_y \cdot \hat{y}, I_z \cdot \hat{z}]$directions.

In general, the radiated field will be:

$\vec{E} = \int_V \vec{E}(\vec{r'}) \cdot d\vec{r'}$ Where $\vec{E}(\vec{r'})$ is the field produced by the current placed at $\vec{r'} = [\Delta y, \Delta z]$.

$\vec{E}(\vec{r'}) = E_y(\vec{r'}) \cdot \vec{y} + E_z(\vec{r'}) \cdot \vec{z}$

But under this approximation, it is only necessary to ingrate the field in the first quadrant. For each point of the first quadrant, the complete contribution to the electric field will be:

$$E_y(\vec{r'}) = E_{oy}(\vec{r'}) \cdot (-1)^{|z| mod R} \cdot 4 \cdot sin[\Delta z \cdot cos(\theta)] \cdot sin[k\Delta y \cdot sin(\phi) \cdot sin(\theta)]$$

$$E_z(\vec{r'}) = E_{oz}(\vec{r'}) \cdot 4 \cdot cos[\Delta z \cdot cos(\theta)] \cdot cos[k\Delta y \cdot sin(\phi) \cdot sin(\theta)]$$

Where R is the vertical radius of the antenna.

Using this model, the electromagnetic field polarization in the E and H planes, that is to say, in the $\theta = 90^{\circ}$ and $\phi = 0^{\circ}$ planes, can be predicted. In both planes the $E_y(\vec{r'}) = 0$ and $E_z(\vec{r'})$ is in general no null. Therefore, the polarization is purely vertical in both planes.

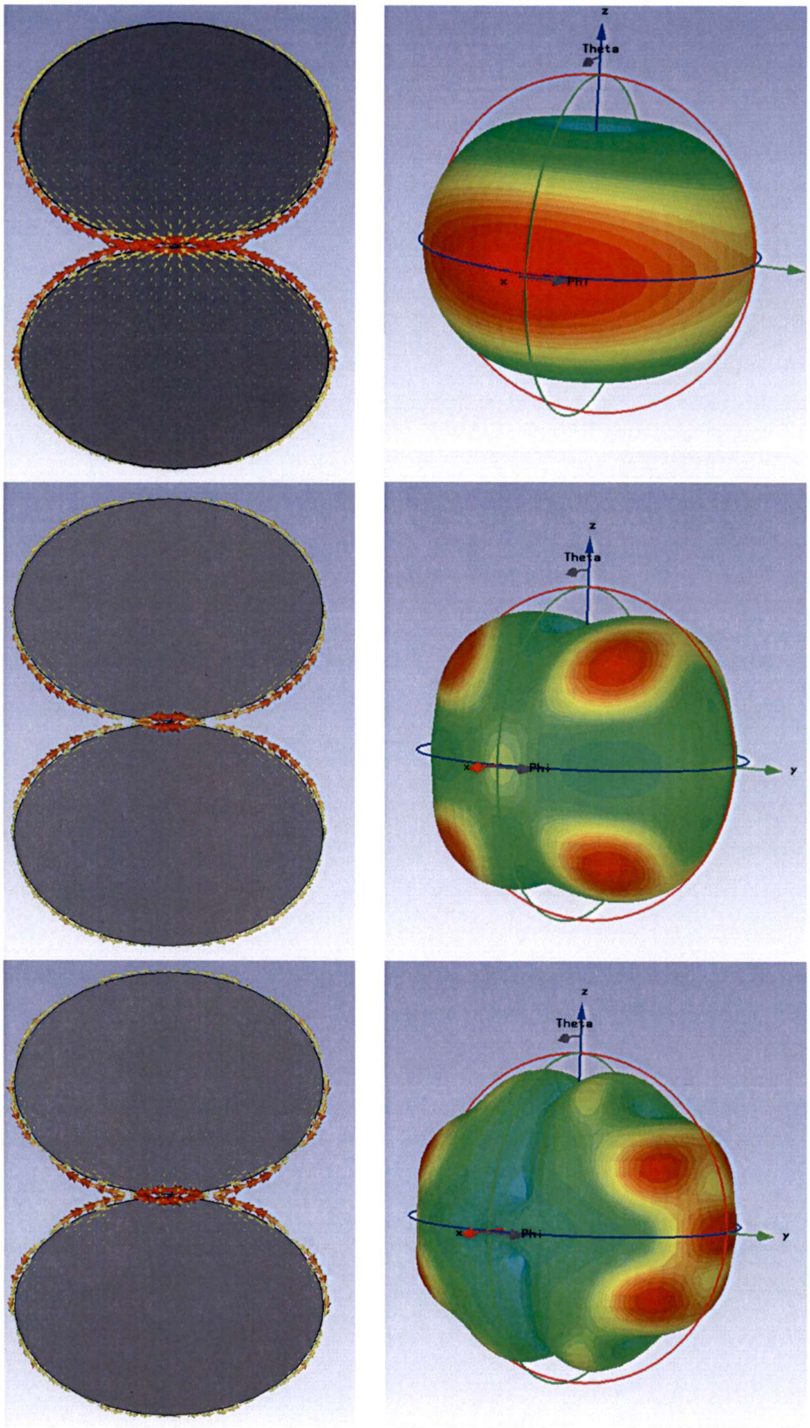

Figure 3.2: Surface currents over the antenna and 3D radiation pattern. Frequencies 330MHz, 1.07GHz and 2GHz

3.3 Analysis of the elliptical dipole antenna

In this section the analysis of the planar elliptical dipole is presented. An extensive parameter study has been carried out to evaluate its impact in the antenna performance. The parameters under test have been antenna size, shape (or eccentricity) and gap between the antenna flairs.

3.3.1 Effect of the antenna size in the antenna performance

The figure 3.3 shows the antenna return losses versus frequency for different antenna radiuses. The antenna minor ratio has been swept from 70 to 100mm in order to study the effect of the antenna size in the antenna performance. That means that the antenna has been scaled without altering the antenna shape.

As expected, increasing the minor ratio of the antenna leads to a shift of the antenna response toward lower frequencies. This behavior is a direct consequence of changing the electric size of the antenna.

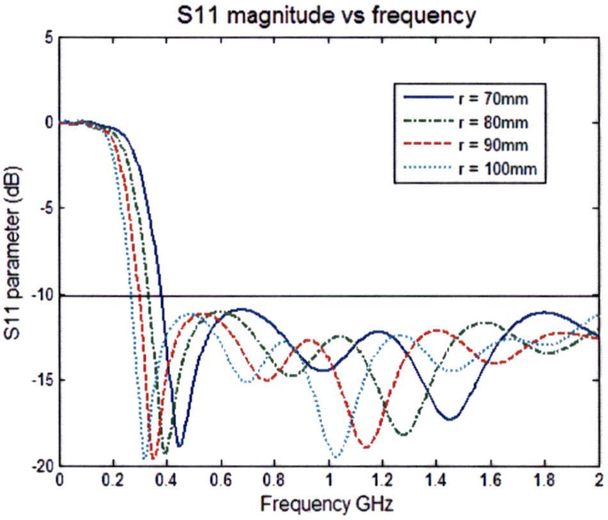

Figure 3.3: S_{11} versus frequency. Antenna sizes from 70 to 100mm

3.3.2 Effect of the antenna shape in the antenna performance

The effect of the antenna shape in the antenna performance has been checked running simulations varying the antenna eccentricity with a fixed minor radio fixed to 9.5cm and gap between the antenna flairs of 2mm.

In the figure 3.4 it is shown that increasing eccentricity the first resonant effect is reduced. As can be inferred from the physical description of the antenna, the current is concentrated at the antenna edges, so a larger eccentricity separates the current form the top of the antenna and the first resonant mode, governed by the antenna diameter, is weakened. Moreover, the other resonant mode are shifted toward lower frequencies and the strength of the resonance near 1GHz is increased, the reason is that this modes are governed by the antenna envelope, and it is increased by a larger eccentricity.

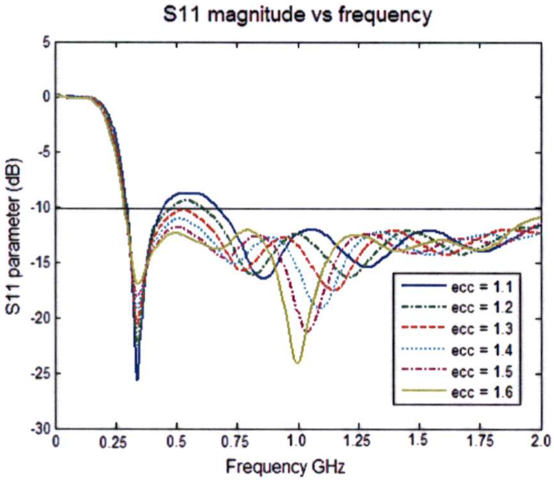

Figure 3.4: S_{11}versus frequency. Eccentricity values from 1.1 to 1.6.

However, the eccentricity also has influence in the radiation pattern. Increasing the eccentricity the antenna radiation pattern becomes more unstable, so the bandwidth where the radiation pattern is nearly to the dipole one is smaller, an the antenna performance worse. In the figure 3.5 the H-plane for different eccentricities is presented. It is shown that the radiation towards the $\phi = \pm 90^{\circ}$ appears sooner for higher eccentricities. And the coupling between the array elements. Therefore, the choice of the optimum eccentricity presents a trade-off between impedance bandwidth and radiation pattern stability that must be solved.

However, as it is shown in the figure 3.6 the bandwidth in terms of gain is almost unaltered while changing the eccentricity. Hence, increasing the eccentricity yields in a poorer radiation pattern, but has not effect in the gain in the front direction. ($\phi = 0^{\circ}$, $\theta = 90^{\circ}$).

From other point of view, according to Schantz [10] the optimal eccentricity value must fit two basic principles: it must be conformal to the energy-flow streamlines of the desired field configuration, and the stored reactive energy must be minimized. In this case, the desired configuration is the ideal Hertzian dipole, and the optimum eccentricity value presents conformity to the streamlines. Furthermore, increasing eccentricity a fatter shape is obtained, so undesired concentrations of reactive energy are avoided.

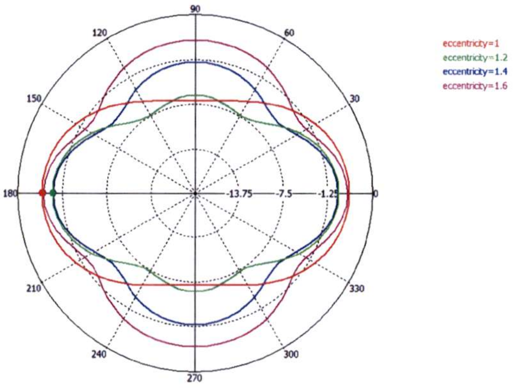

Figure 3.5: H-plane of the radiation pattern for eccentricities 1, 1.2, 1.4 and 1.6.

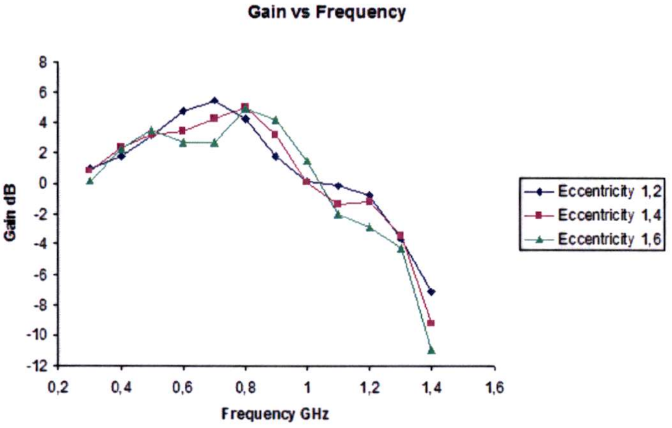

Figure 3.6: Gain versus frequency, eccentricities 1.2, 1.4 and 1.6

3.3.3 Effect of the separation between the antenna flairs

The effect of the separation between the antenna flair has also been studied. Separation gaps between 2 and 5mm have been simulated. The results are shown in figure 3.7. The antenna performance improves by decreasing the gap. In fact, the shorter the spacing the lower the reflection coefficient. The differences are more noticeable at higher frequencies.

The real and imaginary part of the antenna resistance is shown in figure 3.8. As it is shown, the gap between the antenna flairs has a great influence in the antenna impedance, so it has an important effect in the return losses. As the gap increases, the real part of the impedance is also increased, and an inductive load is added, due to the presence of the feeding wire.

Nevertheless, the gap between the antenna flairs must be chosen taking into account mechanical constraints and considerations concerning the antenna feeding.

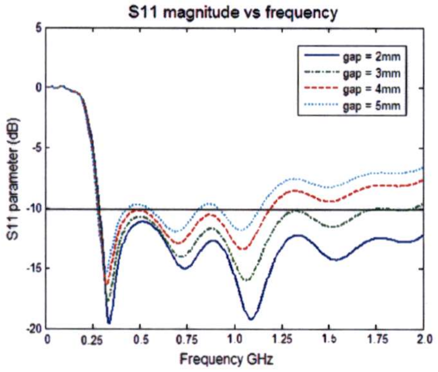

Figure 3.7: S_{11}versus frequency. Gap between the antenna flairs from 2 to 5mm.

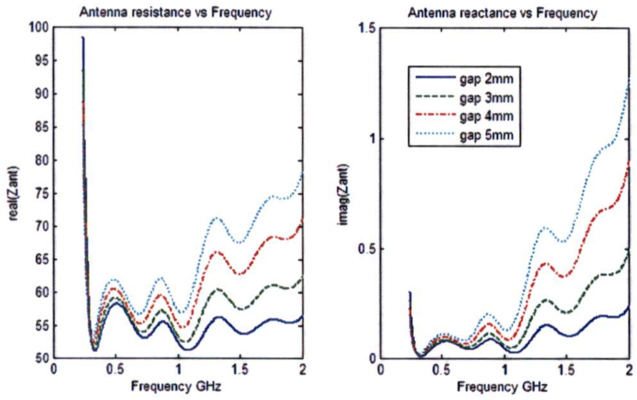

Figure 3.8: Antenna resistance and reactance. Gap between the antenna flairs from 2 to 5mm.

3.4 Impact of the curvature radius

The main features of the elliptically shaped dipole antenna have been analyzed in the previous section. However, this antenna is going to be employed in conformal circular arrays, and the plane case is a mere approximation. The main advantage of the use of conformal antennas is that they lead to a smaller, more compact system, or even in a system that could be integrated in other structures. In spite of this, the antennas are subjected to a deformation, so the impact of this deformation in the antenna performance must be studied.

Since system is basically a circular array, the deformation consists in bending the antenna over a cylinder. As it is shown in the figure 3.9, there is two possible deformations, for the vertical and horizontal polarization array.

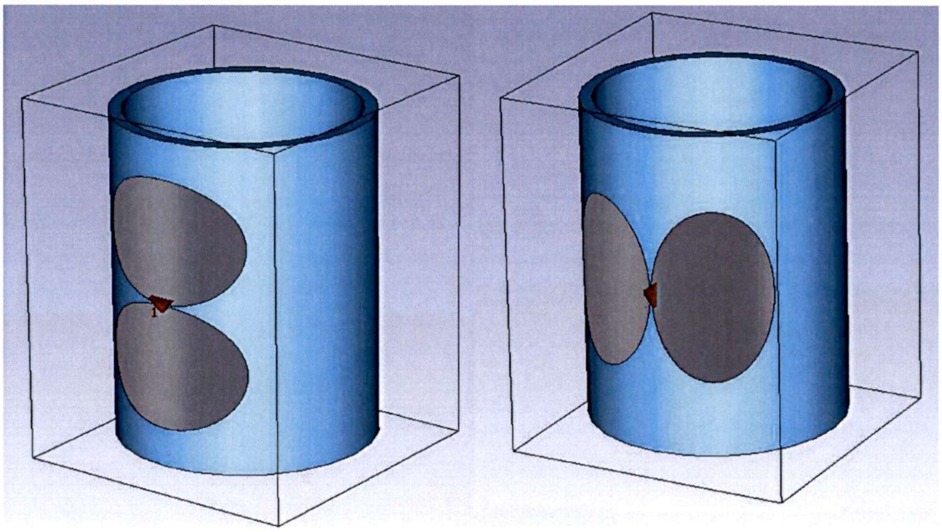

Figure 3.9: Antenna bent over a cylinder. Two possible directions directions corresponding with vertical and horizontal polarization arrays.

The antenna employed in the simulations is an elliptical dipole with minor radius 95mm, eccentricity 1.4 and gap between the antenna flairs of 2mm. The curvature radiuses studied come from 15 to 45cm.

The figure 3.10 shows the impact of the curvature radius in the antenna return losses for the two possibilities. In order to fully understand the impact of the deformation in the antenna performance, it is necessary to describe how the antenna is radiating. As anticipated in the physical description of the antenna, the wideband behavior of the antenna is based on the superposition of different modes.

At the lowest frequencies the dominant mode is the resonant mode due to the reflection on the top of the antenna flair, and the antenna is nearly acting as a dipole. At intermediate frequencies the dominant modes are governed by the envelope of the antenna flairs, and the antenna is mainly radiating in the direction of the envelope humps. At the highest frequencies, the dominant modes are the travelling ones, and the antenna can be analyzed as two opposite slotline horns. As it is shown in the picture 3.10 curving the antenna in the horizontal direction has no effect at the lowest frequencies, where the dominant mode is the resonant vertical one. However, there is degradation in the antenna return losses at higher frequencies, due to the curvature along the antenna edges.

Inversely, when the antenna is bent in the vertical direction, there is degradation in the first resonant mode, but the performance is almost the same at higher frequencies. In any case, the antenna is quite robust against this deformation, and the return loss level is hold even with very small radiuses, under the practical limit for its use in circular arrays.

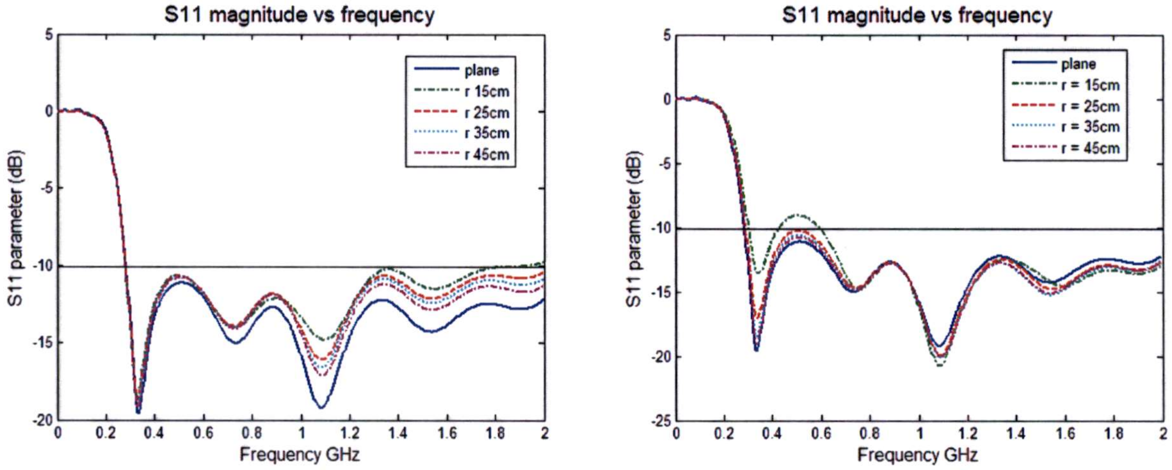

Figure 3.10: S_{11}parameter vs frequency for a curvature radius from 15 to 45cm.

The deformation also has impact in the antenna radiation pattern. The figures 3.11 and 3.12 shows the E and H plane at 600MHz for the two different conformal antennas. It is shown that reducing the curvature radius leads to a wider beamwidth in the front direction and a thinner beamwidth in the back direction. Furthermore, the front to back ratio is degraded, fig 3.13. Both effects are in correspondence with the physical intuition, taking into account how the antenna is bent, and the analogy with the reflector antennas.

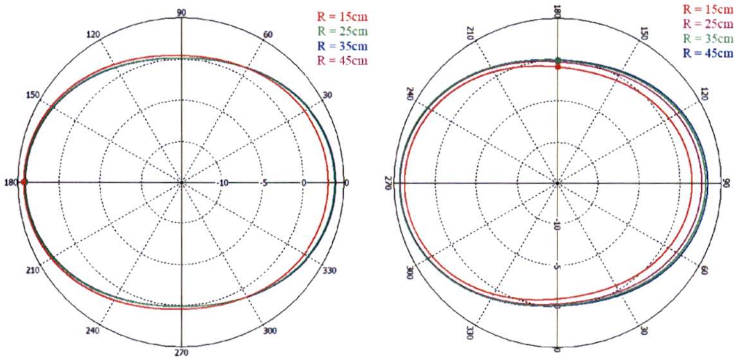

Figure 3.11: Antenna gain in the H-plane at 600MHz. Curvature radius from 15 to 45 cm.

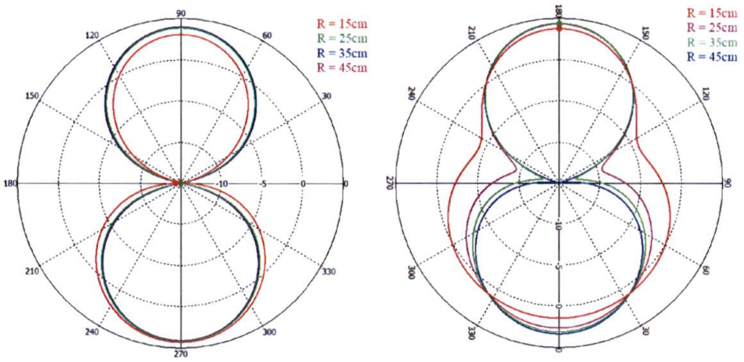

Figure 3.12: Antenna gain in the E-plane at 600MHz. Curvature radius from 15 to 45 cm.

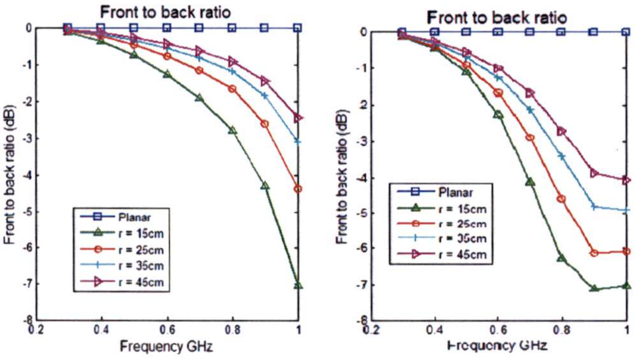

Figure 3.13: Gain and front to back ratio vs frequency. Planar antenna and curvature radius from 15 to 45 cm.

3.5 Antenna cover

3.5.1 Introduction

Antenna elements previously presented are going to be employed in outdoor, and perhaps mobile applications, what means that the system will be exposed to severe weather conditions. A cover is necessary to protect the antenna form environmental hazards, such as rain, fog, snow and small stones that can impact in the antenna. Moreover, these systems are usually mobile units, so the array structure is exposed to some mechanical forces producing during the conduction, and the cover can also improve the mechanical stability of the antennas.

Both disturbances, environmental hazards and mechanical actions, can compromise seriously the performance of the system. Environmental hazards can affect the antenna performance dramatically and the effect of a violent conduction of the mobile units can change the array geometry. Therefore, these disturbances are an actual engineering problem and it would be fallacious to ignore them.

The cover structure also affects the electromagnetic behavior of the system. It has been studied that introducing different materials in the neighborhood of the antenna affect adversely the antenna performance. However, it has also been demonstrated that with specific configurations, the antenna performance can be improved in some aspects. Hence, a study of the cover structure in electromagnetic terms is included.

3.5.2 Superstrate material

The superstrate material must be chosen carefully. Since it is going to protect the system from severe weather conditions, there are some characteristics which must be considered in the selection: moisture absorption, thermal conductivity, coefficient of thermal expansion and peel strength.

Furthermore, other characteristics are necessary to do not compromise the antenna performance. The dielectric constant must present a small tolerance over the entire operational bandwidth and a low dissipation factor is required to do not diminish the gain.

Moreover, the direction finding system is a circular array, so the material must be deformable during the fabrication process, but it must have enough mechanical strength to support the antenna. Since the system operates at low frequencies, it has a considerable size, and material cost must be taken into account.

Nowadays, there are many dielectric materials commercially available. The most popular are based in Glass Reinforce PTFE, Ceramic filled PTFE and Hydrocarbon-based Microwave materials. Therefore, it is possible to choose between different options. In this thesis the material Orcer RF-35 offered by taconics is proposed, because this material covers the previously exposed requirements at a moderate cost.

3.5.3 Superstrate structure

It is well documented that the proper choice of the cover parameters can enhance some antenna basic performance characteristics, such as gain, radiation resistance and efficiency. [12, 14, 13]. However, most of these attempts are based in satisfy some resonance conditions, so they could not be suitable for UWB operation.

Nevertheless, it is possible to try with other approaches. For instance, it is well known that the electromagnetic field tends to be concentrated in the zones with high dielectric constants. Therefore, it can be expected that placing a supertrate with a relatively high permittivity may concentrate the gain in the front direction, improving the front to back ratio, and thus, reducing the coupling between the array elements, specially the coupling between the antennas and the supporting mast.

Since strong resonance effects must be avoid, the dielectric thickness must be small in comparison with the minimum wavelength of operation. Most studied structures are based in satisfying some resonant conditions choosing the thickness of the superstrate and substrate layers equal to $\lambda/4$ and $\lambda/2$. However, these narrowband concepts can not be applied in this situation, and the superstrate thickness will be restricted

The antenna employed in this section to analyze the impact of the superstrate structure in the antenna performance is an elliptically shaped dipole with minor radius equal to 95mm, eccentricity 1.4 and gap between the antenna flairs 2mm.

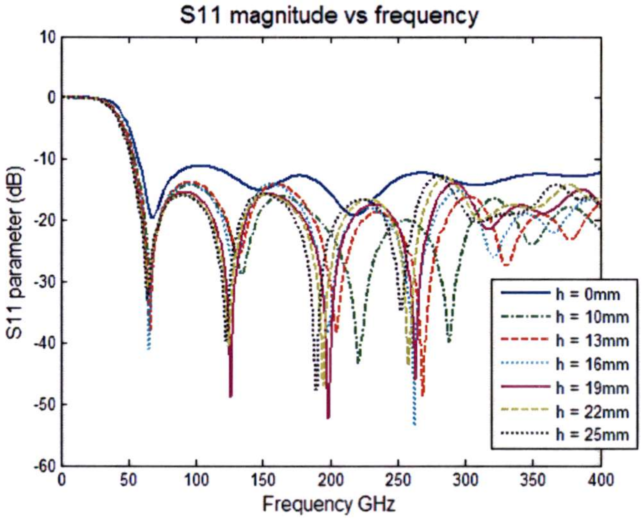

Figure 3.14: S_{11} parameter versus frequency for different superstrate thicknesses.

In the figure 3.14 the S_{11} parameter for different thicknesses is represented. The material is a dielectric with permittivity equal to 3.5. It is shown that the return loss level is improved in comparison with the antenna without the superstrate structure. Furthermore, the presence of the superstrate also produces resonant effects, but these resonant effects do not diminish the impedance bandwidth.

It is also shown that the first resonant frequency and the cross through the return loss $-10dB$ level are shifted toward lower frequencies. These effects are a consequence of the diminution of the wavelength in the dielectric material.

The figure 3.15 shows the gain and front to back ratio vs frequency for superstrate thicknesses from 10mm to 25mm. As expected, these pictures show that it is possible to improve the front to back ratio of the antenna increasing the superstrate thickness. However, the inclusion of the superstrate also reduces the bandwidth in terms of gain.

Although the RF-35 superstrate material has been suggested, it is also possible to study the use of other materials, whether if they are available or not. The figure 3.16 shows the S_{11} parameter versus frequency for different superstrate permittivities, and the figure 3.17 shows the gain in the front direction and front to back ratio versus frequencies for different superstrate permittivities. It is shown that change the superstrate permittivity has the same effect than change the superstrate thicknesses. However, the impedance matching is worse for higher permittivities.

In conclusion, the inclusion of the superstrate structure improves the antenna return losses and the front to back ratio. However, it yields in a more unstable radiation pattern and reduces the bandwidth in terms of gain. Therefore, the choice of the optimum superstrate presents a compromise between bandwidth and coupling effects. Although the coupling effects are usually alleviated with calibration techniques the influence of the mast could degrade the antenna performance.

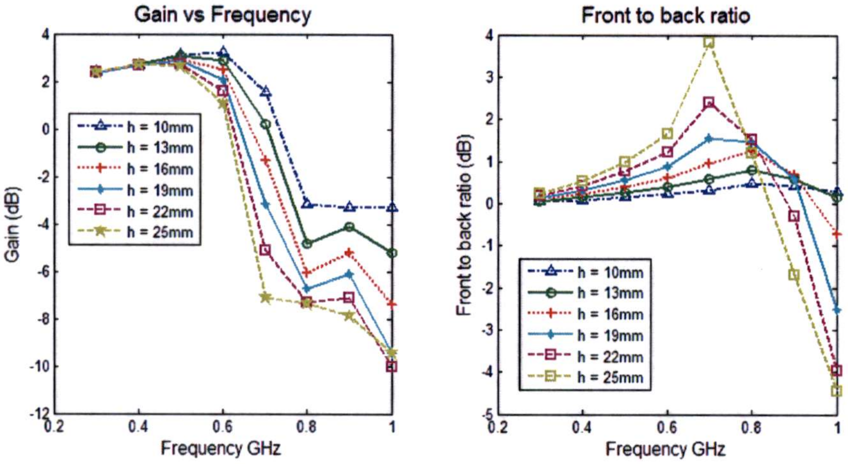

Figure 3.15: Gain and front to back ratio vs frequency for superstrate thicknesses from 10mm to 25mm.

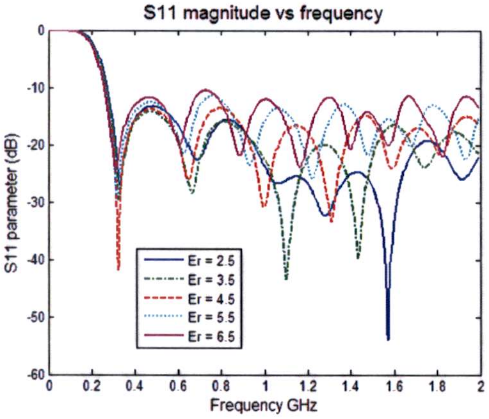

Figure 3.16: S_{11} parameter versus frequency for superstrate permittivities from 2.5 to 6.5.

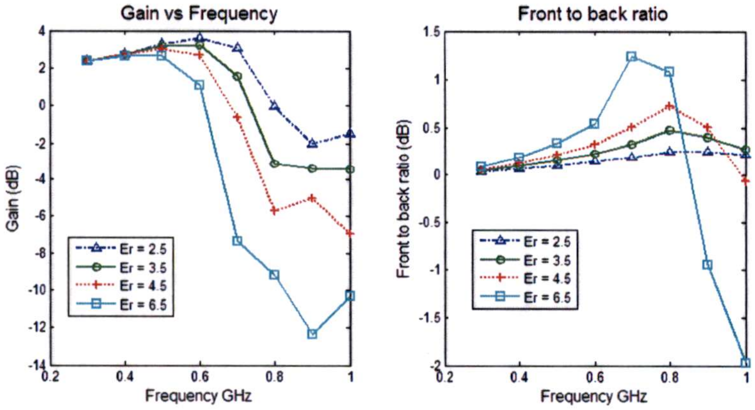

Figure 3.17: Gain and front to back ratio vs frequency for superstrate permittivities from 2.5 to 6.5.

3.5.4 Superstrate - Radome structure

Another strategy to improve the gain and front to back ratio is the inclusion of a radome. Additionally, this approach will improve the mechanical stability and protection of the system. The figure shows the cst model of the proposed structure.

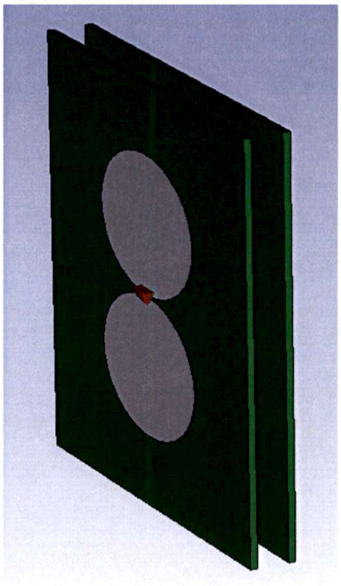

Figure 3.18: Superstrate-radome CST model

Intuitively, the operation mode structure of the superstrate plus radome can be analyzed from the multiple reflections or transmission line analogy points of view. However, both structures affect the reactive fields of the antenna, and the electromagnetic problem becomes more complicated. Therefore, the design of the structure is based on its full-wave analysis and consequent parametric studio.

The figure 3.19 shows the gain and front to back ratio for different separations between the superstrate and the radome. The superstrate and radome are dielectric layers of thicknesses 10mm and permittivity 3.5.

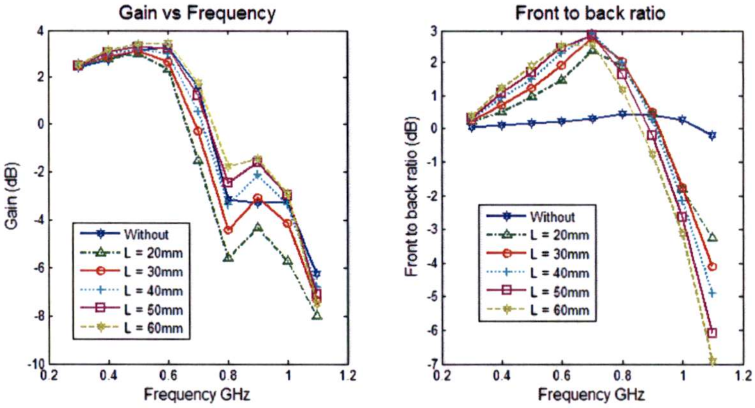

Figure 3.19: Gain and front to back ratio vs frequency. Antenna with superstrate and a radome separated by 20,30,40 and 50 mm

As it is shown, it is possible to achieve higher front to back ratios than the ones achieved with the superstrate. However, the bandwidth where the front to back ratio is greater than 0dB is reduced, due to the resonant nature of the structure.

Reducing the separation between the superstrate and radome layers strengthens the front to back ratio, although its bandwidth is reduced. On the other hand, reducing the separation between the superstrate and radome layers has a negative effect in the bandwidth in terms of gain, due to the nearness to the antenna and the influence over the near field.

The influence of the radome height is studied in the figure 3.20. In this case, the radome is placed at 50mm from the superstrate, and the superstrate has a thickness of 10mm. The figure shows that increasing the height of the radome increases the effect of the superstrate-radome structure. Therefore, the front to back ratio is enhanced, but its bandwidth is reduced. Consequently, the gain in the front direction is improved where the front to back ratio is positive, but reduced at the frequencies where it is negative.

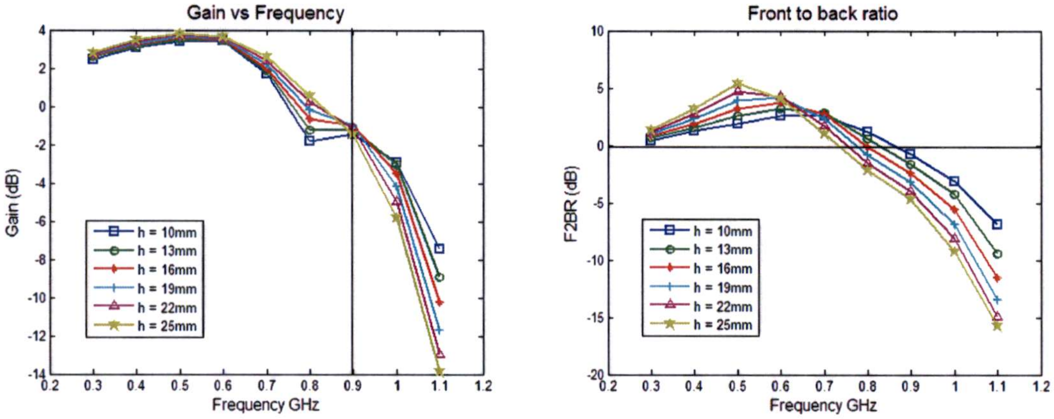

Figure 3.20: Gain and front to back ratio vs frequency. Antenna with superstrate and a radome with different heights

The results corresponding to the antenna return losses have been omitted here. The reason is that the S_{11} parameter is very close to the antenna with superstrate. Obviously, the changes in the position and height of the radome lead to changes in the antenna return losses, but the overall level is hold.

3.6 Design of the antenna feeding

3.6.1 Introduction

In the previous sections it has been shown that the presented antenna performs well as UWB antenna, gathering together good characteristics of impedance bandwidth, dispersion and radiation pattern. However, one drawback of this kind of antennas is the problems introduced by the feeding.

Firstly, the antenna is balanced feeding. If the feeding line is unbalanced, it is necessary to include a balun, and it is a complex task to design a low-loss, compact, uwb balun. Fortunately, the array geometry gives some freedom in this aspect, and a it is possible to employ a balanced feeding.

Secondly, the butterfly antenna is center fed, that is to say, a transmission line must couple to the gap between the elements. Necessarily this transmission line lies in the heart of the reactive fields surrounding the feed and is thus particularly vulnerable to undesired sheath coupling. This coupling is liable to distort the antenna pattern directly due to blockage and indirectly due to undesired cable currents.

A common solution is to incorporate the transmission-line feed into the antenna structure; the result is the bottom-fed antenna showed on the figure 3.21. Bottom-fed elliptical dipoles [9] are well suited for some commercial applications. However, the bottom-fed elliptical dipole has the feeding in the orthogonal plane to the array, so it is not adequated to the array geometry.

However, if the antenna is center fed by a small line, in comparison with the antenna, the contribution of the feeding to the noise is not so relevant. Furthermore, the center fed line do not distort the radiation pattern in the reception side, but the bottom fed does, due to its geometry.

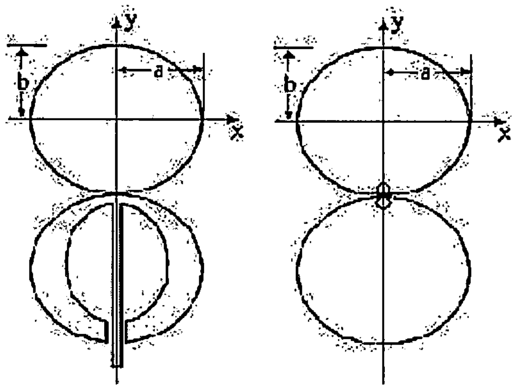

Figure 3.21: Geometry of a bottom and center-fed elliptical dipole antenna

In this thesis, the parallel plate line has been chosen as the feeding line. This is an unexpensive balanced line that suits perfectly to the geometry of the array. Furthermore, a small line can be designed to feed the antenna, so the main drawbacks of the center-fed antenna are circumvented.

3.6.2 Design of the parallel plate line

The parallel plate line is shown in figure 3.22. It is basically formed by two parallel conducting plates of width W, separated a certain distance $2H$. The gap between the conducting plates is usually filled with a dielectric, with permittivity ϵ_r. The width of the dielectric is often considered infinite, and the thickness of the plates are often neglected. These parameters describe completely the parallel plate structure, and the election of its optimal values constitutes the design of the antenna feeding.

The microstrip line and parallel plate line are shown in figure 3.22. Analyzing both structures through the image theory it is clear that the effect of the ground plane in the microstrip line is equivalent to the parallel plate line.

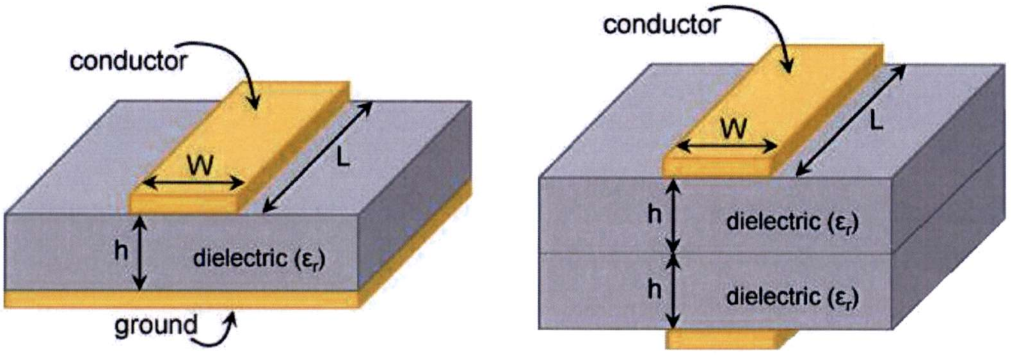

Figure 3.22: Microstrip and parallel plate lines.

Owing that it is a low-cost, easy to fabricate, and easily integrated with other passive and active microwave devices, microstrip has been the most successful of the printed technologies for the last decades. Hence, this technology has been widely studied, and there are many accurate equations and simulators to design these lines, and they can be used in the design of the parallel plate line.

As introduced in [16], it is possible to obtain the desired characteristic impedance Z_0 of the line fixing the dielectric permittivity of the substrate ϵ_r, and the ratio W/h.

$$\begin{cases} \frac{W}{h} = \frac{8 \cdot e^A}{e^{2A}-2} & for\ \frac{W}{h} < 2 \\ \frac{W}{h} = \frac{2}{\pi}\left[B - 1 - ln(2B-1) + \frac{\epsilon_r - 1}{2\epsilon_r}\left\{ln(B-1) + 0.39 - \frac{0.61}{\epsilon_r}\right\}\right] & for\ \frac{W}{h} > 2 \end{cases}$$

Where:

$$A = \frac{Z_0}{60}\sqrt{\frac{\epsilon_r+1}{2}} + \frac{\epsilon_r-1}{\epsilon_r+1}\left(0.23 + \frac{0.11}{\epsilon_r}\right)$$

$$B = \frac{377\pi}{2Z_0\sqrt{\epsilon_r}}$$

Substituing in this equations $Z_0 = 25\Omega$ and $\epsilon_r = 2.3$, the optimum W/h value is fixed at 7.64. The permittivity of the dielectric material has been chosen with a typical value. However, there is still one degree of freedom, since the W/h ratio is fulfilled with many different W and h values. In spite of this, other parameters can be calculated to resolve this ambiguity.

First, the attenuation of the line can also be calculated. It is caused by both, dielectric and conductor losses, and is calculated as follow: [16]

Attenuation due to dielectric loss:

$$\alpha_d = \frac{k_0 \epsilon_r (\epsilon_e - 1) tan\delta}{2\sqrt{\epsilon_e}(\epsilon_r - 1)}\, Np/m$$

$$\epsilon_e = \frac{\epsilon_r+1}{2} + \frac{\epsilon_r-1}{2}\frac{1}{\sqrt{1+12\frac{d}{W}}}$$

Where $\epsilon_e$is the effective dielectric constant, and $tan\delta$ is the loss tangent of the dielectric.

Attenuation due to conductor loss:

$$\alpha_c = \frac{R_s}{Z_0 W}\,Np/m$$
$$R_s = \sqrt{\frac{w\mu_0}{2\sigma}}$$

Where R_s is the surface resistivity of the conductor. The conductor losses are, in general, much more significant than the dielectric losses. Consequently, a larger value of W, or equivalently a larger value of h, yields in a smaller line losses. The figure 3.23 shows the line losses versus frequency for different line heights.

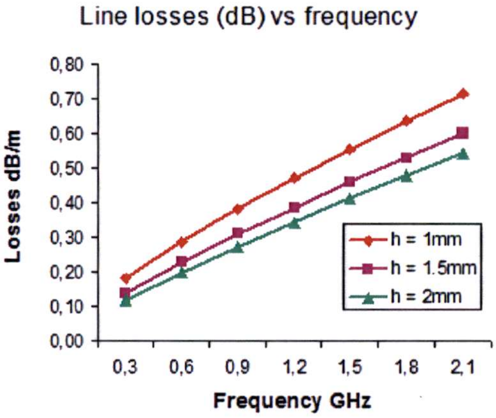

Figure 3.23: Parallel plate line losses vs frequency for different line heights. $W/h = 7.64$, $\varepsilon_r = 2.3$ and $h = 1,\ 1.5\,and\,2mm$

Furthermore, these equations have been obtained studying the line under an electrostatic field analysis. Hence, the antenna must operate within the quasi-static region. Otherwise, other effects like dispersion, excitation of higher order modes appear. The frequency which characterizes the transition from the quasi-static to the dispersion region can be approximated by [15]:

$$f_{tr} = 0.95\frac{\sqrt{Z_0}}{h\sqrt{\epsilon_r - 1}}$$

Solving this equation it is concluded that h must be smaller than 3mm to support frequencies up to 2GHz, a good limit to guarantee the operation within the region where the radiation pattern is stable.

Another aspect that must be considered is how to connect the feeding line to the antenna, since it is possible to connect it in the lower limits of the antenna flairs or inside the antenna flairs (if h is bigger than the gap between the antenna flairs). The parametric study included in the full-wave analysis of the feeding structure shows that the feeding point has influence in the matching with the antenna, and the best performance is obtained with a separation equal to the gap between the antenna flairs.

To summarize, the choice of the values of W and h that yields the ratio W/h presents a compromise between several factors.Larger values present less losses and better mechanical properties, but they also present a worse matching and bigger coupling effects. In any case, h must be smaller than 3mm. However, due to the impact of the feeding height in the antenna impedance matching, the h parameter is fixed to half of the gap between the antenna flairs.

It must be noticed that the length of the feeding line has been omitted in the design. The length of the feeding line determines the phase of the signals that are radiated, or by reciprocity, the phase of the received signals. However, in this design, the length of the feeding is not a parameter, and it is fixed by the radius of the array.

3.6.3 Full-wave analysis of the parallel plate line

In the previous subsection the parallel plate line has been designed based in the design equations for a microstrip line. In this section, the designed line is simulated with CST in order to check the results and discuss some possible variations.

Since the length of the feeding is determined by the radius of the array and the antenna mast, which are unknown, the simulations have been run with an approximated radius of 20cm.

First of, the feeding line has been modeled independently. To this a end, the line is excited with two ports, and the scattering parameters of the line are calculated. The CST model of the feeding line and the S_{11} parameter for different plate's width can be seen in figure 3.24.

As it is shown, the lowest S_{11} parameter is obtained with W taking the value of the design equations. Unfortunately, the S_{11} parameter does not show a flat response with frequency. The explanation to this phenomena comes from the dispersive nature of the pseudo-TEM mode excited in the parallel plate line, which yields in a dependency of the line impendance with frequency. Due to the impedance mismatch, standing waves are excited in the line, and the S_{11} parameter shows this resonant shape. In spite of this, the S_{11} parameter shows a low level, below $-20dB$, over all the operational bandwidth.

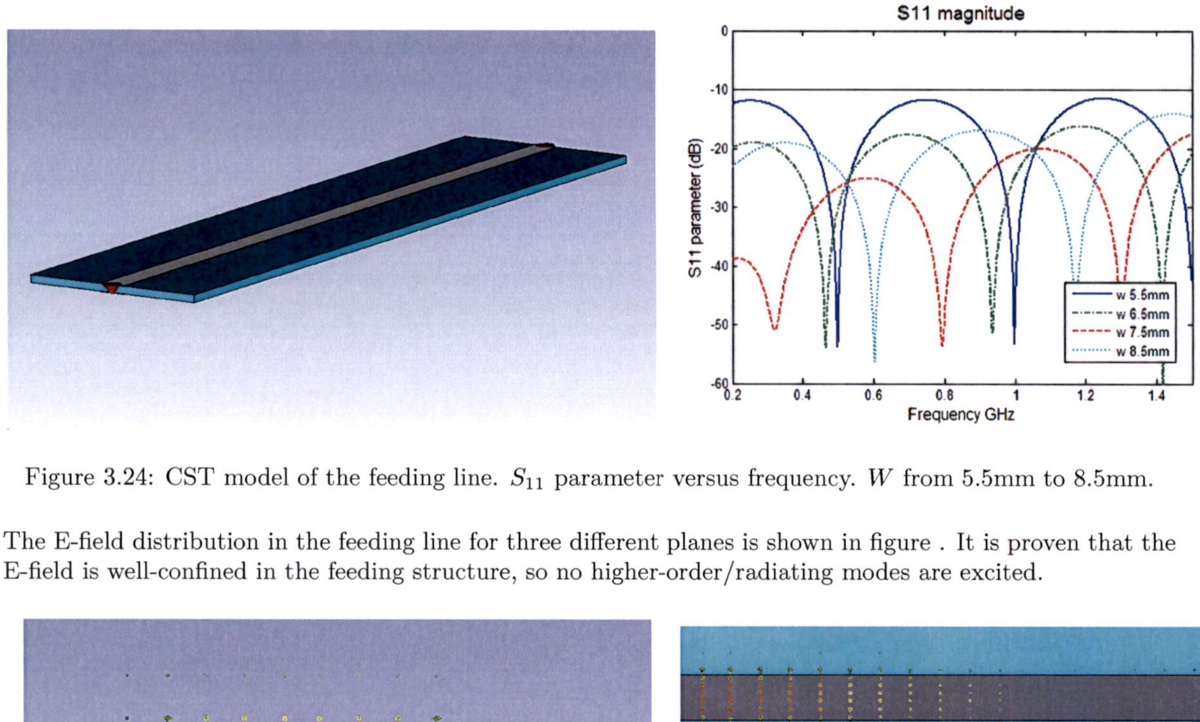

Figure 3.24: CST model of the feeding line. S_{11} parameter versus frequency. W from 5.5mm to 8.5mm.

The E-field distribution in the feeding line for three different planes is shown in figure . It is proven that the E-field is well-confined in the feeding structure, so no higher-order/radiating modes are excited.

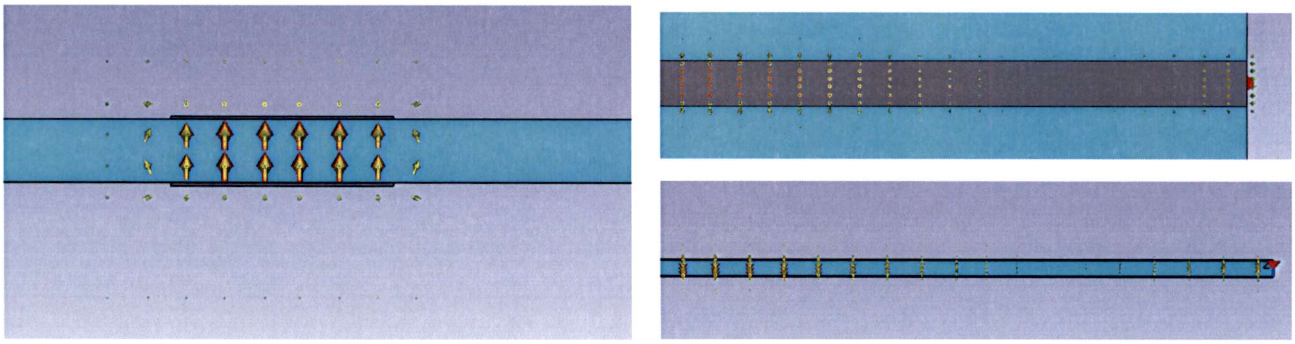

Figure 3.25: E-field distibution in the parallel plate line.YZ, XY and XZ planes.

This results concludes the design and characterization of the feeding line. However, the influence of the feeding in the antenna performance must be checked. To this end the feeding is conected to a ellipticaly shaped dipole antenna of minor radius of 95mm, gap between the antenna flairs of 2mm and eccentricity of 1.4.

As anticipated in the previous section, the height of the feeding must be optimized. To this end, the effect of the feeding in the antenna impedance matching must be studied. The antenna return losses with a feedin height from 1 to 3mm can be seen in figure. Obviously, the feeding height has a great impact in the antenna return losses, and the best matching is obtained with a feeding height equal to the separation between the antenna flairs.

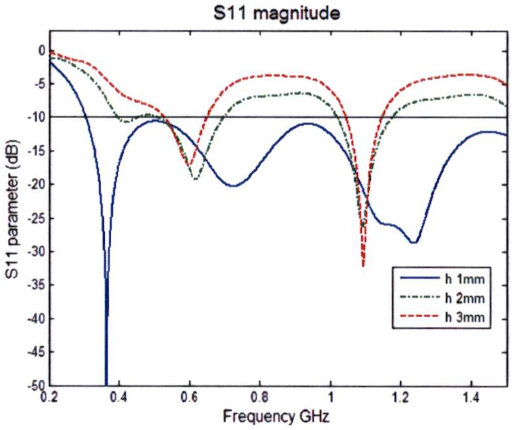

Figure 3.26: Antenna return losses for different feeding heights.

The antenna performance is shown in figure 3.27. There is a small degradation in the antenna return losses, but the overall performance is almost the same, and the level under $-10dB$ is hold. Additionaly, it is shown that there is no degradation in terms of gain.

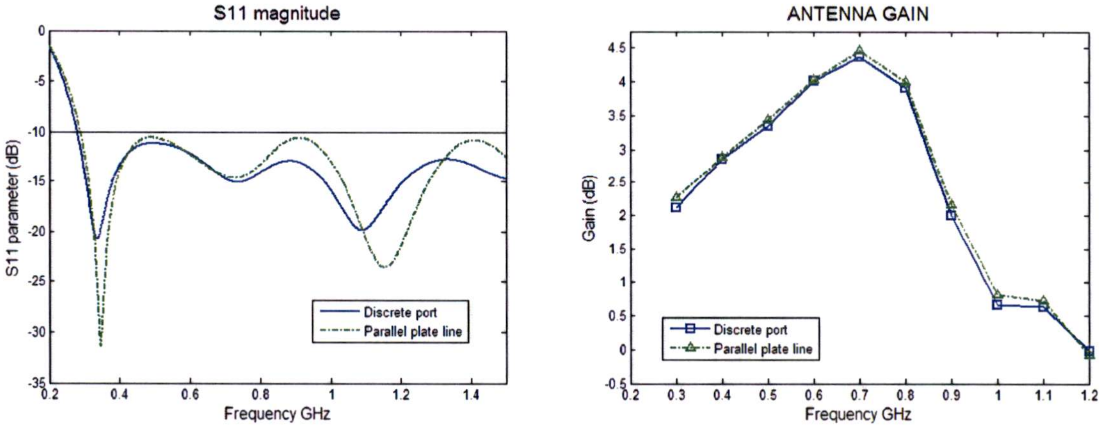

Figure 3.27: Antenna return losses and gain in the front direction. Antenna fed with a parallel plate line.

3.7 Antenna optimization

The previous sections have presented a complete analysis of all the parameters of the elliptically shaped antenna, the cover, the curvature radius and the antenna feeding. Based on all this knowledge it is possible optimize the antenna for direction finding applications. In this section the radiation and circuital characteristics of the proposed antennas are presented.

Particularly, two different antennas has been developed, one for a subarray covering from 250MHz to 900MHz and the other one for a subarray covering from 900MHz to 3.5 GHz. These antennas will be employed as the single element antenna for the array design.

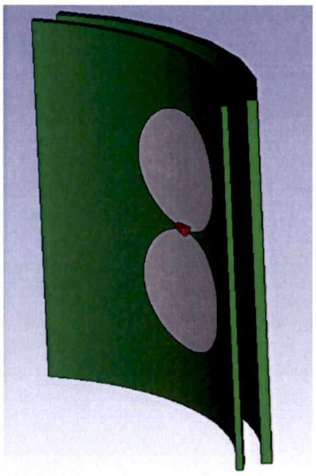

Figure 3.28: CST model of the proposed antenna.

The CST model of the proposed antennas is shown in the figure 3.28. The antenna final dimensions are gathered together in the table 3.2.

VARIABLE	**1^{st} SUBARRAY**	**2^{nd} SUBARRAY**
Radio	95mm	27mm
Eccentricity	1.1	1.1
Gap	2mm	1mm
Superstrate ϵ_r	3.5	3.5
Superstrate height	10mm	2.6mm
Radome height	16mm	4.3mm
Radome separation	45mm	12mm
Curvature radius	45cm	13cm

Table 3.2: Antenna final dimensions.

The antenna return losses versus frequency of the proposed antennas are shown in the figure 3.29. Both antennas show a good impedances matching over all the operational bandwidth.

The figures 3.30 shows the gain and front to back ratio of the proposed antennas. As it is shown, the gain is greater than 0dB from 250MHz to 900MHz for the first subarray, and from 900MHz to 3GHz for the second subarray. Moreover, the front to back ratio is grater than 0dB from 250MHz to 950MHz, with a peak of 9 dB, for the first subarray; and from 900MHz to 3.4GHz, with a peak of 8dB, for the second subarray.

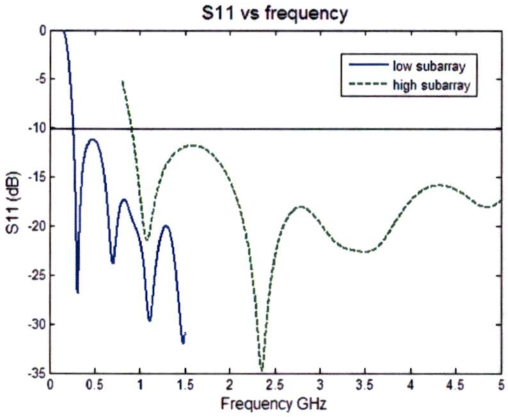

Figure 3.29: Antenna return losses versus frequency.

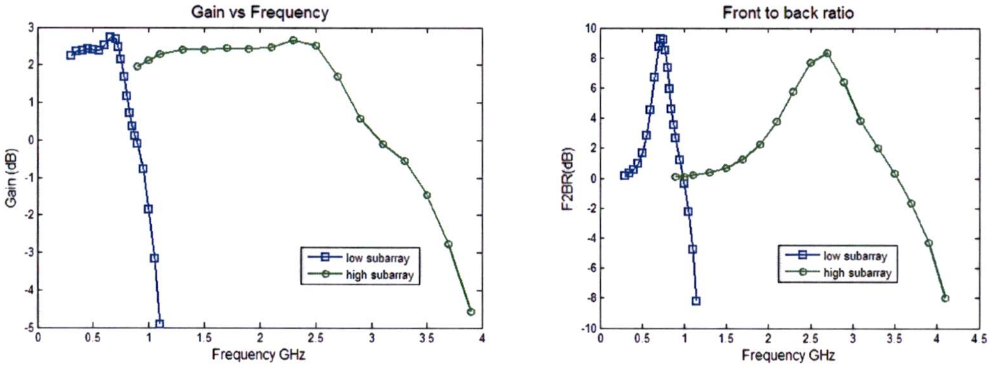

Figure 3.30: Gain in the front direction and front to back ratio of the proposed antennas.

The figures 3.31 and 3.32 shows the radiation patterns in the E and H plane of the proposed antennas. In both antennas the radiation pattern is dipole like at the lowest frequencies of operation. As the frequency is increased the radiation is more concentrated in the front radiation and front to back ratio and directivity are enhanced. Finally, at the very highest frequencies the some lobes appear, and the radiation is also concentrated toward the $\phi = \pm 90^o$ directions.

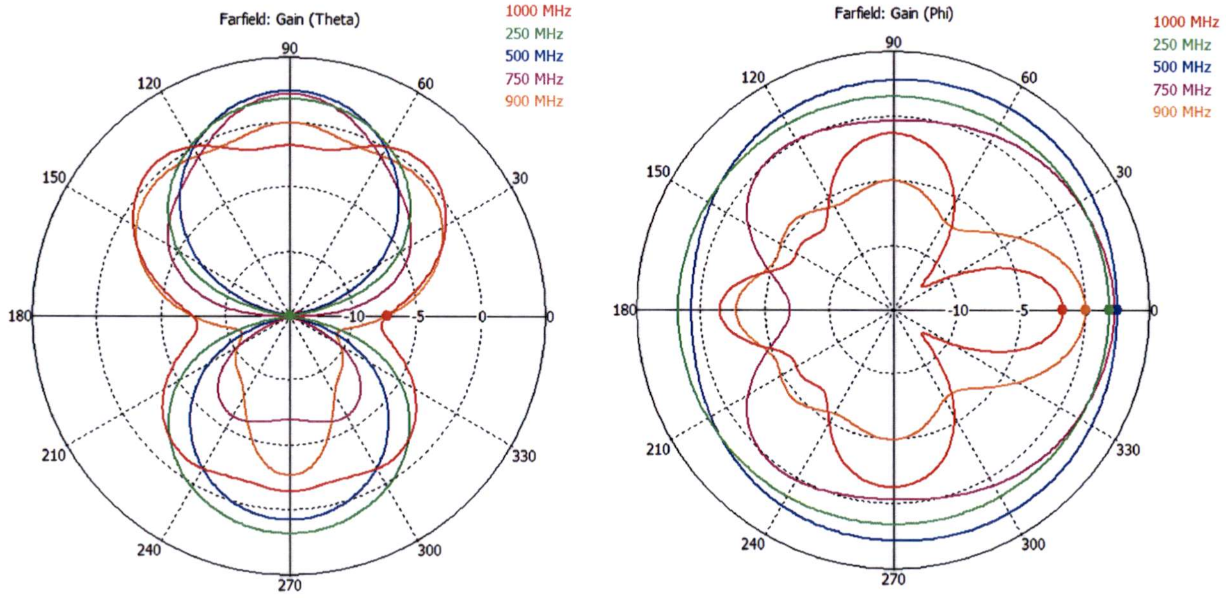

Figure 3.31: Radiation patterns of the first subarray in the E and H planes.

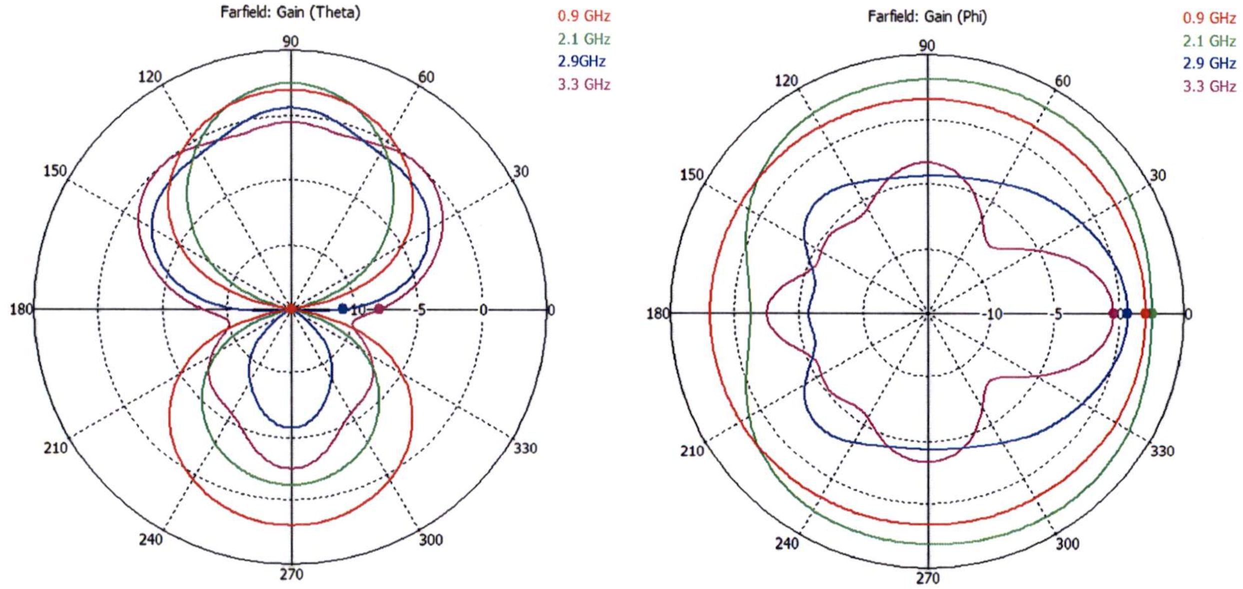

Figure 3.32: Radiation patterns of the second subarray in the E and H planes.

Chapter 4

Algorithms for DOA estimation

4.1 Introduction

This chapter gives to the reader an introduction to the signal processing techniques and the difficulties in DOA estimation with antenna arrays. To this end, it is included a briefly introduction, a description of the technique implemented in thesis, the MUSIC algorithm, and its extension to ultra-wideband DOA estimation.

The problem of DOA estimation by observing the received signals with spatially separated signal has attracted a great deal of attention of research interest due to its application in many fields such as radar, sonar, mobile communications, radio astronomy and seismology. Hence, many different techniques have been developed for DOA estimation. Just to mention some of them, these techniques include methods such as spectral estimation, minimum-variance distortionless estimator, linear prediction, maximum entropy, maximum likelihood and eigenstructure methods such as the many versions of MUSIC algorithms, minimum norm methods, CLOSEST method, ESPRIT method and the weighted subspace fitting method. Nowadays, the development of algorithms for DOA estimation constitutes an open research topic.

Among all of them, the MUSIC algorithm is the most studied and popular algorithm. Moreover, it can be shown that the variance in the DOA estimation is comparable or inferior to the variance of other techniques and its computational burden is inferior to other methods such as maximum likelihood. Furthermore, the MUSIC algorithm is employed as a reference to design antenna arrays and calibration techniques in numerous papers, and thus makes the design comparable with other systems. Additionally, some of the most popular wideband techniques, such as the Coherent Signal-Subspace Method (CSSM), are compatible with the MUSIC algorithm.

4.2 The MUSIC algorithm

4.2.1 Introduction

The algorithm implemented in this thesis is the MUltiple Signal Classification (MUSIC). It was introduced by Smith in 1986 [17]. The MUSIC algorithm has been proposed for applications such as cellular mobile communications [20] and mobile satellite communications [19]. It is a popular high resolution eigenstructure method, the most studied, and has many variations.

MUSIC promises to provide unbiased estimates of the number of signals, the angles of arrival, polarization and the strengths of the waveforms. Furthermore, it is independent of the array geometry. However, the performance of MUSIC is poor in the presence of correlated signals, and it fails to detect coherent arrivals.

For a single source, the MUSIC estimation asymptotically approaches the Cramer-Rao lower bound (CRLB), that is to say, for a infinite large number of snapshots, the best possible estimate is achieved. A snapshot is defined as the measured voltages at the outputs of the sensors at one determined instant. For multiple sources, the estimate approaches the CRLB just for large SNR. The CRLB is the theoretical lowest value of the covariance for an unbiased estimator.

4.2.2 The algorithm

In this subsection the MUSIC algorithm is briefly described. Firstly, it is necessary to introduce the data model. The waveforms received in an array of M antennas, due to D incident signals is described by the equation:

$$X = A \cdot F + W$$

Where X is the $M \times L$ voltage matrix measured by the M antennas, F is the $D \times L$ vector representing the D incident waveforms, W is the noise vector, and A is the called steering matrix, that gives the array response to the incident signals. Each column of A is the response of the array for one angle of arrival and is called steering vectors. L is the number of snapshots, that its to say, the number of measurements.

Equally, this equation can be written as a time function. The voltage exited at a certain instant of time at the j antenna is $x_j(t)$:

$$x_j(t) = \sum_{i=1}^{D} a_j(\theta) \cdot s_i(t) + n(t)$$

Where θ_i is the DOA of the i impinging signal, $s_i(t)$. And $a_j(\theta_i)$ is the response of the j antenna in the θ_i direction, for a uniform circular array of radius R. For an azimuth-only case, it is defined as:

$$a_j(\theta_i) = g(\theta_i - j \cdot \tfrac{2\pi}{M}) \cdot e^{jkRcos(\theta_i - j \cdot \frac{2\pi}{M})} = a_{ji}$$

Defining a_{ji} as the j-i element of the matrix A, and $g(\theta)$ as the voltage induced in the antenna element by a impinging signal in the θ direction.

Although an azimuth-only detection has been described here for simplicity, the MUSIC algorithm works in both in azimuth and elevation spaces when detecting the angle of arrival of an incoming signal.

Once the X vector is measured, it is possible to calculate the S array correlation matrix:

$$S \triangleq \overline{XX^*} = A\overline{FF^*}A^* + \overline{WW^*}$$

At this point two important algebraic properties of the array correlation matrix are invoked. First, the spaced spanned by the eigenvector of the array correlation matrix mat be partitioned in two orthogonal subspaces, the signal subspace and the noise subspace. Second, the subspace of noise is spanned by the smallest eigenvalue, with multiplicity equal to the dimension of the subspace.

In the practice, the noise subspace is spanned by a cluster of similar values, but not identically equal. Nevertheless, the eigenvalues of the noise subspace are smaller than the eigenvalues corresponding to eigenvectors, and it is possible to identify the noise subspace defining an adequate threshold.

It must be noticed that $\overline{FF^*}$is diagonal when the signals are uncorrelated, nondiagonal and nonsingular when the signals are partially correlated and nondiagonal but singular when some signals are fully correlated (or coherent). If the $\overline{FF^*}$ matrix is singular, the rank of the S matrix is reduced, and these two properties could not be applied. Therefore, the algorithm fails to detect coherent signals.

If the dimension of the noise subspace is N, then the number of signals D, is easily calculable: $D = M - N$. Finally, the called music spatial spectrum $P_{MU}(\theta)$ can be calculated to find the direction of arrival of the incident signals:

$$P_{MU}(\theta) = \frac{a(\theta)^* \cdot a(\theta)}{a(\theta)^* \cdot E_N E_N^* \cdot a(\theta)}$$

Where E_N is a $N \times M$ matrix whose columns are the N noise eigenvectors, and $a(\theta)$ is the steering vector of the direction θ.That is to say $a(\theta) = [a_1(\theta)....a_M(\theta)]$, equal to a column of the matrix A. Since $a(\theta)^* \cdot E_N E_N^* \cdot a(\theta)$ is the projection of $a(\theta)$ over the noise subspace, the DOAs are found in the local maximums of the music spectrum.

An example of the MUSIC spectrum is shown in the figure 4.1. As it should be noticed, this is the spectrum for two incoming signals at the directions 100 and 110°, with a SNR of 20dB. The sharpness of the peaks is a symbol of the high resolution achieved with this algorithm.

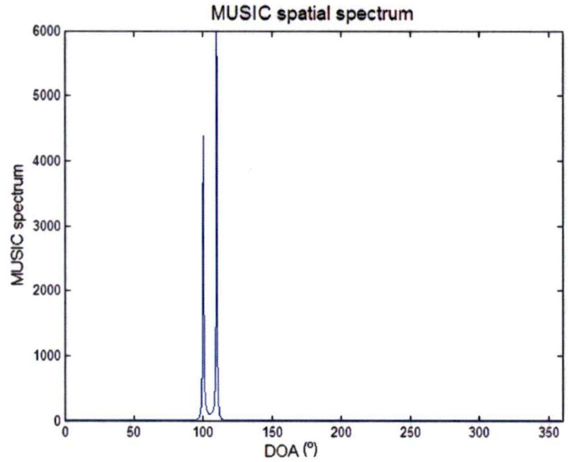

Figure 4.1: MUSIC spatial spectrum. Two signals at 100 and 120°. Superposition of 10 estimations.

Identically, it is possible to extend the search to azimuth and elevation. In that case, the steering vectors contains azimuth and elevation unknowns, and the MUSIC spatial spectrum becomes 2D. As it can be deduced in the expresion of the steering vector, these system presents an ambiguity in the elevation angle. The figure 4.2 shows the 2D-MUSIC spectrum for two incoming signals in the directions $\phi = 100$, 110° and $\theta = 70$, 75° with a SNR of 20dB.

$$a_j(\theta,\phi) = g(\phi - j\tfrac{2\pi}{M},\theta) \cdot e^{jkRsin(\theta)cos(\phi - j\frac{2\pi}{M})}$$

Once the DOA of the incident signals are known, it is possible to construct the matrix A, and thus to calculate the remaining parameters of the incoming signals. For instance, the cross-correlation can be obtained from the following equation:

$$\overline{FF^*} = (A^* \cdot A)^{-1} A^* (S - \lambda_{min} S_0) \cdot A \cdot (A^* \cdot A)^{-1}$$

4.2.3 Noise subspace threshold

As anticipated, the array correlation matrix can be spanned in two different spaces, the signal subspace and the noise subspace. Furthermore, the noise subspace is formed by one eigenvalue with multiplicity equal to $M - D$, the difference between the number of sensors and the number of signals. As a consequence of this property, the number of signals and its DOAs can be calculated characterizing the noise subspace.

However, in practice the eigenvalues of the noise subspace are not identical, but they form a cluster with similar values. Therefore, a threshold must be defined in order correctly separate the noise subspace and

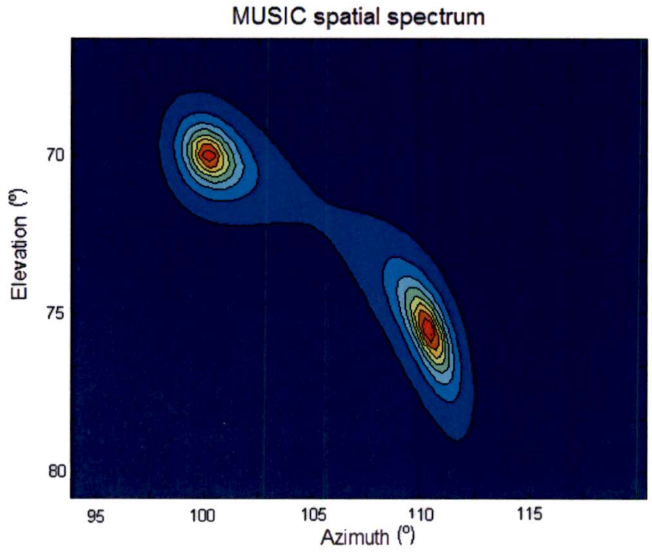

Figure 4.2: MUSIC spatial 2D spectrum.

the signal subspace. It would be desirable to have a unique threshold for all the possible scenarios, but the influence of several factors such as SNR, radiation pattern and number of snapshots must be studied.

In the figure 4.3 the DOA estimation has been carried out for SNRs 0, 3, 10 and 20dB, and noise subspace thresholds from 1.1 to 10. It can be appreciated that for low subspace thresholds the detection fails, because some noise eigenvalues are considered signal eigenvalues which leads to and incorrect number of signals estimation. It is also shown that for low SNRs the detection fails for the highest values of the noise subspace threshold. The reason for this is that with low SNRs the signal eigenvalues are less separated from the noise eigenvalues, and some signal eigenvalues are considered noise eigenvalues.

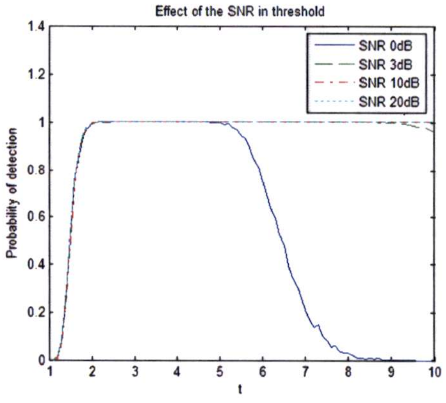

Figure 4.3: Effect of the SNR in the noise subspace threshold..

It would also be desirable to have the same threshold for along all the operational bandwidth. However, this implies that the properties of the eigenvectors of the array correlation matrix must be independent on the radiation pattern and frequency. To check this, the figure 4.4 show the probability of detection versus the threshold value. As can be inferred from the graph, all the lines are identical at the lower values of the threshold, but differ at the higher values. Hence, it can be concluded that the properties of the noise subspace are independent of the radiation pattern and frequency, but the separation between the signal and noise eigenvalues is a function of them. At frequency of 900MHz the signal and noise subspace have collapsed, and the detection is not possible for any value of the threshold.

The effect of the number of snapshots is shown in the figure 4.5. The array correlation matrix is estimated by a limited number of snapshots, so larger number of snapshots, the more accurate description of the matrix. As a consequence, it is shown in the picture, the effect of increasing the number of snapshots is a more pronounced slopes in the lines. The meaning of the increasing in the slope is that both, the noise and signal eigenvalues, became closer, due to the better estimation of the actual correlation matrix. (Ideally all noise eigenvalues would be the same). In conclusion, increasing the number of snapshots let diminish the threshold value.

The figure 4.6 shows the behavior of the threshold with the number of sensors. Logically, increasing the number of sensor yields in steering vectors with more dimensions, so both, the noise and signal eigenvalues have larger values. However, the difference between them is also larger.

In conclusion, the noise subspace threshold can be maintained for different frequency, radiation pattern and signal to noise ratio. However, it must be recalculated for variations in the number of snapshots and number of sensors.

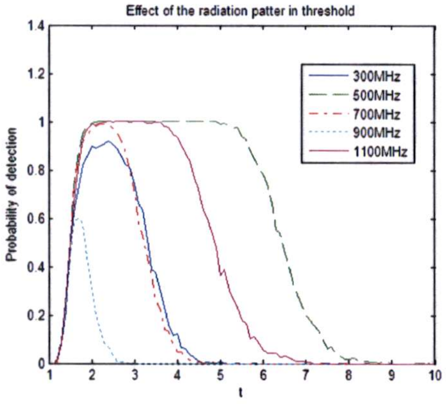

Figure 4.4: Effect of the radiation pattern and frequency in the noise subspace threshold.

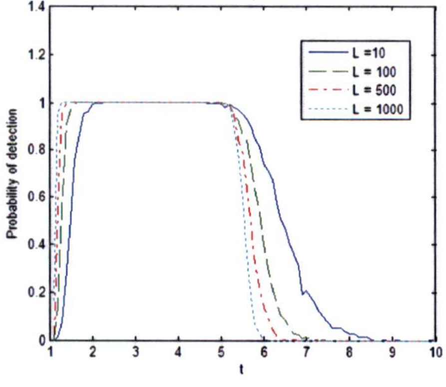

Figure 4.5: Effect of the number of snapshots in the noise subspace threshold.

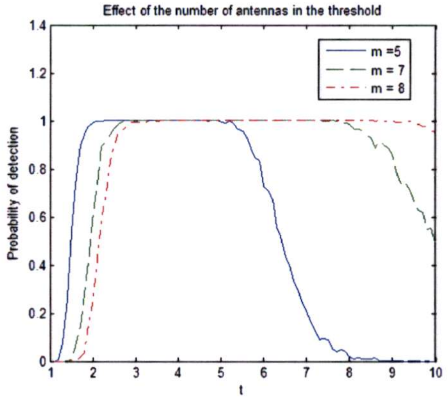

Figure 4.6: Effect of the number of sensors in the noise subspace threshold.

4.2.4 Variations of the MUSIC algorithm

The previous subsection has introduced the MUSIC algorithm as was firstly defined by Schmidt in 1986. However, due to the popularity of this algorithm there are many variations, that try to apply it to more specific problems and solve the weaknesses. In fact, the evolution of this algorithm is an open research topic.

In [30], some of the most relevant variations are gathered together. The original MUSIC algorithm is called spectral MUSIC.

Root-MUSIC

This variation is only applicable to uniformly spaced linear arrays (ULA). The search of the DOAs is made finding the roots of a polynomial instead of finding location of spectral peaks. Root-MUSIC has better performance than spectral MUSIC.

Constrained MUSIC

This variation is only applicable when at least one of the DOAs of the incoming signals is known. Then, the components induced by the known signals are removed and the data matrix is replaced by a modified data matrix. Estimation is achieved by projecting the data matrix onto a orthogonal complement to a spaced spanned by the known signals. This method reduces the complexity of the process decreasing the dimension of the signal space. The quality of the estimation is superior, specially when know and unknown sources are strongly correlated, what it is useful to evaluate multipath environments.

Beam Space MUSIC

In this variation the array data is passed through a beamforming processor before applying MUSIC. The data of the output of the processor is referred to a set of beams instead to a set of antennas. Hence, the number of elements can be reduced to $M + 1$ to resolve M sources, reducing the computational burden. Furthermore, this method has other advantages such as improved resolution, reduced sensitivity to system errors, reduced resolution threshold and reduced bias of the estimate.

This variation is a general method that can be applied in other eigenstructure methods and variation of the MUSIC algorithm like Root-MUSIC.

4.2.5 Performance of the MUSIC algorithm

As anticipated, the MUSIC algorithm is supposed to be an unbiased superresolution algorithm. For a single source, the MUSIC estimation asymptotically approaches the Cramer-Rao lower bound (CRLB), that is to say, for a infinite large number of snapshots, the best possible estimate is achieved. For multiple sources, the estimate approaches the CRLB just for large SNR. The CRLB is the theoretical lowest value of the covariance for an unbiased estimator.

This algorithm is able to capture signals at very low SNR, several signals simultaneously and spaced less than the beamwidth. It is also a general algorithm that can be applied to any array geometry, and any signal with different strength, polarization, frequency, modulation and AOA.

However, the DOA estimation is poor with correlated signals and fails to detect coherent signals. In spite of this, in some applications such as multipath environments or smart jammers the DOA estimation of strongly correlated signals is required. In this cases the MUSIC algorithm can be modified, typically including spatial smoothing [32, 33]. Moreover, there are some other newer algorithms, some of them evolutions from MUSIC, that can deal with this scenarios [34, 35]. In spite of this, it is out of the scope of this thesis to study the robustness of the MUSIC algorithm in front of coherent signals, so incoherent signals with a simple FM modulation are employed.

Obviously, the performance of the MUSIC algorithm is dependent of the array geometry, and the selection of the adequate number of antennas and array radius is critical for the system performance. In general, increasing the number of antennas and the array radius yields in an improvement of DOA estimation. In fact, the MSE error is reduced monotically. Although this fact can seem evident, it must be notice that the same is not hold for other eigenstructure methods such as Min-Norm and non-overlapped ESPRIT.

In spite of this, the array size cannot be increased without control, because big aperture arrays may induce ambiguities. An ambiguity is produced when one steering vector or the linear combination of a certain number of steering vectors is equal to other steering vector of the same steering matrix. In this situation the DOA estimation automatically fails.

The ambiguities can be classified by its rank. A rank-k ambiguity is produced when a linear combination of k steering vectors is also a steering vector of the same steering matrix [21]. Unfortunately, it is not possible to obtain the probability of ambiguity for a given structure, and the ambiguity problem remains unsolved.

First, although it could be computed through the steering matrix, the computational cost makes this option impractical. A one-dimensional steering matrix with a resolution of 0.1º has 3600 steering vectors, so the number of possibles combinations is too elevated.

In [24] and [25] it is shown how to build an array free of rank-1 and rank-2 ambiguities. However, the array configurations are not always practical. A more general approach is introduced in [36], showing conditions to obtain a star array free of rank-k ambiguities. However, concentric and non-uniform circular arrays are needed, so this solution is not practical for small and compact systems.

In the practice the systems include ambiguities in some grade, and measure of the ambiguity are employed to minimize its effects in the probability of detection and signal to noise ratio [22]. However, most of this measures are based in omnidirectional antennas.

The number of snapshots also has influence in the algorithm performance. The best performance is obtained with the largest number of snapshots. However, the use of a large number of snapshots increases the computational cost and collection time. In some applications, such as Radar and Sonar, sometimes there are just two or one snapshots available, and modifications of the MUSIC algorithm and new algorithms are needed.

Single-snapshot DOA estimation is possible with the Matrix Pencil Method [26], and the preprocessing technique special smoothing [28]. These techniques have been applied recently and can deal with coherent signals. [29, 27]. In this thesis a medium number of snapshots, $L = 100$, is employed.

The MUSIC algorithm, as other super-resolution algorithms is based in a perfect knowledge of the steering matrix. Hence, these sorts of algorithms are strongly influenced by variations in the steering matrix. In fact, errors in the phase, gain and positions of the sensors and a bad characterization of the coupling effects between the array elements degrade the system performance dramatically.

In [18] a study of the impact of these errors in the MUSIC algorithm performance is presented. In order to give a measure of the effect of the errors in the system performance, the sensitivity magnitude is defined as the ratio of the error in the DOA estimate and the error introduced in the parameters.In this article it is concluded that: first, the sensitivity decreases as the number of elements is increased. Second, the sensitivity is inversely proportional to the array aperture (or equivalently, element spacing). And finally, the sensitivity is inversely proportional to the source separation if the separation is smaller than the array beamwidth.

However, although this article gathers together some interesting results, it assumes that there is only impinging signal and that the probability of detection is close to one. A more recent analysis of the MUSIC algorithm performance in the presence of modeling errors is found in [31]. The algorithm is proved to be biased in the presence of several signals and modeling errors. Moreover, analytic expressions of the RMS error and the bias are introduced.

4.3 Ultra-Wideband DOA estimation

The previuos section has described the MUSIC algorithm for DOA estimation, which is the algorithm that will be employed for the array design. However, this algorithm has two major drawbacks: first, it is a narrowband technique, so it is not able to handle ultra-wideband signals. Second, it is not able to detect strongly correlated signals, which are likely to appear in multipath scenarios.

In 1986, Wang and Kaveh [37] proposed a technique referred to as coherent signal-subspace method (CSSM) able to handle wideband coherent sources. Moreover, the coherence problem is solved without reducing the effective array aperture. The main difficulty in developing coherent signal-subspace processing is due to the fact that the signal-subspace changes with frequency. The basic idea to overcome this problem is to apply a linear transformation to the array power spectral density (PSD) matrix estimated at each frequency bin, with the purpose of removing the frequency dependence of the transformed signal-subspace and creating a single universal matrix having desired algebraic properties that can be exploited in detection of the number of signals and estiamtion of DOA.

The data model for wideband signals is the following:

$$x_m(t) = \sum_{d=1}^{D} s_d(t - \tau_{md}) + n_m(t)$$

Where is $x_m(t)$ is the measured voltage ate the m-th antenna, $n_m(t)$ a zero-mean, stationary, random process representing the noise field at the mth sensor, and τ_{md} the delay of the d-th signal at the m-th antenna, for a UCA:

$$\tau_{md} = -\frac{R \cdot cos(\theta_d - (m-1) \cdot \frac{2\pi}{M})}{c}$$

These signals are sampled with a frequency f_c and divided in K non-overlapping blocks with J samples each. Subsequently, a J-points discrete Fourier transform (DFT) is applied to each segment by producing $\tilde{X}_k = X_k \cdot F_J^T = [\tilde{x}_k[0], \ldots, \tilde{x}_k[J-1]]^T$, where the matrix F_J^T is the J-points DFT matrix operator and the vectors $\tilde{x}_k[j]$ are referred to as frequencydomain array signal vectors.

$$\tilde{x}_k[j] = A\left(\theta, f_j\right) \cdot S_k[j] + N_k\left[j\right]$$

And it can be shown, that the correlation matrix of $\tilde{x}[j]$ can be written as:

$$R_{\tilde{x}[j]\tilde{x}[j]} = R_j = A\left(\theta, f_j\right) \cdot S_k[j] \cdot S_k^H[j] \cdot A^H\left(\theta, f_j\right) + N_k\left[j\right] \cdot N_k^H\left[j\right]$$

The main problem is that each frequency bin has a different signal subspace. CSM attempts to transform these subspaces using appropriate matrices in order to align them. This procedure is referred to as focusing, and the transformation matrices are called focusing matrices.

$$T_j \cdot A(\theta, f_j) = A(\theta, f_0)$$

And thus an universal correlation matrix can be created, this space shows the same algebraic properties than the array correlation matrix in narrow-band MUSIC. Therefore, the MUSIC algorithm can be applied over this space, being able to resolve ultra-wideband coherent signals.

$$R = \sum_{j=1}^{J} w(j) \cdot T_j \cdot R \cdot T_j^H$$

Where the applied window $w(j)$ can be optimized.

However, the selection of the focusing matrices is not trivial. In general, heavy iterative processes and an initial estimation of the incident DOAs is required. The development of simple but lossles focusing matrices has been an open research topic during many years, where the most important findings can be found in [37, 38, 39, 40, 41, 42]. More recently (October 2008), a non-iterative technique that does not require preprocessing has been introduced [43], this is the procedure implemented in this thesis.

In this technique, the focusing matrices are chosen to satisfy:

$$T_j \cdot A(f_j) \cdot S[j] = A(f_0) \cdot S[0]$$

Where f_0 is the reference frequency. Although the selection of this frequency can be optimized, in this thesis f_0 is set at the central frequency of the band for sake of simplicity. Furthermore, the crosscorrelation matrix between $\tilde{x}[j]$ and $\tilde{x}[0]$ can be written as:

$$R_{\tilde{x}[j]\tilde{x}[0]} = E\left[\tilde{x}[j]\tilde{x}^H[0]\right] = A(f_j) \cdot E\left[S[j]S^H[0]\right] \cdot A^H(f_0)$$

Multiplying by $S^H[0] \cdot A^H(f_0)$ and computing the expectation:

$$T_j \cdot A(\theta, f_j) \cdot E\left[S[j] \cdot S^H[0]\right] \cdot A^H(f_0) = A(\theta, f_0) \cdot E\left[S[0] \cdot S^H[0]\right] \cdot A^H(f_0) \triangleq P_0$$

$$T_j \cdot R_{\tilde{x}[j]\tilde{x}[0]} = P_0$$

Where this problem has already been solved in [44], with solution:

$$T_j = R_{\tilde{x}[j]\tilde{x}[0]} = P_0 \cdot (P_0 \cdot P_0^H)^{-1/2} \cdot \left(R^H_{\tilde{x}[j]\tilde{x}[0]} \cdot R_{\tilde{x}[j]\tilde{x}[0]}\right)^{-1/2} \cdot R_{\tilde{x}[j]\tilde{x}[0]}$$

Finally, $R_{\tilde{x}[j]\tilde{x}[0]}$ and P_0 can estimated as follows:

$$R_{\tilde{x}[j]\tilde{x}[0]} = \frac{1}{K} \sum_{k=1}^{K} \tilde{x}_k[j]\tilde{x}_k[0]$$

$$P_0 = R_{\tilde{x}[0]\tilde{x}[0]} - \sigma^2 I$$

Where $R_{\tilde{x}[0]\tilde{x}[0]} = \frac{1}{K} \sum_{k=1}^{K} \tilde{x}_k[0]\tilde{x}_k[0]$ and σ^2 is determined by averaging the $M - P$ smallest eigenvalues of the pencil $(R_{\tilde{x}[0]\tilde{x}[0]}, I)$.

Chapter 5

Algorithm-oriented array design

5.1 Design procedure

In the previous chapter the MUSIC algorithm for DOA has been introduced. Moreover, the performance of the MUSIC algorithm and the factors that influence the DOA estimation have also been adressed there. At this point, it is possible to employ all this knowledge to carry out the antenna array design.

It must be remarked that the array design presented here is focused on the enhancement DOA estimation performance. Therefore, the design will be adequate for DF applications, where the DOA estimation is the most important feature. For other sort of applications, such as smart radio systems, the array design must be adapted to fulfill other systems requirements, for example, beamforming performance.

An Uniform Circular Array (UCA) geometry is adopted. As anticipated, circular arrays present advantages for RDFs such as complete azimuth coverage and symmetrical performance with respect to the DOA estimation. Moreover, the DOA estimation performance is proven to be better than in other array geometries under the normalization of array aperture and number of elements [59]. However, the coupling effects are typically larger.

Analyzing the structure of a UCA, figure 5.1, the design objective consists on determining the optimum radius and number of elements. Although the design parameters could be extended varying the position of the antennas, forming a non-uniform array it would induce a dependency of the DOA estimation performance with the AOA, annulling one of the main advantages of circular arrays.

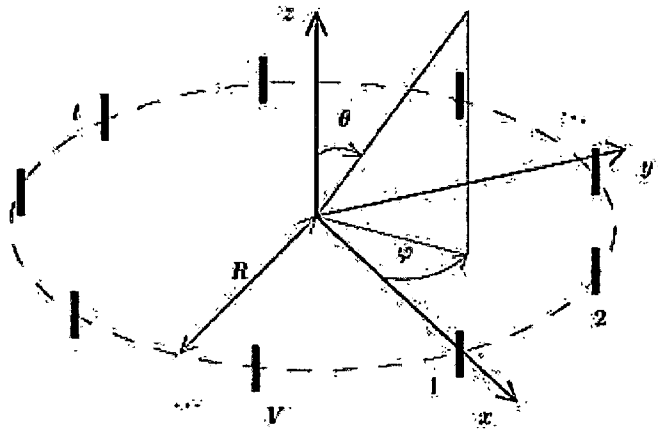

Figure 5.1: Uniform Circular Array geometry.

In spite of this, the UCA design for DOA estimation is a cumbersome task. Although there are only two parameters to fix, there are a huge amount of variables which have influence in the DOA estimation. Firstly, the incoming signals can obey to very different nature, varying its frequency, number, power, SNR, separation and cross-correlation. Secondly, the characteristics of the receptor are variable: antenna characteristics and array aperture are functions of frequency. Other parameters internal to the algorithms, such as the number of snapshots, could be modified.

However, the array have to operate in all these possibl scenarios. Therefore, Monte Carlo Methods are usually employed to design the arrays. A population and a probability density function is defined for each variable, and heavy simulations are carried out to optimize the array in terms of probability of detection (PoD) and mean square error (MSE). The main drawbacks of this methods are the enormous quantity of resources, time and memory, employed, and the difficulty to understand both, the physical operation of the system and the actual limitations in the DOA estimation.

In this thesis a group of signals is considered detected if the number of signals is correctly estimated and the MSE is smaller than 100, that is to say, if the error in the DOA estimation is smaller than 10º. Under this definition, the PoD is computed and the accuracy of the detection is computed recording the MSE of the estimations.

Therefore, in this thesis a different array design procedure is proposed. Instead of calculating the MSE and the PoD for a combination of all possible variables, both measures are calculated in order to determine three basic features of the system:

1. The minimum SNR of operation.
2. The minimum detectable separation between signals.
3. The maximum detectable number of signals.

This analysis gives to the designer an accurate description of the system limitations. In any case, the mean behavior of the system can be quickly check for the optimized array with a complete population definition.

In order to analyze each line with independence of the other ones, the other variables are fixed under good conditions. For the minimum SNR of operation the analysis is carried out with well-separated signals (20º), the minimum separation between signals is carried out with a high SNR (20dB) and the maximum number of signals is detected with 20º of separation and 20dB of SNR.

In general, it can be stated that increasing the number of sensors and yields in a improvement of the system performance. In fact, the resolution and accuracy of the estimation increases with the number of sensors and array aperture. Furthermore, the larger the array radius the better the single element antenna performance. Moreover, the bigger the array aperture the smaller the effect of the mutual coupling and the errors in the sensor characteristics, and the bigger the number of sensors the smaller the probability of ambiguity.

Since the objective of the design is generally to fulfill some specifications with the minimum cost (in this case, number of antennas are cost functions, in terms of space and prize), one possible design procedure consist on increasing these two parameters until fulfill some goals in terms of the three features. Therefore, the design process consists on start with a determine structure, and increase it cost functions (array radius and number of antennas) until fulfill some requirements.

Additional constraints can be introduced in order to reduce the number of possible structures, reducing the computational cost of the array design:

- In general, there are size contraints for the system. Therefore, a maximum array radius can be fixed. In this thesis the maximum array radius is set at 45cm for the first subarray, and 13cm for the second subarray.
- The rank-1 ambiguities of a UCA can be avoided if the number of antennas M, satisfy $M = 5\, or\, M \geq 7$ [24], so the search for the optimal number of sensors could start: $5, 7, 8...$
- A small array radius with an elevated number of antenna leads to high mutual coupling. Therefore, the maximum number of antennas for a given radius could be deduced from the full-wave analysis of the whole array.
- The array aperture increases the probability of ambiguity. Therefore, structures with unnecessary large array apertures must be avoided.

Following with the last point, an UCA is free of rank-2 ambiguities if the array aperture is smaller or equal than $\lambda/2$ [25]. Although this constraint is useful in single-band arrays, it is very difficult to satisfy in wideband systems, where the difference of array aperture in terms of wavelengths between the lowest and highest frequencies is large. This situation is well described in the table 5.2

Frequency (MHz)	$\lambda/2$ (cm)	Number of elements	Max Radius (cm)
300	50.0	5	39.8
400	37.5	5	29.8
500	30.0	5	23.9
600	25.0	5	19.9
700	21.4	5	17.1
800	18.8	5	14.9
900	16.7	5	13.3
1000	15.0	5	11.9
1100	13.6	5	10.9
1200	12.5	5	9.9

Table 5.2: Maximum array aperture and radius for a 5 element UCA free of rank-2 ambiguities.

5.2 Minimum detectable separation between signals

The minimum detectable separation between signals is the second feature that is studied. In order to study the effect of the array parameters in this feature independently, the number of signals is set at 2, and the SNR is is set at 20dB.

As anticipated, the design procedure follows a progressive scheme. Therefore, the analysis starts with a five-element UCA, the minimum number of antennas to avoid rank-1 ambiguities, and the array radius is progressively increased. The figures 5.2, 5.3 and 5.4 shows the probability of detection and the MSE as function of frequency for the array radius 15, 30 and 45cm.

The first conclusion obtained looking at these pictures is that the minimum separation between signals is reduced increasing the array radius. This is a completely logical result, because increasing the array radius the array aperture is also increased, and thus the resolution of the estimation. Moreover, the single element antenna performance is also better for larger radius. Consistently, the most limiting frequencies are the lowest ones, where the array aperture in terms of wavelength is the smallest.

Although the array aperture is operating at frequencies over the rank-2 ambiguity limit, it must be remarked that there is no sign of degradation produced by the ambiguities. It must be noticed that the limit introduced in [24] lies under the assumption of omnidirectional antennas, and the systems that include directional antennas should be more robust to ambiguities. However, it does not mean that there are no ambiguity effects. It can only be stated that the number of ambiguities in the steering vectors separated by less than 20º is small enough to do not affect to the mean system performance. In any case, the UCA free of rank-2 ambiguities, has an impractical radius.

It must also be remarked the excellent performance of the DOA estimation at the highest frequencies of the band, even over 1GHz, due to the high array apertures employed. However, the actual performance could be not so good if the mutual coupling is taken into account. At these frequencies the radiation is mainly directed toward the antenna edges, and the mutual coupling is maximized.

The figures 5.5 and 5.6 show the probability of detection and the MSE as function of frequency for the array radius 30 and 45cm. Comparing the performance of the DOA estimation of the array between the 5-element and 7-element UCA, it is concluded that there are no significant differences. Thus a configuration of 5-elements should be chosen, since cost and coupling effects are smaller.

In conclusion, the minimum detectable separation between signals is mainly influenced by the array radius, so the radius could be chosen to fulfill some requirements of this feature. The minimum detectable separation is also a strong function of frequency, where the lower frequencies of the band set the lower bound of this feature for the overall system.

The results shown that the minimum detectable separation is 10º with the maximum radius, independently of the number of antennas. It is a limited resolution, but it must be reminded that the resolution is conditioned by the beamwidth, and the radiation pattern at 250MHz is almost omnidirectional.

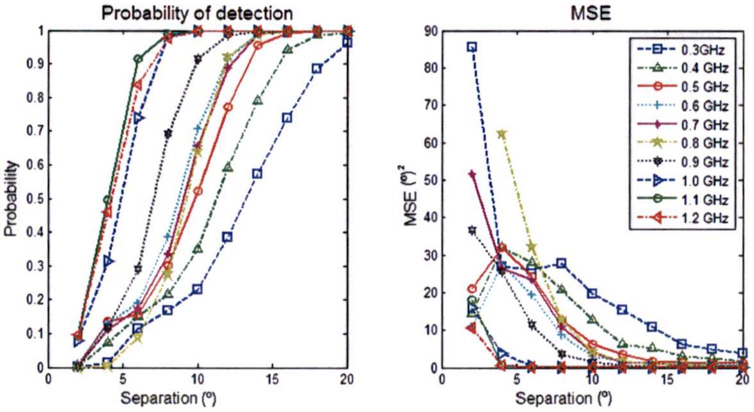

Figure 5.2: Probability of detection and MSE for a five-element UCA with radius 15cm. The incoming signals are separated by 20º and have a SNR of 20dB.

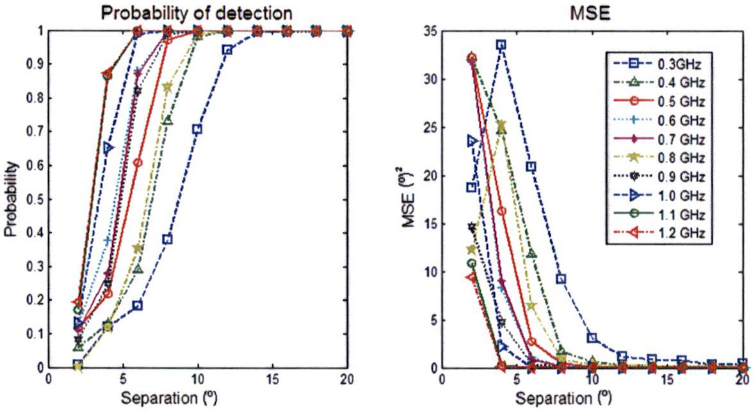

Figure 5.3: Probability of detection and MSE for a five-element UCA with radius 30cm. The incoming signals are separated by 20º and have a SNR of 20dB.

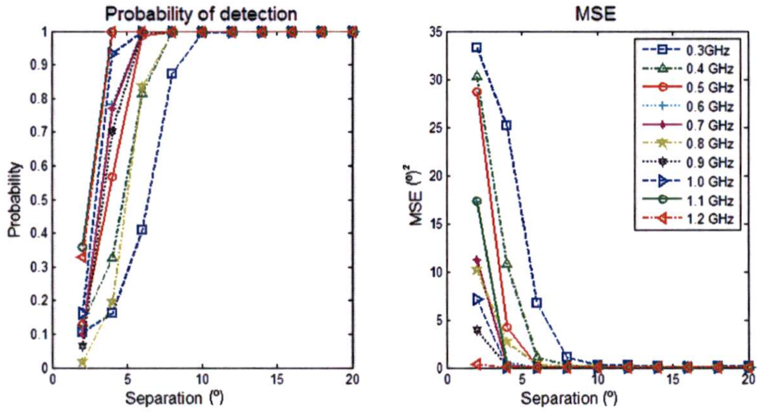

Figure 5.4: Probability of detection and MSE for a five-element UCA with radius 45cm. The incoming signals are separated by 20º and have a SNR of 20dB.

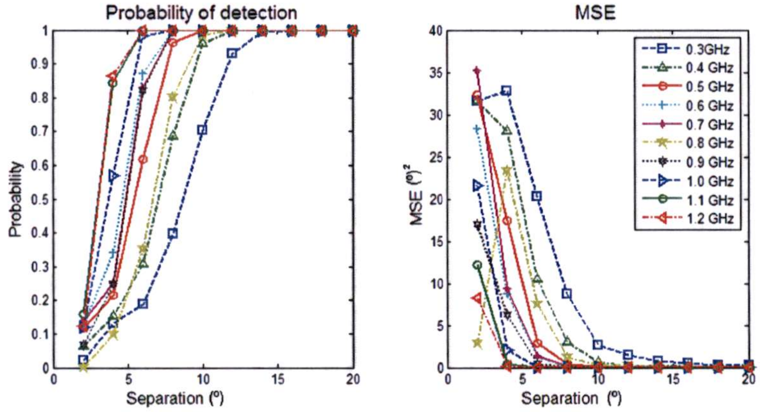

Figure 5.5: Probability of detection and MSE for a seven-element UCA of radius 30cm. The incoming signals are separated by 20º and have a SNR of 20dB.

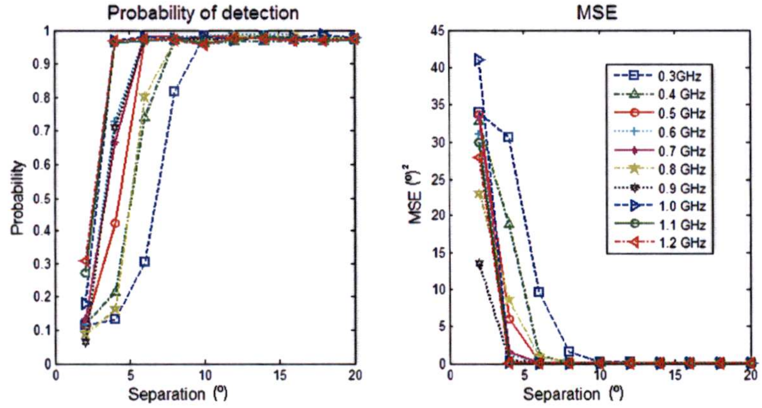

Figure 5.6: Probability of detection and MSE for a seven-element UCA with radius 45cm. The incoming signals are separated by 20º and have a SNR of 20dB.

5.3 Maximum detectable number of signals

The last feature studied is the maximum number of signals detectable. As anticipated, these three features are investigated independently, so the maximum number of signals is studied under enough good conditions, a SNR of 20dB and a separation between signals of 20 degrees.

Theoretically, if M is the number of sensors, and N is the number of signals, the MUSIC algorithm is able to detect any number of signals if M > N. That is to say, the MUSIC algorithm is able to detect M-1 signals. Even more, modifying the MUSIC algorithm it is possible to detect more signals that sensors, for example with the Cyclic MUSIC algorithm [?]. Furthermore, other algorithms which are not evolutions of MUSIC are also able to detect more sources than sensors [45].

However, a larger number of incoming signals affects the performance of the system. There are mainly two sources of degradation. Firstly, it is well-known that the projection of the signals in the noise space is not perfect, and the peaks in the MUSIC spectrum corresponding to incoming signals with the same power can have different values. Therefore, if the value of the peak corresponding with a signal between two other signals is smaller than these other ones, this peak could be lost. This effect is especially important at low frequencies, where the peaks are not so sharp.

Secondly, a higher number of signals also increase the probability of ambiguity, because higher rank ambiguities are possible, and the number of combinations for lowers rank ambiguities is also larger.

The picture shows an example of these two sources of errors. The array is an UCA with seven elements and radius 45cm, the number of incoming signals is 6, and its DOAs are 50, 70, 90, 110,130 and 150º. In the first case, the frequency of operation is 300MHz. It is shown that due to the influence of the wide peaks and the lack of resolution, the 90 and 110º merge into a single peak at 100º and the detection fails. In the second case, the frequency of operation is 1000MHz- It is possible to appreciate that a strong fake peak appears at 18º due to the ambiguities. Therefore, the 70º peak is ignored, and the detection also fails.

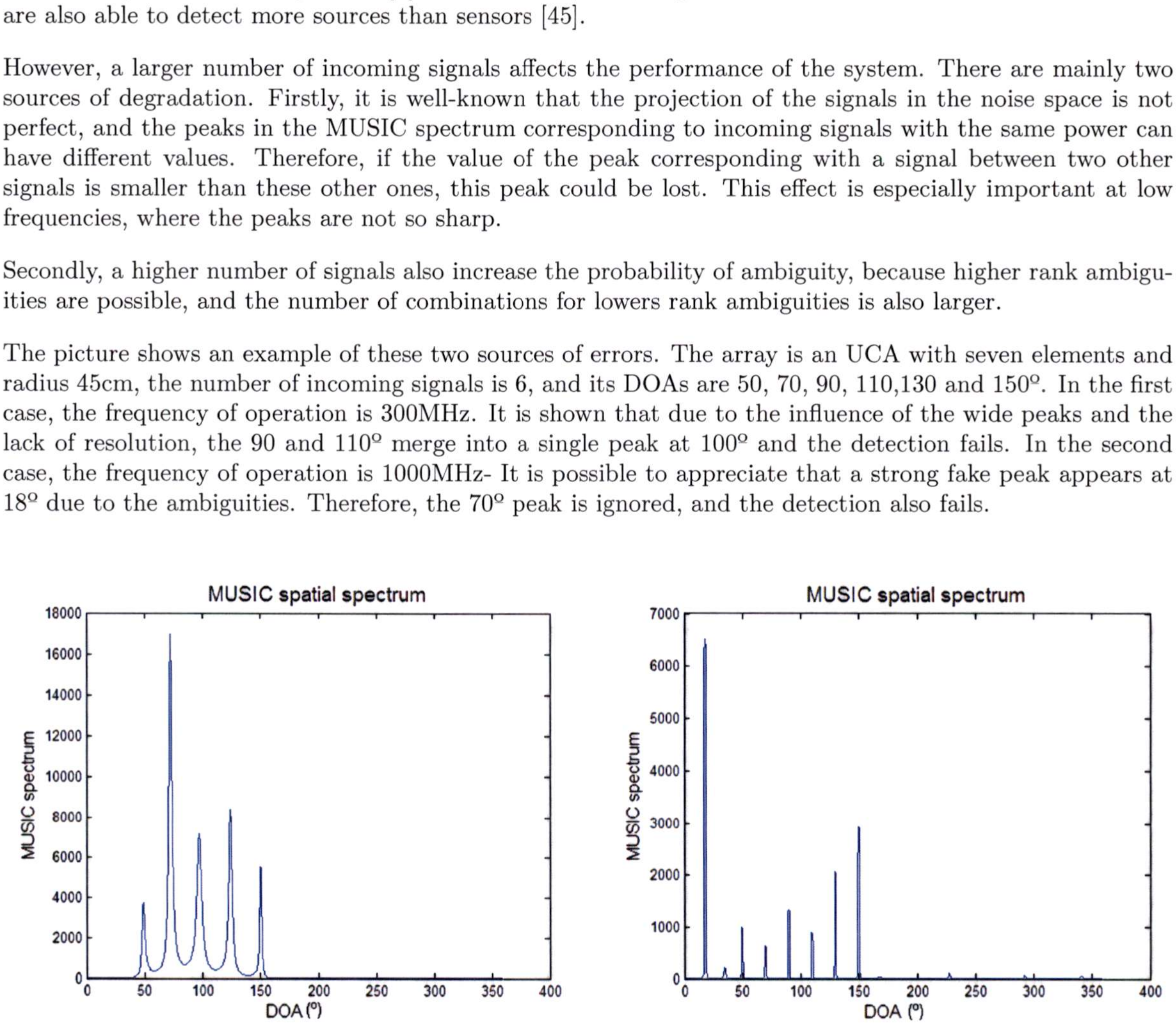

Figure 5.7: MUSIC spectrum of 6 incoming signals at 300 and 1000MHz, with DOAs 50, 70, 90, 110,130 and 150. The array geometry is an UCA with 7 antennas and array radius 45cm.

The pictures 5.8 and 5.9 show the DOA estimation performance for an array of radius 45cm and 5 and 7 elements. It is possible to observe the two sources of degradation, at the lowest and at the highest frequencies of the band. It is clear that in order to increase the maximum number of detectable signals is necessary to increase the number of array elements.

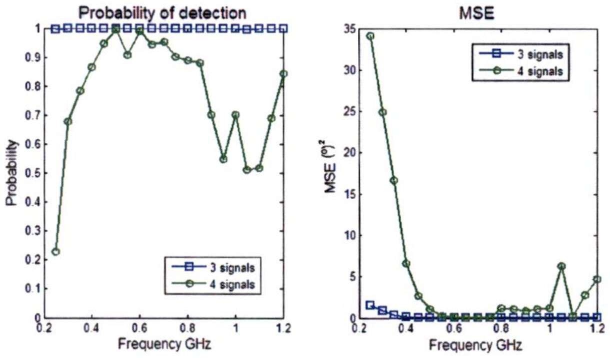

Figure 5.8: Probability of detection and MSE for 3 and 4 incoming signals. The array geometry is an UCA with 5 antennas and radius 45cm.

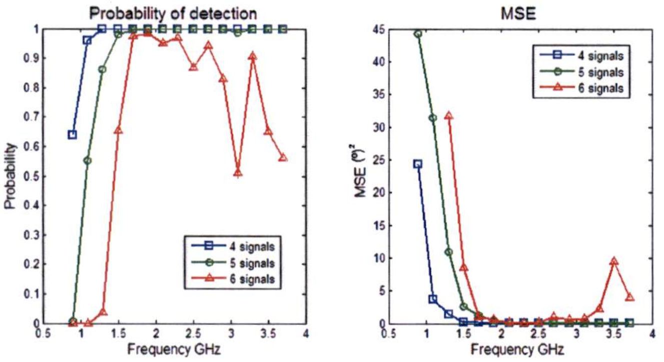

Figure 5.9: Probability of detection and MSE for 4,5 and 6 incoming signals. The array geometry is an UCA with 7 antennas and radius 45cm.

These effects can also be appreciated varying the radius of the array. The picture shows the DOA estimation performance of a UCA with 5 elements a radius of 45cm. The number of incoming signals is 4. The performance at the lowest frequencies is degraded reducing the radius, but the performance is enhanced at higher frequencies, due to the reduction of the probability of ambiguity.

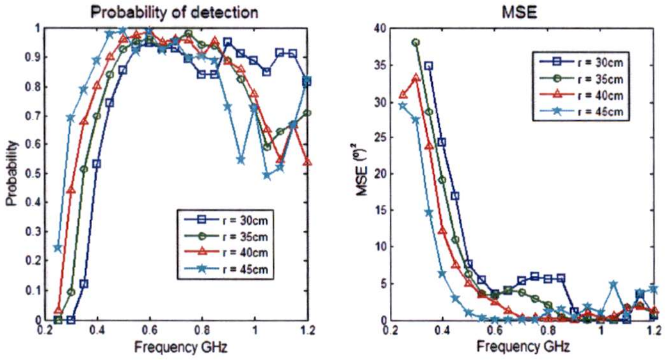

Figure 5.10: Probability of detection and MSE for 4 incoming signals. The array geometry is an UCA with 5 antennas and radius 30, 37.5, 45 and 55cm.

5.4 Minimum SNR of operation

The first feature of the system that is presented is the minimum SNR of operation. In order to study the effect of the array parameters in this feature independently, the separation between the two incoming signals is set at 20º. This separation can be considered a minimum that must be solved under any circumstance.

In general, there are two main contributions to noise of the system. The first one is the noise received in the antenna, which is basically defined by the environment, and the other one has an electronic origin, and is due to the noise generated by the receptor. Thus, the complete SNR follows the expression:

$SNR = \frac{G \cdot S}{G \cdot N_{env} + N_{elec}}$

Where S is the incident signal power, N_{env} is environmental noise and N_{elec} is the noise contribution generated in the receptor. The main difference between both noise contributions is that N_{env} is affected by the gain of the antenna, and N_{elec} is not.

Therefore, there are two possible scenarios, one when the noise contribution of the environment is dominant and the other one when the noise contribution of the electronics is dominant. In the first one, the influence of the antenna gain I the system performance can be neglected, and the array geometry is the most influent factor. In the second one, the array geometry has influence in the system performance, but the antenna gain will also be determinant.

The second approach is analyzed in figure 5.11. To this end, the figure shows the Probability of Detection (PoD) and Mean Square Error (MSE) vs frequency for different SNR. In this approach the SNR is defined as S/N_{elec}. The scenario in defined by two incoming signals of random DOA and separated by 20º, the array is a five-element UCA of radius 45cm.

These pictures shows that there are two sources of degradation for the probability of detection. The first one at the lowest frequencies of the one, caused by the small array aperture, that is to say, the geometry of the array. The second one is placed near 1GHz and it is caused by the low gain of the antenna at that frequency. This results is an excellent example of how the antenna influences the overall system performance.

On the other hand, the first approach is analyzed in figure 5.12. Here, the SNR is defined as S/N_{env}. In this picture, there is no degradation of the PoD due to the low antenna gainat 1GHz. However, the performance at the lowest frequencies of the band is sligthly worse for the same reason.

Moreover, the degradation due to the high level of noise is mainly concentrated in the probability of detection. That means that the MUSIC algorithm is having problems to identify the noise and signal subspaces, but if the noise subspace is correctly described, the detection will be accurate.

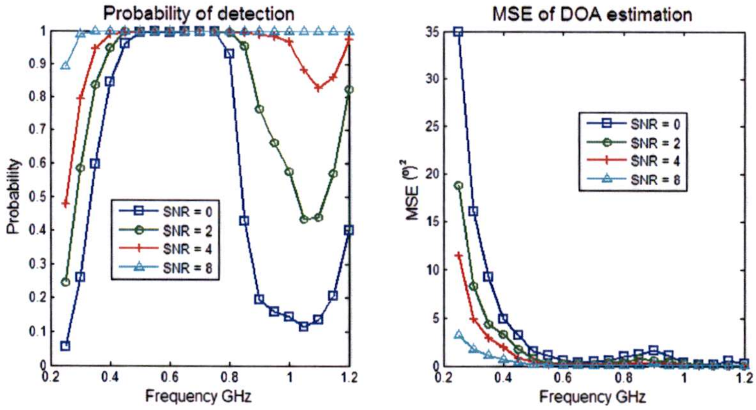

Figure 5.11: Probability of detection and MSE for two incoming signals separated by 20º and with different SNRs. The array geometry is UCA with 5 elements and 45cm of array radius. The electronic noise is considered dominant.

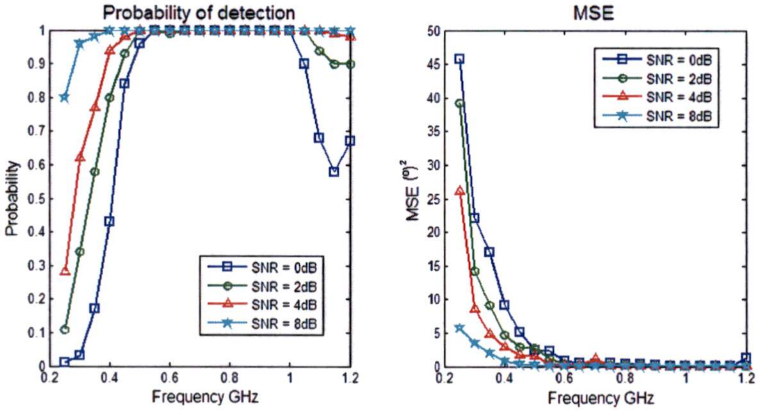

Figure 5.12: Probability of detection and MSE for two incoming signals separated by 20º and with different SNRs. The array geometry is UCA with 5 elements and 45cm of array radius. The environmental noise is considered dominant.

The figure 5.13 shows the probability of detection and MSE for two incoming signals separated by 20 degrees and with a SNR of 6dB. Different lines are plot for array radiuses from 25 to 45cm. As it is shown, reducing the curvature radius has a negative impact in the DOA estimation performance, especially at low frequencies, and thus limiting the minimum SNR of operation.

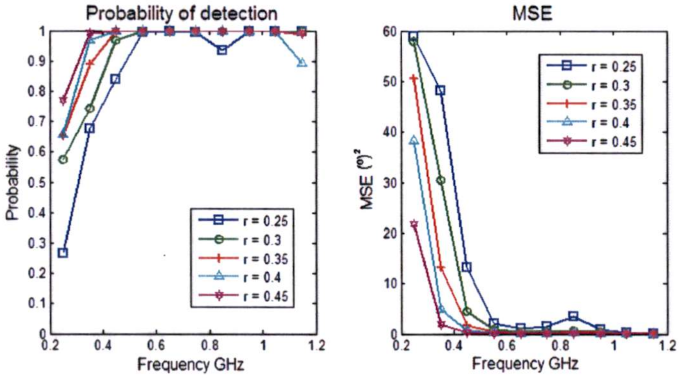

Figure 5.13: Probability of detection and MSE for different array radius and SNR 6dB. The electronic noise is considered dominant.

5.5 Ultra-Wideband DOA estimation performance

The previous sections have presented the algorithm-oriented array design. To this end, these sections have introduced design guidelines aimed to the enhacement of the DOA estimation performance under the implementation of the MUSIC algorithm. This narrow-band algorithm is one of the most popular estimation algorithms, and thus makes the design comparable with other systems. Furthermore, this algorithm is compatible with some of the most popular algorithms for UWB DOA estimation, particularly those based on CSM, as it is explained is section 4.3. Therefore, the introduced design is also suitable for UWB DOA estimation.

This section introduces the performance of the designed array with UWB signals. Particularly, a UCA with 5 elements and an array radius of 45cm is employed. Two far-field wideband sources with the same power are located at random arrivals with a separation of 20 degrees. The sources spectra is shown in figure 5.14, the PSD has been properly chosen to fit the subarray range. The center frequency of the spectrum is selected as the focusing frequency. The output of each sensor is decomposed into 100 snapshots (K = 100) of 256 samples each. An FFT algorithm is used in each block to sample the spectrum of signals and 34 frequency bins are used in the DOA estimation.

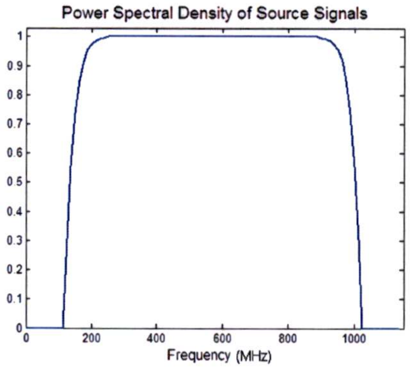

Figure 5.14: Normalized Power Spectral Density (PSD) of source signals.

The probability of detection and mean square error of the DOA estimation for different SNRs can be seen in figure. The proposed design presents a competitive performance in terms of both statistics.

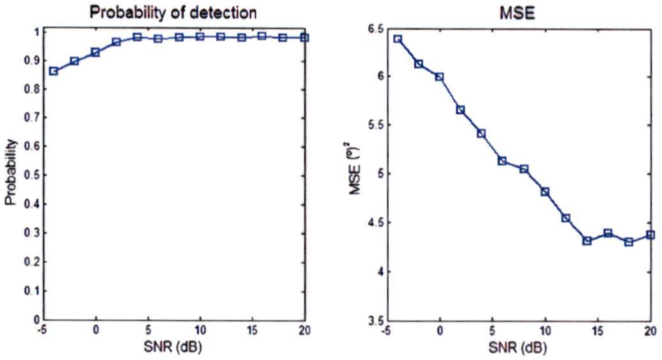

Figure 5.15: PoD and MSE for two incoming signals separated by 20º and with SNRs from -4 to 20.

Chapter 6

Calibration techniques

6.1 Introduction

The MUSIC algorithm, as the other eigenstructure methods, needs a complete knowledge of the steering matrix to perform a correct DOA estimation. Hence, a lack of correspondence between the actual steering matrix and the steering matrix employed in the data model will virtually destroy the DOA estimation performance.

Unfortunately, there are many factors that affect the antenna array performance. Thus, the differences between the actual and the estimated steering matrix are evident. Hence, this problem must be treated, and it is necessary to employ calibration techniques to deal with all these sources of error.

6.2 Sources of error

There are two principal sources of error, the mutual coupling and the error in the sensor characteristics:

Mutual coupling

The mutual coupling between the array elements is a very strong source of error that includes the near field interferences between the array elements and the scattering of incoming signals. It must be notice that not only the antennas cause interference between them, but the waveguides that feed the antenna and the supporting structure can also affect the system performance.

In this case, the antennas are fed with long but very thin lines orthogonal to the antenna plane. Therefore, the influence of the feeding lines will be limited, especially with vertical polarization, because the scattered fields from this waveguides will have horizontal polarization.

The supporting structure is mainly formed by a metallic mast. Unfortunately, the mast must be big enough to guarantee mechanical stability to the system, and the scattered fields from it have vertical polarization. Therefore, the influence of the mast in the structure is important and it would be recommendable to study if it is possible to cover the mast with an absorber layer without affect the antennas performance.

In the data model, the coupling effects are usually taken into account including a coupling matrix, C, with size $M \times M$. In some cases the coupling matrix is extended and includes the effect of the supporting structure. In this model, the effect of the mutual coupling is a change from the original steering matrix A to a new steering matrix $C \cdot A$.

The previous data model: $X = A \cdot F + W$

Data mode with coupling: $X = C \cdot A \cdot F + C \cdot W$

Although the mutual coupling changes the noise properties, in general this effect is neglected. Due to the mutual coupling the noise in the antenna ports is not uncorrelated, and the noise covariance matrix becomes non-diagonal. However, in general the estimated noise covariance is non-diagonal, and noise subspace is estimated using a threshold between the eigenvalues of the signal and noise subspace. Therefore, the effect of the noise coupling is not important under good SNR.

Moreover, in general the calibration matrix is invertible, and the effect of the mutual coupling in the noise and signal subspaces can be removed multiplying by C^{-1}. The C matrix can be estimated using calibration techniques under high SNR or the full-wave analysis of the whole array structure.

The full-wave analysis of the whole array structure gives enough information to characterize the mutual coupling effects, taking into account not only the scattered field, but also the near field interferences. Moreover, the full-wave analysis is itself an excellent calibration technique, because if the coupling effects are well-known, the impact over the DOA estimation performance is negligible.

The coupling matrix can be estimated from the scattering parameters of the array. The figure 6.1 shows the S_{11}, S_{12}, $and\, S_{13}$ parameters of a five-element UCA with radius 45cm, the other scattering parameters are omitted by reciprocity. The single antenna element in the antenna introduced in section3.7, with a flair's thickness of 1.5mm.

As in many other systems based on dipoles, the mutual coupling between the antenna elements is high, due to the omnidirectional nature of the antennas. Furthermore, the mutual coupling changes the radiation pattern of the single antenna element, as it is shown in the figure 6.1, which presents the radiation pattern in the H-plane at 250MHz. In spite of this, the antenna radiation patterns can be measured, compensating this effect.

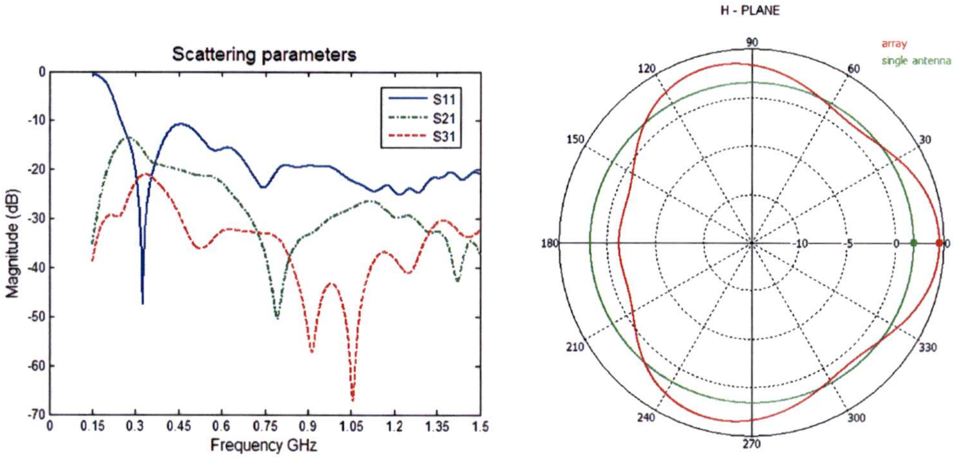

Figure 6.1: Array scattering parameters. Effect of mutual coupling in the radiation pattern, H plane at 250MHz.

It also important to study the mutual coupling with supporting structure. Unfortunately, it is not always possible to carry out a full-wave analysis of the whole array structure, including the mast and arms. Therefore, a simplified will be employed here, that takes into account the coupling with mast structure analyzing the scattered waves by means of the Friis equation. Hence, C_{mast}, the coupling factor between the antennas and the mast, will follow the equation:

$$C_{mast} = \frac{g_{mast} \cdot g_{ant} \cdot \lambda}{4\pi R} \cdot e^{jkR} \left(1 + \sqrt{S_{11}} \frac{g_{mast} \cdot g_{ant} \cdot \lambda}{4\pi R} \cdot e^{jkR}\right)$$

Where the coupling coefficient is form by two terms. The first one is the scattered wave re-radiated form the mast to the antenna, and the second one is the wave re-radiated from the antenna to the mast, and again, from the mast to the antenna. In this equation, the mast has been characterized as a antenna with a certain gain. The figure 6.2 shows the coupling coefficient vs frequency for different gain values. Logically, the front to back ratio has a great influence in the coupling factor.

Due to the strong influence of the coupling effects in the DOA estimation there are different calibration techniques that try to alleviate its effects, most of them consist on an estimation of the coupling matrix C. The figure 6.3 show the effect of the mutual coupling in the MUSIC spectrum of the figure 4.1. As can be appreciated, the determination of the number of signals is successful, since the noise and signal eigenvalues have been identified successfully. However, it is not possible to calculate the MUSIC spectrum correctly, because the steering matrix employed is not correct.

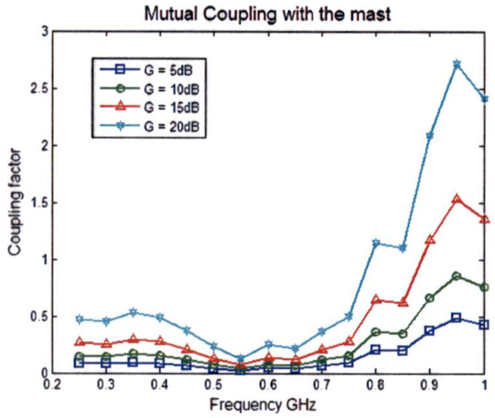

Figure 6.2: C_{mast} vs frequency for different antenna gain.

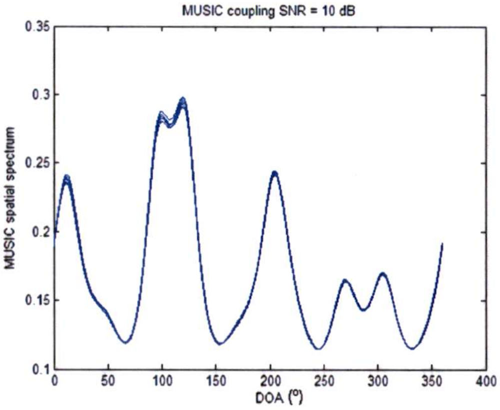

Figure 6.3: MUSIC spatial spectrum with coupling. Two signals at 100 and 120º. Superposition of 10 estimations

Error in the sensor characteristics

This source of error consists in the difference between the actual and nominal characteristics of the sensor. Including deviations in the position, gain and phase. The phase errors have the biggest influence, due to the big part of information stored in the phase of the steering vectors.

The influence of this sort of errors is very dependent on the magnitude of the errors. Small errors yield in a bigger MSE but do not affect to the probability of detection. However, large errors lead to a totally deviation in the DOA estimation. The figure 6.4 shows the previous MUSIC spectrum in the presence of errors. The errors follow a normal distribution, with standard deviation of the 1% and 5%.

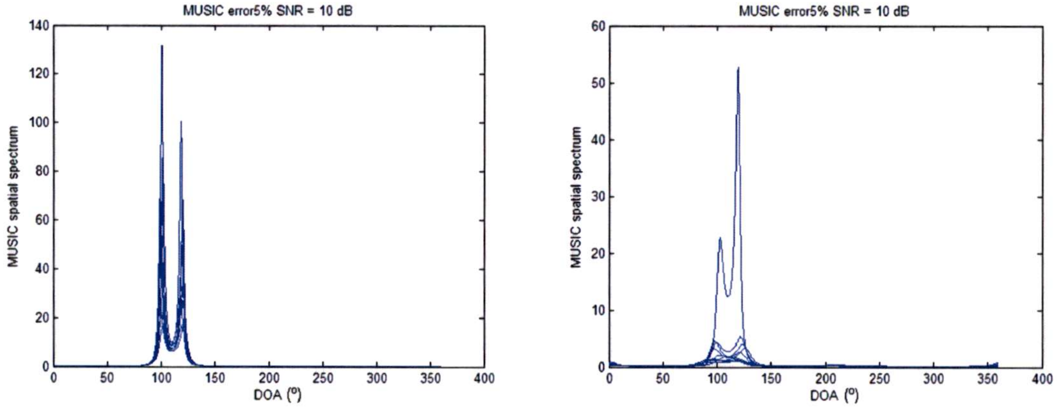

Figure 6.4: MUSIC spatial spectrum with errors in the position, phase and gain of the sensors of 1% and 5%. Two signals at 100 and 120°. Superposition of 10 estimations.

The figure 6.5 shows the impact of errors in the antenna characteristics in the DOA estimation performance. As anticipated, small errors have no influence in the performance, but strong errors virtually destroy it. In spite of this, it is highly improbable to find strong errors in a well-manufactured array.

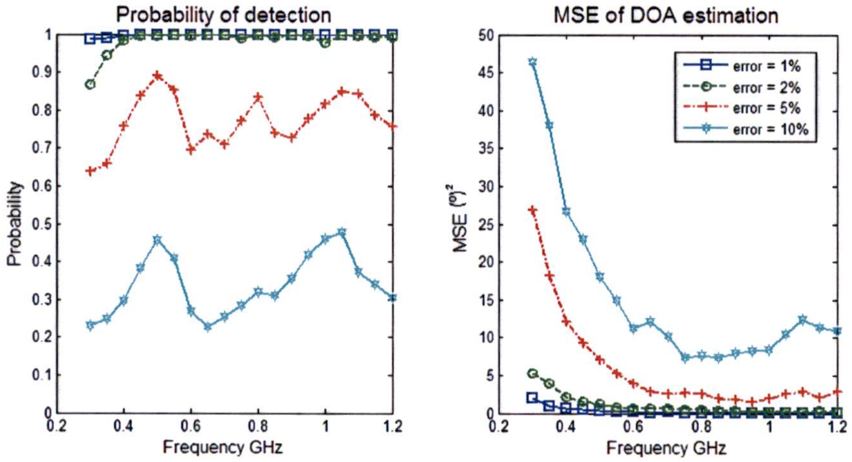

Figure 6.5: Probability of detection and MSE for error of the sensor characteristics 1%, 2%, 5% and 10%.

6.3 Calibration techniques

The previous section has described the main source of error in Direction Finding systems. Due to the impact on the system performance of these source of error, the development of calibration techniques has attracted and is attracting a great deal of research interest. Therefore, there are many different calibration techniques. This section gives to the reader an overview of the existing calibration techniques and includes a comparative studio. A more complete description of the implemented calibration techniques can be found in the appendix.

As a first approach, the calibration techniques can be subdivided in two groups, local calibration techniques and global calibration techniques. The global calibration techniques are based in the assumption that the mutual coupling matrix (MCM) is independent of DOA of arrival. On the other hand, the local calibration techniques take into account the dependence of the MCM on the DOA. The mutual coupling and errors in the phase and gain of the antennas are completely described by a global calibration matrix $C \neq C(\phi, \theta)$. However, the error in the sensor positions and the differences in the antenna radiation patterns are scan dependent errors, and require local calibration $C = C(\phi, \theta)$. In spite of this, most arrays are manufactured with high mechanical accuracy, and the radiations patterns can be measured in anechoic chambers, so the scan dependent errors are small and are usually neglected. Nevertheless, a good local calibration technique can be found in [53].

Regarding with the global calibration techniques, these techniques may be classified in two families: deterministic methods and blind methods.

6.3.1 Deterministic calibration techniques

The deterministic methods are off-line calibration techniques. The errors are removed with matrix compensation, provided that the mutual coupling matrix has been calculated, measured or estimated ahead in time. These techniques are the most accurate and reliable. However, these methods have some disadvantages such as complex numerical calculation, accurate pattern measurement and additional calibration procedure required. However, the main drawback is that these methods can not be carried out during the system operation, so the effect of the environment and is neglected.

The first calibration techniques were based on the minimization of a function cost. Pierre a Kaveh [46], 1991, proposed to minimize the sum of squared euclidean distances between $M^{-1}a_{mk}$ and a_k. Where M is the estimated mutual coupling matrix a_{mk} is a measured steering vector, and a_k the theoretic steering vector in the same direction.

$$\underset{M}{\arg\min} \ \left\|M^{-1}A_m - A\right\|_F^2 = \textstyle\sum_{k=1}^{K} \left\|M^{-1}a_{mj} - a_j\right\|^2$$

See [47] proposed in 1993 and later in 1996 an iterative minimization procedure, taking into account the error in the sensor characteristics, gain, phase and position.

$$\hat{M}, \hat{\psi} = \underset{M,\psi}{\arg\min} \ \|M \cdot A(\psi) - A_m\|_F^2$$

Where ψ is the estimated position of the antennas.

In 1999, Pensel [48] proposed to use an orthogonality criterion. For each calibration measurement a_{mj}, he found a vector c_j which is orthogonal to a_{mj}. The calibration matrix M is now determined such that $Q \cdot a_j$ is as orthogonal to c_j as possible:

$$\underset{Q}{\min} \ \textstyle\sum_{j=1}^{K} \left|c_j^* M \cdot a_j\right|^2 \quad s.t. \ \|M\|_F^2 = 1$$

In 2003, Kortke [49] proposed a collinearity criterion. The objective is to determine M in such a way that $M \cdot a_j$ is as parallel to a_{mj} as possible:

$$\underset{M}{arg\,min} \sum_{j=1}^{J} \left(\|a_{mj}\|^2 \|M \cdot a_j\|^2 - |a_{mj}^* \cdot M \cdot a_j|^2 \right) \quad s.t. \ \|M\|_F^2 = 1$$

In general, all these calibration techniques model the errors in the gain/phase as a global calibration matrix, and solve the minimization problem using the pseudoinverse. This technique is summarized in [50]. Hence, the difference are introduced to deal with errors in the sensor positions [47], errors in the measurement process [49]...

$A_m = M \cdot A \implies M = A_m \cdot A^H (A \cdot A^H)$

There is another important family of calibration techniques. These techniques take advantage of the previous knowledge about of the array structure, creating an analytical model to describe the mutual coupling. The method introduced in [51] (2000), has been a popular technique. However, it only considers omnidirectional antennas. A more complete approach was introduced by Ferreol in 2007, that includes, the mutual coupling between the mast and supporting structure [52].

As introduced, there are techniques that solve the problem of the mutual coupling between the antenna elements and the errors in the sensor characteristics, and there is also a technique that includes the mutual coupling between the array elements and supporting structure. Therefore, in this thesis a novel technique is introduced that takes into account the errors in the antenna characteristics and mutual coupling between the array elements and supporting structure. This technique is based on [52], extending the model with an analytical model for the errors in the antenna characteristics.

Steering vectors for a Uniform Circular Array:

$a(\phi,\theta) = [a_1(\phi,\theta), \ldots, a_j(\phi,\theta), \ldots, a_M(\phi,\theta)]^T$

$a_j(\phi,\theta) = g(\phi - (j-1)\frac{2\pi}{M}, \theta) \cdot e^{jkRsin(\theta)cos(\phi-(j-1)\frac{2\pi}{M})} = g(\phi - (j-1)\frac{2\pi}{M}, \theta) \cdot e^{jkRsin(\theta)\cdot(x\cdot cos(\phi)+y\cdot sin(\phi))}$

Analytical model for the errors in the antenna characteristics:

- Error in the antenna gain/phase:

$$a_j^{true}(\phi,\theta) = \Delta g_j \cdot e^{\Delta\varphi_j} \cdot g(\phi - (j-1)\frac{2\pi}{M}, \theta) \cdot e^{jkRsin(\theta)cos(\theta-(j-1)\frac{2\pi}{M})} = \Delta g_j^1 \cdot e^{\Delta\varphi_j^1} \cdot a_j(\phi,\theta)$$

- Error in the antenna position:

$$a_j^{true}(\phi,\theta) = g(\phi - (j-1)\frac{2\pi}{M}, \theta) \cdot e^{jkRsin(\theta)\cdot[(x+\Delta x_j)\cdot cos(\phi)+(y+\Delta y_j)\cdot sin(\phi)]} = e^{jkRsin(\theta)\cdot[\Delta x_j \cdot cos(\phi)+\Delta y_j \cdot sin(\phi)]} \cdot a_j(\phi,\theta)$$

- Error in the antenna orientation:

$$a_j^{true}(\phi,\theta) = g(\phi + \Delta\phi_j - (j-1)\frac{2\pi}{M}, \theta + \Delta\theta_j) \cdot e^{jkRsin(\theta)cos(\theta-(j-1)\frac{2\pi}{M})} = \Delta g_j^2(\phi,\theta) \cdot a_j(\phi,\theta)$$

- Error in the radiation pattern:

$$a_j^{true}(\phi,\theta) = \Delta g_j^3(\phi,\theta) \cdot a_j(\phi,\theta)$$

From the previous description of the antenna errors it is clear the the errors in the antenna gain and phase are independent of the DOA, but the errors in the antenna position, orientation and radiation pattern are DOA dependent. Therefore, the former errors can be compensated with a global calibration matrix, $C \neq C(\phi,\theta)$, but the latter errors require a scan dependent calibration matrix, that is to say $C = C(\phi,\theta)$.

In general the radiation patterns of the antenna can be measured, so the errors in the antenna orientation and radiation pattern can be neglected. If the array is built accurately there should not be large errors in the sensor positions. Therefore, global calibration techniques are usually employed.

In this case, it is shown that all the errors in the sensor characteristics can be modeled as complex constant multiplying each component of the steering vector. The constant will be the same for all the components of the same antenna and under this assumption is angle independent.

According to this model, the actual steering matrix is modified. If N pilot signals are collected, the measured steering matrix will follow:

$$\tilde{A} = E \odot A$$

$$E = \begin{bmatrix} e_1 & \dots & e_1 \\ \vdots & \ddots & \vdots \\ e_M & \dots & e_M \end{bmatrix}$$

Where E is a row-matrix whose elements are the complex constants that model the error in the sensor characteristics. If the mutual coupling is included:

$$\tilde{A} = Z_o \cdot (E \odot A)$$

Where:

$$\tilde{a}_{mn} = \sum_{i=1}^{M} z_{ni} \cdot (e_{in} \cdot a_{in}) = \sum_{i=1}^{M} z_{ni} \cdot (e_n \cdot a_{in}) = \sum_{i=1}^{M} (z_{ni} \cdot e_n) \cdot a_{in}$$

Therefore, the model can be reformulated as:

$$\tilde{A} = Z_o \cdot (E \odot A) = (Z_o \odot E_{red}^T) \cdot A$$

$$E_{red}^T = \begin{bmatrix} e_1 & \dots & e_M \\ \vdots & \ddots & \vdots \\ e_1 & \dots & e_M \end{bmatrix}$$

Where E_{red}^T is an MxM matrix, equal to the transpose of the E matrix reduced to five columns. With this model, the mutual coupling and the error in the sensor characteristics are gathered together in a global coupling matrix with known structure. The figure 6.6 shows the mutual coupling for a five-element UCA, under this model, the matrix becomes:

$$Z_o = \begin{bmatrix} 1 & \alpha & \beta & \beta & \alpha \\ \alpha & 1 & \alpha & \beta & \beta \\ \beta & \alpha & 1 & \alpha & \beta \\ \beta & \beta & \alpha & 1 & \alpha \\ \alpha & \beta & \beta & \alpha & 1 \end{bmatrix} \odot \begin{bmatrix} e_1 & e_2 & e_3 & e_4 & e_5 \\ e_1 & e_2 & e_3 & e_4 & e_5 \\ e_1 & e_2 & e_3 & e_4 & e_5 \\ e_1 & e_2 & e_3 & e_4 & e_5 \\ e_1 & e_2 & e_3 & e_4 & e_5 \end{bmatrix} = \begin{bmatrix} e_1 & \alpha e_2 & \beta e_3 & \beta e_4 & \alpha e_5 \\ \alpha e_1 & e_2 & \alpha e_3 & \beta e_4 & \beta e_5 \\ \beta e_1 & \alpha e_2 & e_3 & \alpha e_4 & \beta e_5 \\ \beta e_1 & \beta e_2 & \alpha e_3 & e_4 & \alpha e_5 \\ \alpha e_1 & \beta e_2 & \beta e_3 & \alpha e_4 & e_5 \end{bmatrix}$$

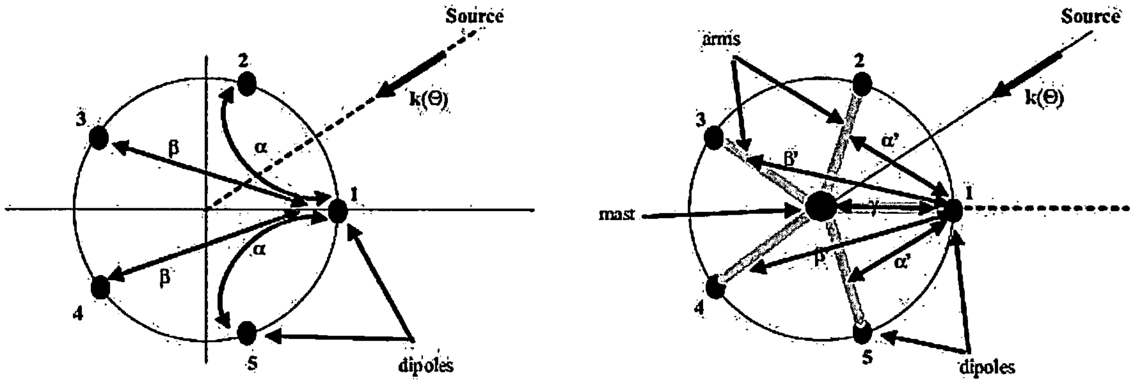

Figure 6.6: Mutual coupling in the case of a five element antenna. Coupling between the array elements and supporting structure.

Additionally, this model can be extended to take into account the supporting structure:

$\tilde{a}(\theta) = Z \cdot b(\theta)$ *where* $b = \begin{bmatrix} a(\theta) \\ a_b(\theta) \end{bmatrix}$ *and* $Z = [Z_0 \, Z_b]$

$$Z_b = \begin{bmatrix} \alpha_0 & \alpha' & \beta' & \beta' & \alpha' & \gamma \\ \alpha' & \alpha_0 & \alpha' & \beta' & \beta' & \gamma \\ \beta' & \alpha' & \alpha_0 & \alpha' & \beta' & \gamma \\ \beta' & \beta' & \alpha' & \alpha_0 & \alpha' & \gamma \\ \alpha' & \beta' & \beta' & \alpha' & \alpha_0 & \gamma \end{bmatrix}$$

However, for a vertical polarization array with small feeding structures only the mast coupling is important, so $\alpha_0 = \alpha' = \beta' = \beta' = \alpha' = 0$. Moreover, the influence of the mast can also be affected by the errors in the antennas.

$$Z_b = \begin{bmatrix} e_1 \cdot \gamma \\ e_2 \cdot \gamma \\ e_3 \cdot \gamma \\ e_4 \cdot \gamma \\ e_5 \cdot \gamma \end{bmatrix}$$

As for the minimization problem, each row of the matrix Z can be rewritten as:

$$z_m^T = D_n \cdot c$$

Where

$$D_m = \begin{bmatrix} D_{0m} & 0 \\ 0 & D_{bm} \end{bmatrix} \quad and \quad c = \begin{bmatrix} c_0 \\ c_b \end{bmatrix}$$

$$e_1 \cdot \gamma c_0 = [e_1, \alpha \cdot e_1, \ldots, e_5, \alpha \cdot e_5, \beta \cdot e_5]^T \quad and \quad c_b = [e_1 \cdot \gamma, \ldots, e_5 \cdot \gamma]^T$$

And, for example:

$$D_{01} = \begin{bmatrix} 1 & 0 & 0 & 0 & 0 & 0 & 0 & 0 & 0 & 0 & 0 & 0 & 0 & 0 & 0 \\ 0 & 0 & 0 & 0 & 1 & 0 & 0 & 0 & 0 & 0 & 0 & 0 & 0 & 0 & 0 \\ 0 & 0 & 0 & 0 & 0 & 0 & 0 & 0 & 1 & 0 & 0 & 0 & 0 & 0 & 0 \\ 0 & 0 & 0 & 0 & 0 & 0 & 0 & 0 & 0 & 0 & 0 & 1 & 0 & 0 & 0 \\ 0 & 0 & 0 & 0 & 0 & 0 & 0 & 0 & 0 & 0 & 0 & 0 & 0 & 1 & 0 \end{bmatrix}, \quad D_{b1} = \begin{bmatrix} 1 & 0 & 0 & 0 & 0 \end{bmatrix}$$

At this point, a model for the mutual coupling of a UCA has been described. The next step is the evaluation of the model parameters, that is to say, the vector c. To this end, K pilot signals are employed. Thus, K, steering vectors, are measured: $a_e(\theta_i)$ with $1 \leq i \leq K$.

The relation between the measured vectors, $a_e(\theta)$, and the vectors estimated by the model, $\tilde{a}(\theta)$, is given by:

$$a_e(\theta) \approx \rho \cdot e^{j\varphi} \cdot \tilde{a}(\theta)$$

$$a_{em}(\theta) \approx \rho \cdot e^{j\varphi} \cdot z_m \cdot b(\theta)$$

Where ρ and φ are the amplitude and phase ambiguity respectively. Defining $c' = \rho \cdot e^{j\varphi} \cdot c$, the previous relation becomes:

$$a_{em}(\theta) \approx t_m^T \cdot c' \quad where \quad t_m^T = b(\theta)^T \cdot D_n$$

Since the expression of t_n^T is analytical, and $a_{em}(\theta)$ is provided by the calibration process, the problem of finding the coupling parameters, c', can be solve as a minimization problem:

$$\hat{c'} = \underset{c}{arg\,min} \left\{ \sum_{m=1}^{M} \sum_{i=1}^{K} \left| t_m^T(\theta_i) \cdot c - a_{em}(\theta_i) \right| \right\}$$

The solution to the previous equation is:

$$\hat{c'} = (Q^\dagger Q)^{-1} Q^\dagger q$$

$$Q = \begin{bmatrix} T(\theta_1) \\ \vdots \\ T(\theta_K) \end{bmatrix} \quad where \quad T(\theta) = \begin{bmatrix} t_1^T(\theta) \\ \vdots \\ t_N^T(\theta) \end{bmatrix}$$

$$q = \begin{bmatrix} a_e(\theta_1) \\ \vdots \\ a_e(\theta_K) \end{bmatrix}$$

This calibration technique has been tested with 2 incoming signals with SNR 10 dB separated by 20º. The array geometry is a 5-element UCA with radius 45cm. The error in the sensor characteristics follow a normal distribution with a std of 5% of its nominal values. The mutual coupling between the array elements has been modeled with the data obtained in the full-wave analysis, and the mast influence has been modeled as an antenna with gain 10dB.

The original and extended techniques are compared with the conventional calibration techniques in figure 6.7. It is shown that the performance with the original technique is severely degraded by the presence of errors in the antenna characteristics, and the performance obtained with conventional calibration techniques is degraded due to the presence of the mast. Logically, this degradation is concentrated where front to back ratio is smaller.

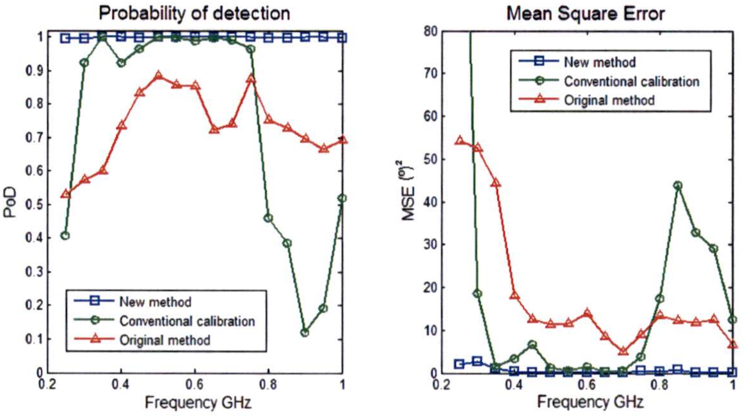

Figure 6.7: PoD and MSE for the extended, original and conventional calibration techniques.

6.3.2 Blind calibration techniques

The blind methods are on-line calibration techniques, signal parameters and the steering matrix are estimated at the same time. In general, there is no previous assumption about the array topology or antennas characteristics, so these methods are virtually immune to mutual coupling and errors. On the other hand, this suppose a waste of information a the resolution of this methods is typically worse. Moreover, sometimes the solution is not unique.

One blind calibration method was introduced in [54]. However, its use have been discussed [55, 56] due to ambiguity issues. The Independent Component Analysis has also been employed. This technique is able to recover to separate the signals by its direction of arrival, and it is also employed for calibration using pilot signals with unknown directions of arrival [57]. The ICA technique inherently suffers from magnitude and permutation ambiguities, but these difficulties have been overcome with some post-processing [58].

Chapter 7

Conclusions and future work

7.1 Conclusions

Once the results that have been obtained in this project have been shown in previous chapters, now it is time be expose the more important conclusions we have achieved.

The main objective of this thesis was the design of Radio Direction Finder. To this end, several tasks, which include single element antenna design, implementation of DOA estimation algorithms, antenna array design and the analysis of suitable calibration techniques, have been accomplished.

As for the antenna design, the elliptically shaped dipole antenna, also called butterfly antenna, has been adopted as the single radiating unit. An extensive parameter study has been carried out, ratifying that this antenna presents excellent ultra-wideband properties, and proving that this antenna features robust circuital and radiation properties against conformal deformations. In addition, a suitable antenna radome is adopted to enhance the front-to-back radiation ratio over the whole operational bandwidth, as well as to increase environmental durability of the structure.

Regarding with the antenna array design, an algorithm-oriented design procedure has been presented. This procedure is focused on the enhancement of the DOA estimation performance and the description of the physical limitations of the system, such as minimum separation between radio signals, minimum SNR, and maximum detectable number of signals.

The MUSIC algorithm is the estimation technique that has been implemented. This algorithm is one of the most popular DOA estimation techniques, and thus makes the design comparable with other systems. Furthermore, the MUSIC algorithm is usually employed in some of the ultra-wideband DOA estimation algorithm, especially in those based on the Coherent Signal-Subspace Method. Therefore, the design is also suitable for ultra-wideband DOA estimation.

Finally, the calibration techniques have also been studied. An overview of the different calibration techniques has been presented, and a novel calibration technique has been developed. This technique takes into account the errors in the antenna characteristics, and the mutual coupling between the antenna elements and supporting structure. Therefore, this technique is superior to the conventional calibration techniques in the presence of large supporting structures, such a mast.

7.2 Future work

Inherent to the nature of engineering, any system can follow an infinitely long enhancement process. Therefore, some possible work lines are addressed in this section, which could contribute to the development of a more complete and better system:

- First of, the elliptically shaped dipole have been successfully adopted as the single antenna element, showing robust circuital and radiation properties for its implementation in RDFs. However, one of the limitations of this antenna is its vertical polarization. Therefore, the adoption of diversely polarized ultra-wideband antennas could be studied. It must be remarked that these antennas must be conformal and compatible with the array geometry.
- A suitable radome has been designed, which improves the front-to-back radiation ratio protecting the antenna against the mast interferences. In spite of this, the development of antenna radomes is an open research area, and many other structures, such as multi-layered dielectric superstrates could be employed.
- This system has been designed for control applications, where there is no previous knowledge about the characteristics of the incoming signals, so it have been focused on very general algorithms that allows the detection of both narrow-band and ultra-wideband signals. However, it is a potentially versatile system, which can take advantage of previous knowledge about the signals. Therefore, the design and implementation of additional modules for specific scenarios is recommended. For example, TOA/DOA algorithms for ultra-wideband multipath scenarios and single-snapshot algorithms for radar detection.

Appendix A

Numerical techniques for electromagnetics

A.1 The Finite Integration Technique

A.1.1 Introduction

The Finite Integration Technique (FIT) was first proposed more than 30 years ago (1977) [3] as a method for the simulation of electromagnetic fields and of various coupled problems. The key idea was to use in the discretization the integral, rather than the differential form of Maxwell equations. [4]

FIT is one of the most popular algorithms for solve electromagnetic problems, in both time and frequency domain, including a wide variety of materials, and from DC to THz. The success of the Finite Integration Technique is probably mainly due to three factors. First, it is an algorithm with a sound theöretical foundation (among others, stability, orthogonality of numerically computed modes, energy and charge conservation were demonstrated in a very early stage). Second, it is applicable not only in frequency, but also in time domain, allowing thus the simulation of very large or very complex structures. Last, it is applicable to a variety of mesh types.

A.1.2 Numerical discretization of Maxwell's equations.

The discretization process of the FI-method begins with the restriction of the electromagnetic field problem, transforming an open boundary problem in a simply connected and bounded space region $\Omega \varepsilon R^3$. The computational domain Ω is also decomposed in a finite number of cells V_i such as tetra- or hexahedral under the premise that all cells have to fit exactly to each other. This decomposition yields the finite cells complex G, which serves as a computational grid.

For example, a hexahedral decomposition for Cartesian coordinates:

$$G := \{V_{i,j,k} \epsilon R^3 | V_{i,j,k} := [x_i, x_{i+1}] \times [y_i, y_{i+1}] \times [z_i, z_{i+1}],\ i = 1, ..., I-1, j = 1, ..., J-1, k = 1, ..., K-1\}$$

Results in the total number of $N_p = I \cdot J \cdot K$ mesh points for $(I-1) \cdot (J-1) \cdot (K-1)$ mesh cells.

The discretization of the complete set of Maxwell equations requires the introduction of a second cell complex $\widetilde{G}$. For the Cartesian tensor product grid G the dual grid $\widetilde{G}$ is defined by taking the foci of the cells of G as grid points for the mesh cells of $\widetilde{G}$ or viceversa. With this definition there is a one-to-one relation between the cell edges of G cutting the cell surface of $\widetilde{G}$ and viceversa. The dual grid $\{G, \widetilde{G}\}$is shown in the figure A.1.

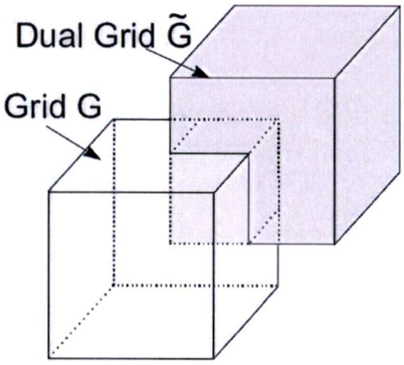

Figure A.1: Dual grid $\{G, \widetilde{G}\}$

Maxwell's equations and the related material equations are transformed from the continuous to the discrete space by allocating electric voltages on the edges and electric fluxes on the faces of a grid ("primary grid") and magnetic voltages on the edges and magnetic fluxes on the faces of a second grid ("dual grid"), as it is showed in the figure A.2.

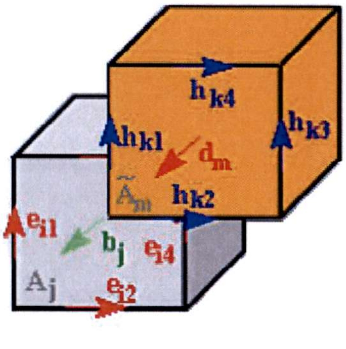

Figure A.2: Allocation of the voltages and fluxes in the dual grid$\{G, \widetilde{G}\}$

Where:

$e_{i2} = \hat{e}_x(i,j,k) = \int_{(x_i,y_i,z_i)}^{(x_{i+1},y_i,z_i)} \vec{E} \cdot d\vec{l}$

$b_j = \hat{\hat{b}}_z(i,j,k) = \iint_S \vec{B} \cdot d\vec{S}$

With this definitions, it is possible to build topological matrix operators equivalent to the curl, divergence and gradient operators. This discretization yields in the discrete equivalent of Maxwell equations, also called the Maxwell Grid Equations (MGE):

$$
\begin{array}{cc}
\oint_S \vec{E}\cdot d\overrightarrow{l} = -\iint_S \frac{d}{dt}\vec{B}\cdot d\vec{S} & C\cdot\hat{e} = -\frac{d}{dt}\hat{\hat{b}} \\
\oint_S \vec{H}\cdot d\overrightarrow{l} = \iint\left(\frac{d}{dt}\vec{D}+\vec{J}\right)\cdot d\vec{S} & \widetilde{C}\cdot\hat{h} = \frac{d}{dt}\hat{\hat{d}}+\hat{\hat{j}} \\
\oiint_{\partial V} \vec{B}\cdot d\vec{S} = 0 & S\cdot\hat{\hat{b}} = 0 \\
\oiint_V \vec{D}\cdot d\vec{S} = \iiint_V \rho\cdot dV & \widetilde{S}\cdot\hat{\hat{d}} = q
\end{array}
$$

Table A.1: Maxwell equations and Maxwell Grid Equations

$C, \widetilde{C}$ and $S, \widetilde{S}$ are the topological matrix operators for the curl and the divergence, with dimensions $3N_p \times 3N_p$ and $N_p \times 3N_p$. $\hat{e}, \hat{h}$ are the electric and magnetic voltages with dimensions $3N_p \times 1$. $\hat{\hat{d}}, \hat{\hat{b}}$ are the electric and magnetic fluxes with dimensions $3N_p \times 1$.The resulting equations are a exact representation of Maxwell equations on a grid doublet. The use of integral degrees of freedom, i.e. voltages and fluxes, instead of field components (such as used in FDTD) allows not only a very elegant way of writing the matrix form of Maxwell equations, but also has important algorithmic-theoretical and numerical consequences [6]. In fact, measurable quantities are also of integral type: for instance, the electric field strength cannot be measured directly, but through the intermediary of the electric voltage along a very short path.

The approximation of the method itself enters when the integral voltage- and flux state-variables allocated on the two different cell complexes are to be related to each other by the constitutive material equations.

$$
\begin{array}{cc}
\overrightarrow{D} = \epsilon_0\overrightarrow{E} + \overrightarrow{P} & \hat{\hat{d}} = M_\epsilon\cdot\hat{e}+\hat{\hat{p}} \\
\overrightarrow{B} = \mu_0\overrightarrow{H} + \overrightarrow{M} & \hat{h} = M_\nu\hat{\hat{b}} - \hat{m} \\
\overrightarrow{J} = \sigma\cdot\overrightarrow{E} & \hat{\hat{j}} = M_\kappa\cdot\hat{e}
\end{array}
$$

Table A.2: Constitutive material equations

Here M_ε is the permittivity matrix, M_κ is the (usually singular) matrix of conductivities, M_ν the matrix of reluctivities and $\hat{\hat{p}}$ and $\hat{m}$ arise from permanent electric and magnetic polarizations. The matrix are diagonal for diagonal or isotropic material tensors. Since the MGE are an exact representation of the Maxwell equations the numerical discretization error is found to be located in the discrete constitutive material equations. They contain the averaged information of the material and of the grid geometry and dimensions.

In fact, each cell is filled with only one material, which yields to the staircase problem of curved boundary surfaces. To overcome this problem, different mesh types can be employed.

A.1.3 Mesh types

Before solving an electromagnetic problem, the structure needs to be spatially discretized. As anticipated, the selection of the mesh type is not a trivial task, but it has great influence on the accuracy and computational load. The most often employed discretization meshes are hexahedral, tetrahedral, conformal-hexaedral and Perfect Boundary Approximation (PBA).

The hexahedral meshes have the advantage that they can be easily used in both time- and frequency-domain algorithms. In time domain they lead to very efficient algorithms in terms of memory and computing-time. The mesh generation is quite straightforward, even for very complicated geometries. The main disadvantages of the classical hexahedral mesh are the staircase approximation of curved surfaces, sometimes with severe consequences on the solutions accuracy, and the fact that if a fine mesh is needed in a small zone of the structure, it will be extended through the entire computational domain.

The tetrahedral meshes have the advantage of allowing a good approximation of curved surfaces. Their main disadvantage is that such a mesh is not appropriate for time-domain algorithms: the resulting matrices (for any numerical method) can be efficiently solved in frequency-domain but due to their nondiagonal character, they are inefficient in time-domain algorithms. Last, but not least, it should be pointed out that the generation of the tetrahedral mesh is not a trivial task.

The conformal hexahedral meshes are based on generalized non-orthogonal grids, including a local interpolation scheme for field components. Fulfilling the symmetry condition in this interpolation process, an explicit time-stepping method with proven stability properties is obtained. As the method reduces to standard FIT for orthogonal meshes, interfacing orthogonal with non-orthogonal grids is trivial. The numerical cost is increased by the interpolation scheme by a factor between 2 and 3 for 2D- or 3D-problems, respectively. The application of the conformal hexaedral meshes is sometimes limited by the increase of the numerical cost, and by the requirement to supply a body-fitted, structured, non-orthogonal grid.

In the Perfect Boundary Approximation the computational grid does not have to be conformal to the rounded boundaries. Instead, also sub-cellular information is taken into account, leading to an algorithm with second order accuracy for arbitrary shaped boundaries. Except for the more complicate preprocessing, there is only slightly additional numerical cost during the iteration. Moreover, the grid generation becomes very easy, as there is no need for a highly resolved mesh near by non-orthogonal shapes. In most cases, even equidistant meshes produce highly accurate results.

In conclusion, the PBA technique maintains all the advantages of the structured Cartesian grids, while allowing an accurate modeling of curved boundaries. Nowadays, it is implemented on CST MWS.

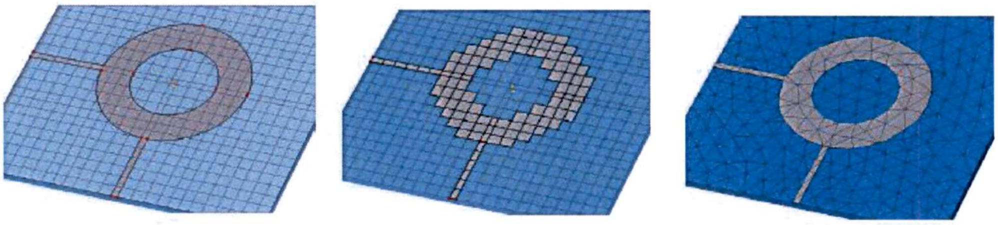

Figure A.3: Different meshes. a) PBA. b) Hexahedral. c) Tetrahedral.

A.1.4 Energy and charge conservation

The Maxwell Grid Equations (MGE) obtained with FIT possess the inherent properties of Maxwell equations with respect to energy and charge conservation and thus ensure a specially favorable stability and convergence behavior in the numerical implementation.

First, the topological matrix operators present the following properties [5]:

$$S \cdot C = 0$$

$$\widetilde{S} \cdot \widetilde{C} = 0$$

$$C = \widetilde{C}^T$$

$$G = -\widetilde{S}^T$$

$$\widetilde{C} \cdot S^T = 0$$

$$C \cdot S^T = 0$$

Corresponding to the vector-analytical identities:

$$\nabla \cdot \nabla \times \overrightarrow{A} = 0$$

$\nabla \times \nabla\phi = 0$

Hence, the continuity equation:

$\widetilde{S}(\widetilde{C} \cdot \widetilde{h}) = \widetilde{S}\left(\frac{d}{dt}\hat{\hat{d}} + \hat{\hat{j}}\right) = 0$

The discrete continuity equation ensures that no spurious charges will occur. Such non-physical charges would result in static fields contaminating discrete transient field solutions.

If electromagnetic field processes are calculated in time domain, energy conservation of the time and space discrete system becomes of paramount importance. If this condition is violated, a necessary prerequisite for a long-term stable time integration of electromagnetic wave-propagation phenomena without artificial numerical damping is not available. For the FI-Technique the proof of this condition was given in[5], [7] for resonator structures with perfectly conducting walls.

A.1.5 Time Domain discretization

In previous subsections the discretization procedure of the spatial domain has been presented. It yields in a discretized formulation of the Maxwell equations, the Maxwell Grid Equations. These equations are a exact representation of the original ones and only contain topological information, whereas approximations are made in the material constitutive equations. They contain the averaged information of the material and of the grid geometry and dimensions.

It also have been shown that both energy and charge conservation hold in this spatially discretized formulation.

However, it is also necessary to discretize the time dependence of the electromagnetic process in order to allow numerical calculation. One formulation of the time domain discretization could be the following:

$f(t),\, t\,\varepsilon\,[t_0, t_n] \rightarrow f(t_i),\, t_i\,\varepsilon\,[t_0, t_n],\, i = 0, ..., n$

Fortunately, the algebraic properties of the MGE of FIT ensure charge and energy conservation when time discrete schemes such as the explicit Leapfrog FDTD scheme[8] or certain second order implicit methods [15], [16] are employed. Hence, it is possible to evaluate magnetic and electric grid voltages at the same time or to use a dual-staggered grid for the time axis.

Implicit time integration schemes can also be applied to non-gauged magneto-quasi-static formulations, which yield singular matrix systems that still can be numerically tackled due to their consistency given with the FIT approach. These results clearly distinguish these time integration schemes from many alternative methods which do not rely on space and time stability and thus may become unstable or inaccurate in long-term calculations.

A.2 Finite Difference Time Domain - FDTD

Finite-difference time-domain (FDTD) method is a popular computational electrodynamics modeling technique. As it is a time domain method, it is well suited for simulations covering a wide band of frequencies. The basic FDTD space grid and time-stepping algorithm were first introduced by Yee in 1966 [14], but the descriptor "Finite Difference Time Domain" was created by Allen Taflove, in 1980.

The FDTD method belongs to the general class of grid-based differential time-domain numerical modeling methods. The time-dependent Maxwell's equations in partial differential form are discretized using central-difference approximations to the space and time partial derivatives. The resulting finite-difference equations are determined in a leapfrog manner: the electric field vector components in a volume of space are solved at a given instant in time; then the magnetic field vector components in the same spatial volume are determined at the next instant in time; and the process is repeated over and over again until the desired transient or steady-state electromagnetic field behavior is fully evolved. In order to describe how the FDTD algorithm works it is necessary to consider the differential form of Maxwell equations. It can be seen that the change in the E-field in time is dependent on the change in the H-field across space. This results in the basic FDTD time stepping relation. At any point in space, the updated value of the E-field in time is dependent on the stored value of the E-field and the numerical curl of the local distribution of the H-field in space.[14]. The H-field is time-stepped in a similar manner. At any point in space, the updated value of the H-field in time is dependent on the stored value of the H-field and the numerical curl of the local distribution of the E-field in space. Iterating the E-field and H-field updates results in a marching in time process wherein sampled-data analogs of the continuous electromagnetic waves under consideration propagate in a numerical grid stored in the computer memory.

This procedure can be applied in 1-D, 2-D and 3-D problems. However, it is complicate to calculate the curl when multiple dimensions are considered. In 1966 Yee also introduced the commonly know Yee lattice (Figure A.4) It is based in spatially staggering the vector components of the E-field and H-field about rectangular unit cells of a Cartesian computational grid so that each E-field vector component is located midway between a pair of H-field vector components, and conversely. This scheme has proven to be very robust, and remains at the core of many current FDTD software constructs. Furthermore, Yee proposed a leapfrog scheme for marching in time wherein the E-field and H-field updates are staggered so that E-field updates are sampled midway during each time-step between successive H-field updates, and conversely.

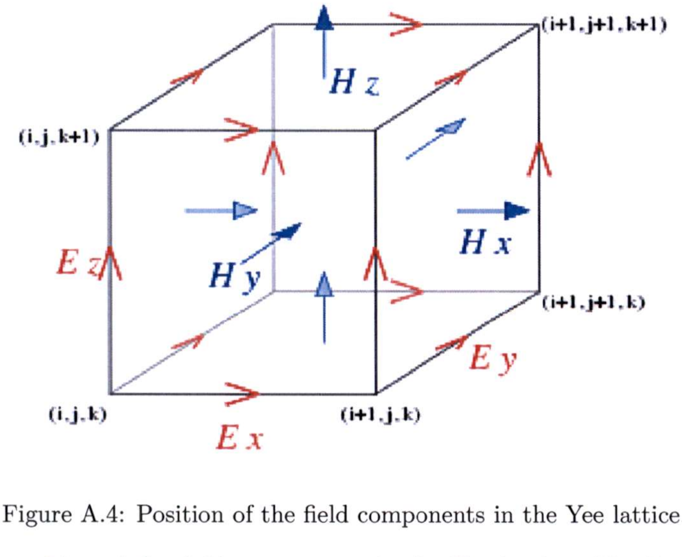

Figure A.4: Position of the field components in the Yee lattice.

Figure A.4 shows the position of the field components in the Yee lattice. The E- components are in the middle of the edges and the H- components are in the center of the faces. A formulation of the Maxwell equations under this grid is introduced in order to give a deeper description of the FDTD method.

In a rectangular coordinate system, the Maxwell equations are equivalent to the following system of scalar equations:

$$-\frac{\partial B_x}{\partial t} = \frac{\partial E_z}{\partial y} - \frac{\partial E_y}{\partial z}$$

$$-\frac{\partial B_y}{\partial t} = \frac{\partial E_x}{\partial z} - \frac{\partial E_z}{\partial x}$$

$$\frac{\partial B_z}{\partial t} = \frac{\partial E_x}{\partial y} - \frac{\partial E_y}{\partial x}$$

$$\frac{\partial D_x}{\partial t} = \frac{\partial H_z}{\partial y} - \frac{\partial H_y}{\partial z} - J_x$$

$$\frac{\partial D_y}{\partial t} = \frac{\partial H_x}{\partial z} - \frac{\partial H_z}{\partial x} - J_y$$

$$\frac{\partial D_z}{\partial t} = \frac{\partial H_y}{\partial x} - \frac{\partial H_x}{\partial y} - J_x$$

A grid point of the space and a function of space and time are

$$(i, j, k) = (i\Delta x, j\Delta y, k\Delta z)$$

$$F(i\Delta x, j\Delta y, k\Delta z, n\Delta t) = F^n(i, j, k)$$

respectively.

Then the previous equations can be rewritten:

$$\frac{B_x^{n+1/2}(i,j+\frac{1}{2},k+\frac{1}{2})-B_x^{n-1/2}(i,j+\frac{1}{2},k+\frac{1}{2})}{\Delta t} = \frac{E_y^n(i,j+\frac{1}{2},k+1)-E_y^n(i,j+\frac{1}{2},k)}{\Delta z} - \frac{E_x^n(i,j+1,k+\frac{1}{2})-E_y^n(i,j,k+\frac{1}{2})}{\Delta y}$$

The update equations for other field components can be similarly obtained.

Strengths of FDTD:

- FDTD is a versatile and easy to understand technique.
- FDTD is time-domain technique, so it is useful for broadband applications.
- E a H fields are calculated at any point in time and space, so it is possible to build animations useful in understanding physical processes responsible for the electromagnetic behavior of the structure under investigation.
- A wide variety of linear and nonlinear dielectric and magnetic materials can be naturally and easily modeled.
- E and H are calculated directly, so the use of transformations is avoided.

Weakness of FDTD:

- FDTD requires gridding of the entire computational domain. So the discretization must fit the smallest wavelength in the frequency band of interest, and the smallest detail of the structure. Large structures operating at high frequencies or with thin features result in very large computational load.
- Calculating the fields at some distance requires post-processing.
- Since the computational domain must be finite, it is needed to insert artificial absorbing boundaries into the simulation space. Care must be taken to minimize errors introduced by such boundaries.
- Since the fields are calculated in a forward march-in-time process, the time response of the medium must be modeled explicitly. In general, it requires a computationally heavy convolution.

A.3 Method Of Moments - MOM

The Method Of Moments, introduced by Harrington in 1968 [5, 12], was one of the first method widely employed in antenna design. This method is based on integral equations (IE) and Green's functions and it is also known as the Boundary Elements Method (BEM).

Generally, the MOM is employed in the frequency domain. Since it is not necessary to use a full domain discretization, it is better suited for long and thin antennas than the differential methods, which need a dense mesh to cover thin structures.

In the method of moments, the radiating structure is replaced by equivalent currents. These are normally surface currents. Volumetric currents can be used for inhomogeneous dielectric bodies.

In radiation and scattering problems the integral equation can be produced in different forms. The most popular integral equations are the Electric Field Integral Equation (EFIE) and Magnetic Field Integral Equation (MFIE). The integral equations are produced invoking the boundary conditions. The EFIE enforces the boundary condition of the tangential electric field and the MFIE enforces the boundary condition of the tangential magnetic field. The EFIE is valid for both open and closed surfaces, while the MFIE is only valid for closed surfaces.

$$\vec{n} \times \vec{E}(\overrightarrow{r}) = \vec{n} \times \iint_S \left[jk\eta \vec{J}_s(\vec{r}) \cdot G(\vec{r},\vec{r}\,') + \tfrac{\eta}{jk}\nabla_s' \vec{J}_s(\vec{r}\,') \cdot \nabla G(\vec{r},\vec{r}\,')\right] d\vec{S}\,' \ \forall \vec{r},\vec{r}\,' \epsilon S$$

$$\tfrac{1}{2}\vec{J}_s(\vec{r}) = \vec{n} \times \vec{H} + \vec{n} \cdot \oiint_s \vec{J}_s(\vec{r}\,') \times \nabla G(\vec{r},\vec{r}\,') dS' \ \forall \vec{r},\vec{r}\,' \epsilon S$$

The solution can be obtained numerically by reducing the integral equation to a series of linear algebraic equations that may be solved by conventional matrix equation techniques. To facilitate this, the unknown function is approximated by an expansion of N terms (basis functions) with constant but unknown coefficients. If F is a integrodifferential operator, and g is the unknown function, then the integral equation and the function decomposition can be written as follow:

$$F(g) = h$$

$$g(\vec{r}) = \textstyle\sum_{n=1}^{N} a_n \cdot g_n(\vec{r}) \implies \sum_{n=1}^{N} a_n \cdot F(g_n) = h$$

Choosing the basis is a very important step. In general, it is chosen a set that has the ability to accurately represent and resemble the anticipated unknown function, while minimizing the computational effort to employ it. These functions can be divided in two classes, the sub-domain functions, which are zero only over a part of the structure, and the entire domain functions, forming an orthogonal set.

In order to obtain the solution for this N amplitude constants, N linearly independent equations are needed. These equations can be built choosing N observation points, as in the point matching technique. It is possible to improve point matching defining an inner product with some properties, there are several options but one used in the Method of Moments is:

$$\langle w, g\rangle = \textstyle\iint_s w \cdot g^* dS$$

A set of N weighting functions is defined, and then the matrix equation is constructed. This equation can be solved via matrix inversion.

$$\textstyle\sum_{n=1}^{N} a_n \langle w_m, F(g_n)\rangle = \langle w_n, h\rangle \ m = 1...M$$

$$[F_{mn}] \cdot [a_n] = [h_m] \implies [a_n] = [F_{mn}]^{-1} [h_m]$$

The weighting functions must be linearly independent, in order to obtain a set of N linearly independent equations. Simplicity must be also taken into account. On particular choice of the weighting functions is the Galerkin method, in which the condition $w_n = g_n$, is imposed.

A.4 Finite Element Method - FEM

The Finite Element Method is a general numerical method for finding approximate solutions of Partial Differential Equations or Integral Equations. It is a very popular numerical method, employed in different engineering areas like aeronautical, bio-mechanical, automotive industries... Moreover, it is able to solve problems of different disciplines, like electromagnetics, thermal, fluid and structures problems.

The development of the Finite Element Method traces back to the work of Alexander Hrennikoff (1941) [6] and Richard Courant (1942) [4]. Although their work was different, it shares an essential characteristic, the discretization of a continuous domain into a set of discrete sub-domains, usually called elements.

This is key idea behind FEM algorithm, the domain of interest is represented as an assembly of finite elements. Approximating functions in finite elements are determined in terms of nodal values of a physical field which is sought. A continuous physical problem is transformed into a discretized finite element problem with unknown nodal values. For a linear problem a system of linear algebraic equations should be solved. Values inside finite elements can be recovered using nodal values.

The division of the domain can be made with triangular or quadrilateral cells in two dimensions or with tetrahedral, hexahedral, prismatic or pyramidal cells in three dimensions. These cells can also have curved faces when we need to discretize domains with curved boundaries. The most often used cells are those triangular in 2D and tetrahedral in 3D.

The FEM is usually used in frequency domain and each solving of the equations give the solution for one frequency. Repeated runs and interpolation are used to obtain the systems response over a frequency band. This might give problems for resonant systems, especially those with high Q, where it is not easy to get the resonant frequency unless you sweep the frequency carefully.

In order to give a general description of how the FEM algorithm works, it could be summarizes in the following steps [7]:

1. Discretize the continuum. The first step is to divide a solution region into finite elements. The finite element mesh is typically generated by a preprocessor program. The description of mesh consists of several arrays main of which are nodal coordinates and element connectivities.
2. Select interpolation functions. Interpolation functions are used to interpolate the field variables over the element. Often, polynomials are selected as interpolation functions. The degree of the polynomial depends on the number of nodes assigned to the element.
3. Find the element properties. The matrix equation for the finite element should be established which relates the nodal values of the unknown function to other parameters. For this task different approaches can be used; the most convenient are: the variational approach and the Galerkin method.
4. Assemble the element equations. To find the global equation system for the whole solution region we must assemble all the element equations. In other words we must combine local element equations for all elements used for discretization. Element connectivities are used for the assembly process. Before solution, boundary conditions (which are not accounted in element equations) should be imposed.
5. Solve the global equation system. The finite element global equation system is typically sparse, symmetric and positive definite. Direct and iterative methods can be used for solution. The nodal values of the sought function are produced as a result of the solution.

6. Compute additional results. In many cases we need to calculate additional parameters. For example, in mechanical problems strains and stresses are of interest in addition to displacements, which are obtained after solution of the global equation system.

Appendix B

CODES

B.1 MUSIC algorithm

```
function A = agenerator(g,m,r,f)

% generator of the theoric steering matrix of a circular array

% g <- gain diagram of a single sensor
% m <- number of antennas
% r <- array radius
% f <- frequency of operation
% A -> theoric steering matrix

N = length(g);
gain = sqrt(10.^(g/10));
phi = 2*pi/m; phiindex = round(N/m)+1;
k = 2*pi*f/3e8;
A = zeros(m,N);

for s = 1:m

     A(s,:) = gain.*exp(i*k*r*cos([0:1:N-1]*2*pi/N-(s-1)*phi));
     gain = gain( mod((1:end)-phiindex-1, end)+1 );   %rotate radiation pattern

end


function [X,Ae,C] = generatedata(SNR,DOA,phase,error,L,f,g,m,r)

% generate data for the MUSIC algorithm

%      SNR     <- signal to noise ratio
%      DOA     <- DOA of the incomming signals
%      phase   <- phase shift between the carriers of the incomming signals
%      error   <- antenna's errors
%      L       <- number of snapshots
%      f       <- frequency of operation
%      g       <- antenna's gain diagram
%      m       <- number of antennas
%      r       <- array radius
%      X       -> generated data
%      Ae      -> actual steerin matrix
%      C       -> mutual coupling matrix

A = agenerator(g,m,r,f);

% mutual coupling
C = couplingmatrix(f);
```

```
% including mast
gmast = 5;
gant = 10^(g(round(length(g)/2))/10);
zmast = gmast*gant*3e8*exp(j*2*pi*f*r/3e8)/(f*4*pi*r);
C = [C zmast*ones(m,1)];

% errors in the antenna characteristics
E = (1+random('norm',0,error,1,m)).*exp(j*random('norm',0,error*2*pi,1,m));
E = [ones(m,m)*diag(E) E.'];
C = C.*E;
Ae = C*[A;ones(1,length(A(1,:)))];

% generate signals
sigma = sqrt(10^(-SNR/10)); % noise std
Ts = 0.1/f;
T = [0:1:L-1]*Ts;
X = zeros(m,L);

for q = 1:length(DOA)

     a = Ae(:,round(DOA(q)*length(Ae(1,:))/360)+1);
     % FM modulation
     x = cos(2*pi*f/10*T+phase(q));
     opt = 0.1*2*pi/(max(max(x)));
     s = cos(2*pi*f*T + opt*cumsum(x));
     X = X+a*s;

end
noise = random('norm',0,sigma,m,L);
X = X+noise;


function C = couplingmatrix(f)
% create array mutual coupling matrix
%   f <- frequency
%   C -> mutual coupling matrix
% import Array Scattering parameters

s21mag = importdata('C:\...\s12mag.txt');
freq = s21mag.data(:,1)';
s21mag = s21mag.data(:,2);
s21pha = importdata('C:\...\s12phase.txt');
s21pha = s21pha.data(:,2);
s21 = (s21mag.*exp(i*s21pha*pi/180))';
s31mag = importdata('C:\...\s13mag.txt');
s31mag = s31mag.data(:,2);
s31pha = importdata('C:\...\s13phase.txt');
s31pha = s31pha.data(:,2);
s31 = (s31mag.*exp(i*s31pha*pi/180))';

% create coupling matrix

C21 = sqrt(s21(round((f/1e9-0.15)*1000/1.35)));
C31 = sqrt(s31(round((f/1e9-0.15)*1000/1.35)));
C = zeros(5,5);
C(1,:) = [1 C21 C31 C31 C21];
for s = 2:5   % toeplitz structure

     C(s,:) = C(s-1,[end 1:end-1]);

end


function MSE=mse(DOA,doa)

% calculator of the MSE of the DOA estimation
%      DOA  <- DOA of the incident signals
%      doa  <- estimated DOAs
```

```
%       MSE  -> mean square error of the estimation

L=length(DOA);
MSE=zeros(1,L);
for s=1:L

     error=abs(DOA-doa);
     ind=find(error>180);
     error(ind)=360-error(ind);
     MSE(s)=sum(error.^2)/L;
     doa=doa([ end 1:end-1 ]);

end
MSE=min(MSE);
end


function [F,doa] = findpeaks2(P,n)

% Find n maximum peaks in the MUSIC spectrum
%       P    <- MUSIC spectrum
%       n    <- number of signals
%       F    -> peaks value
%       doa  -> doa of the peaks
doa = [];
F = [];
df = [];
N = length(P);
prev = [N 1:N-1];
post = [2:N 1];
q = 1;
for s = 1:N                          % collect all maxima

     if (P(s)>P(prev(s))) && (P(s)>P(post(s)))
         F(q) = P(s);
         df(q) = s;       % save maxima index
         q = q+1;
     end

end
[F,I] = sort(F,’descend’);      % maximum in descendent order
df = df(I);
if length(df) >= n
doa = df(1:n)*360/N;     % select the largest maxima end


function z = average(v,w)

% filter the vector v averaging

%    v  -> input vector
%    w  -> window size (even)
%    z  -> output vector

Q=length(v);
for q=1:Q

     z(q)=sum(v(mod(q-w/2,Q-1)+1:mod(q+w/2,Q-1)+1))/w;

end


function [P,doa,n]=music(X,A,t)

% The MUSIC method for azimuth DOA estimation

%       X    <- the sensors data
%       A    <- steering matrix
%       t    <- threshold for the noise subspace
```

```
%       P    -> music spectrum
%       doa  -> the vector of DOA estimates
%       n    -> number of incomming signals

[M,N]=size(X); % M number of sensors, N number of snapshots

% compute the sample covariance matrix
R=X*X'/N;

%eigendescomposition
[V,Dia]=eig(R);          %V eigenvectors, Dia eigenvalues
Y=sort(diag(Dia));
index=find(Y>t*min(Y));
n=length(index);         %number of signals
if n==0

     EN=V;

else

     EN=V(:,1:index(1)-1);     %noise subspace

end;

%calculate music espectrum and find the DOAs
[O,L]=size(A);
P=zeros(1,L);
s=1;
for s=1:L

     P(1,s)=(A(:,s)'*A(:,s))/(A(:,s)'*EN*EN'*A(:,s));
     s=s+1;

end;
P=average(P,14);
doa=[];
if n~=0

     [F,doa]=findpeaks2(P,n);
     doa=sort(doa);

end


function [P,n] = music2D(X,A,t)

% The MUSIC method for azimuth and elevation DOA estimation

%       X    <- the sensors data
%       A    <- steering matrix
%       t    <- threshold for the noise subspace
%       P    -> music spectrum
%       n    -> number of incomming signals

[M,N] = size(X); % M number of sensors, N number of snapshots

% compute the sample covariance matrix
R = X*X'/N;

%eigendescomposition
[V,Dia] = eig(R);       %V eigenvectors, Dia eigenvalues
Y = sort(diag(Dia));
index = find(Y>t*min(Y));
n = length(index);      %number of signals
if n == 0

     EN = V;

else

     EN = V(:,1:index(1)-1);  %noise subspace
```

```
end;

%calculate music espectrum and find the DOAs
[m,L,Q] = size(A);
P = zeros(Q,L);
for q = 1:Q

     for s = 1:L
         P(q,s) = (A(:,s,q)'*A(:,s,q))/(A(:,s,q)'*EN*EN'*A(:,s,q));
     end

end


function [P,doa,num] = uwbmusic(xf,r,J,fs)

% Modified MUSIC algorithm for uwb signals

%      xf   <- frequency components of the incoming signals
%      r    <- array radius
%      J    <- number of points of the DFT
%      fs   <- sampling frequency
%      P    -> music spectrum
%      doa  -> the vector of DOA estimates
%      n    -> number of incomming signals

[m,K,fbins] = size(xf); %number of antennas/snapshots/frequency bins

N1 = round(0.25*J/fs);
N2 = round(0.9*J/fs);
No = round((N1+N2)/2);

Tj = zeros(m,m);            % focusing matrix
Rj = zeros(m,m);            % frequency dependent correlation matrix
Rjo = zeros(m,m);
Ro = zeros(m,m);            % central correlation matrix
Po = zeros(m,m);
R = zeros(m,m);             % universal correlation matrix
Ro = (1/K)*xf(:,:,No-N1+1)*xf(:,:,No-N1+1)';

num = 2;          % number of signals

[V,Dia] = eig(Ro);
list = sort(diag(Dia),'Descend');
sig2 = sum(list(num+1:end))/length(list(num+1:end));
Po = Ro - sig2*eye(m);
for n = 1:fbins

     Rjo = (1/K)*xf(:,:,n)*xf(:,:,No-N1+1)';
     Rj = (1/K)*xf(:,:,n)*xf(:,:,n)';
     [U,S,V] = svd(Po'*Po);          % hermitian square roots
     root1 = U*sqrt(S)*V';
     [U,S,V] = svd(Rjo'*Rjo);
     root2 = U*sqrt(S)*V';
     Tj = Po*inv(root1)*inv(root2)*Rjo';
     R = R + Tj*Rj*Tj';

end
R = R/fbins;
fo = No*fs*1e9/J;
A=agenerator(m,r,fo);
[P,doa,num]=narrowmusic(R,A);
```

B.2 Calibration techniques

```
function A=matrixcalibration(Atrue,g,r,f)

% Calibration of the steering matrix based on "Simulation of mutual coupling effect
in circular arrays for Direction-Finding applications" by Tao SU, Kapil Dandekar and Hao Ling.
% Atrue <- coarse measured steering matrix
% g <- gain diagram of a single sensor
% r <- array radius
% f <- frequency of operation
% A -> calibrated steering matrix

[m,N]=size(Atrue);  %m number of antennas, N number of measured angles
gain=10.^(g/10);
gsampled=gain(round([0:1:N-1]*length(g)/N)+1);
Atheo=agenerator(gsampled,m,r,f); %theoric steering matrix
C=Atrue*Atheo'*inv(Atheo*Atheo'); %coupling matrix
Atheo=agenerator(g,m,r,f);
A=C*Atheo;


function M=ferreol(q,g,f,r)

% Estimation of the mutual coupling matrix of a UCA with an arbitrary number of elements.
Based on "On the introduction of an extended coupling % matrix for a 2D bearing
estimation with an experimental RF system", by Anne Ferrol, Eric Boyer, Pascal Larzabal and Martin Haardt.

%      q    <- set of measured steering vectors
%      g    <- antenna radiation pattern. Gain (dB)
%      f    <- frequency of operation
%      r    <- array radius
%      M    -> estimated mutual coupling matrix

[n,m] = size(q);                          % number of pilot signals and number of antennas
ind = round([0:1:n-1]*length(g)/n)+1;     % index of the incomming signals
A = agenerator(g,m,r,f);                  % steering matrix
Q = floor(m/2)+2;                         % number of model parameters
D = zeros(m+1,Q,m);                       % Zm = Dm*c
if mod(m,2) == 0

     I = eye(Q-1);
     Ii = I(Q-2:-1:2,:);
     Do = [I;Ii];
     Db = 1;
     D(:,:,1) = [Do 0;zeros(1,Q-1) 0];

else

     I = eye(Q-1);
     Ii = I(Q-1:-1:2,:);
     Do = [I;Ii];
     Db = 1;
     D(:,:,1) = [Do zeros(m,1);
     zeros(1,Q-1) 1];

end
for s = 2:m

     Do = D(1:m,1:Q-1,s-1);
     Do = Do([m 1:m-1],:);
     D(:,:,s) = [Do zeros(m,1);zeros(1,Q-1) 1];

end
T = zeros(m,Q);
Q2 = zeros(m*n,Q);
p = zeros(m*n,1);
for k = 1:n

     for s = 1:m
```

```
          T(s,:) = [A(:,ind(k)).' 1]*D(:,:,s);  % tm = b*Dm
     end
     Q2(m*(k-1)+1:m*(k-1)+m,:) = T;
     p(m*(k-1)+1:m*(k-1)+m,1) = q(k,:);

end
cp = inv(Q2'*Q2)*Q2'*p;               % MLE of the model parameters c = cp/cp(1);
M = zeros(m,m+1);
for s = 1:m

     M(s,:) = (D(:,:,s)*c).';

end


function M=ferreolextended2(q,g,f,r)

% extended Ferreol calibration including errors and dedicated to a 5-element UCA.

%      q    <- set of measured steering vectors
%      g    <- antenna radiation pattern. Gain (dB)
%      f    <- frequency of operation
%      r    <- array radius
%      M    -> estimated mutual coupling matrix

[n,m] = size(q);                        % number of pilot signals and number of antennas
ind = round([0:1:n-1]*length(g)/n)+1;  % index of the incomming signals
A = agenerator(g,m,r,f);                % steering matrix
Q = 15;                                 % number of model parameters
Do = zeros(m,Q,m);                      % Zm = Dm*c
Db = zeros(1,m,m);
D = zeros(m+1,Q+m);
I = eye(3,3);
Do(:,:,1) = [1 0 0 0 0 0 0 0 0 0 0 0 0 0 0;
             0 0 0 0 1 0 0 0 0 0 0 0 0 0 0;
             0 0 0 0 0 0 0 0 1 0 0 0 0 0 0;
             0 0 0 0 0 0 0 0 0 0 0 1 0 0 0;
             0 0 0 0 0 0 0 0 0 0 0 0 0 1 0];
Db(:,:,1) = [1 0 0 0 0];
D(:,:,1) = [Do(:,:,1) zeros(m,m);zeros(1,Q) Db(:,:,1)];
for s = 2:m

     Do(:,:,s) = Do(:,[end-2:end 1:end-3],s-1);
     Do(:,:,s) = Do([end 1:end-1],:,s);
     Db(:,:,s) = Db(:,[end 1:end-1],s-1);
     D(:,:,s) = [Do(:,:,s) zeros(m,m);zeros(1,Q) Db(:,:,s)];

end
T = zeros(m,Q+m);
Q2 = zeros(m*n,Q+m);
p = zeros(m*n,1);
for k = 1:n

     for s = 1:m
          T(s,:) = [A(:,ind(k));1].'*D(:,:,s);  % tm = b*Dm
     end
     Q2(m*(k-1)+1:m*(k-1)+m,:) = T;
     p(m*(k-1)+1:m*(k-1)+m,1) = q(k,:);

end
c = inv(Q2'*Q2)*Q2'*p;        % MLE of the model parameters
M = zeros(m,m+1);
for s = 1:m

     M(s,:) = (D(:,:,s)*c).';

end
```

Appendix C

Second subarray performance

Minimum SNR of operation

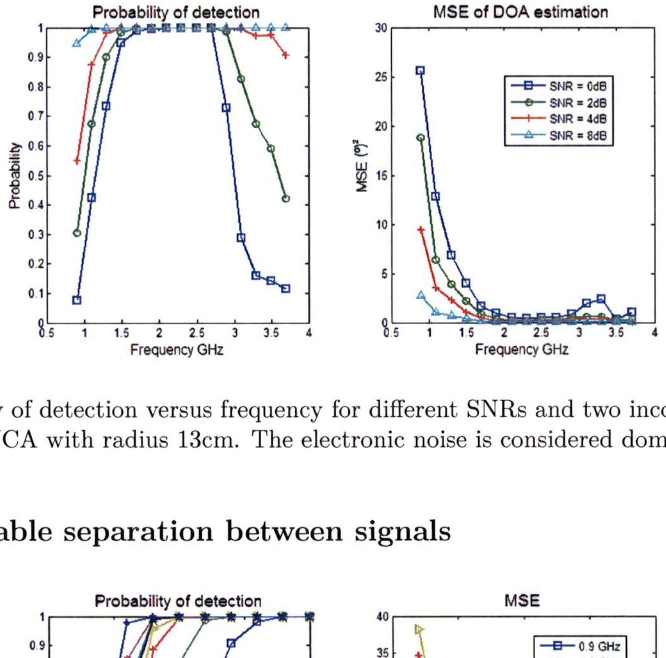

Figure C.1: Probability of detection versus frequency for different SNRs and two incoming signals separated by 20°. Five-element UCA with radius 13cm. The electronic noise is considered dominant.

Minimum detectable separation between signals

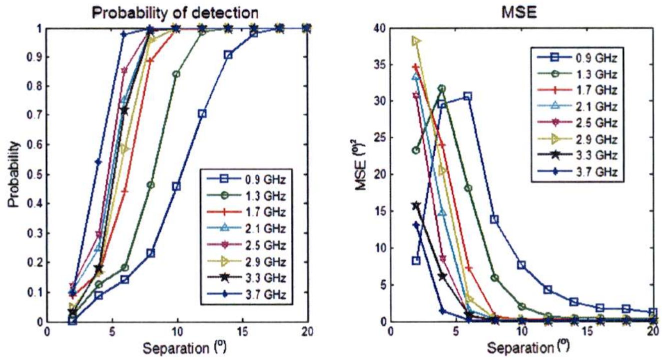

Figure C.2: Probability of detection and MSE for a five-element UCAwith radius 7.5cm. The incoming signals are separated by 20° and have a SNR of 20dB.

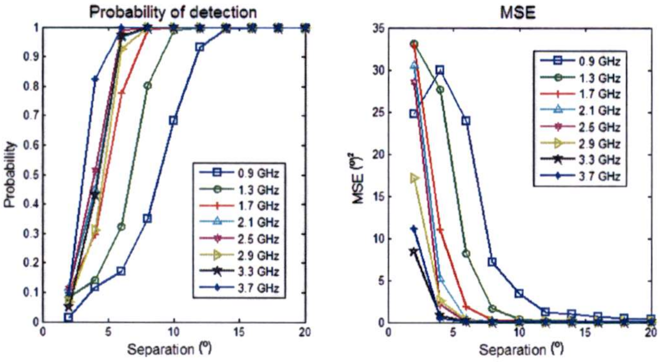

Figure C.3: Probability of detection and MSE for a five-element UCAwith radius 10cm. The incoming signals are separated by 20º and have a SNR of 20dB.

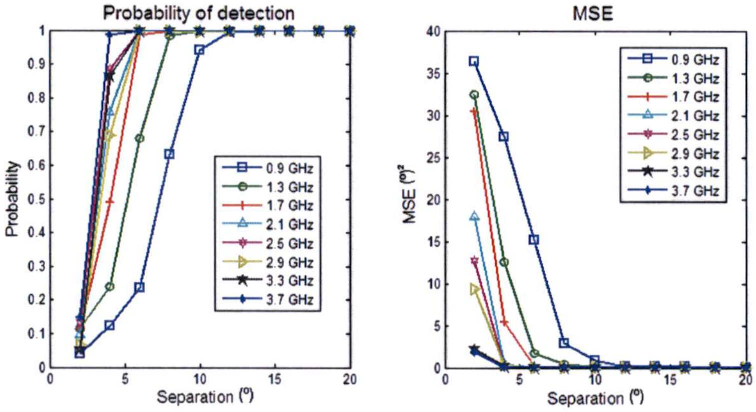

Figure C.4: Probability of detection and MSE for a five-element UCAwith radius 13cm. The incoming signals are separated by 20º and have a SNR of 20dB.

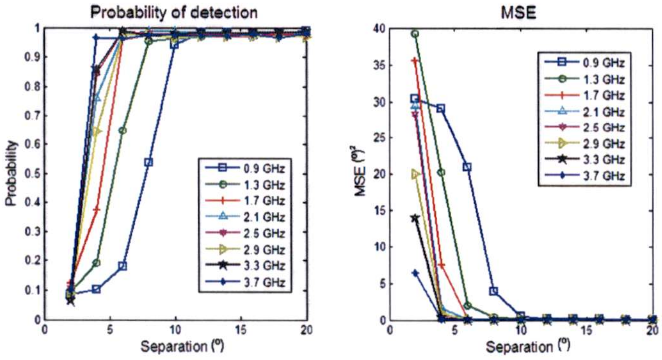

Figure C.5: Probability of detection and MSE for a seven-element UCAwith radius 13cm. The incoming signals are separated by 20º and have a SNR of 20dB.

Maximum detectable number of signals

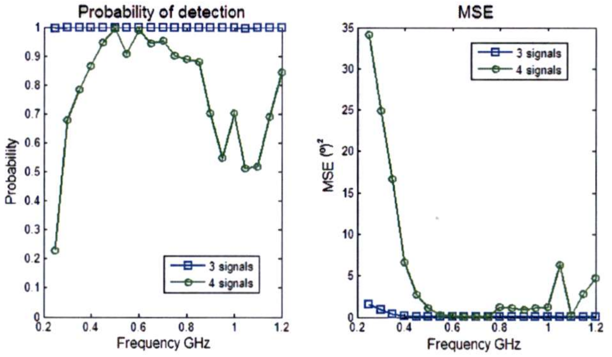

Figure C.6: Probability of detection and MSE for 4,5 and 6 incoming signals. The array geometry is an UCA with 5 antennas and radius 13cm.

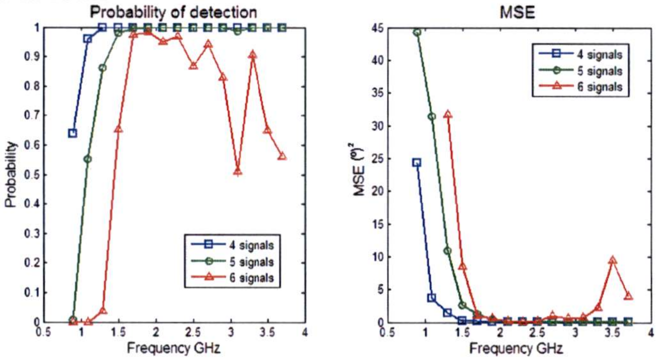

Figure C.7: Probability of detection and MSE for 4,5 and 6 incoming signals. The array geometry is an UCA with 7 antennas and radius 13cm.

Appendix D

Calibration techniques

The different sources of error and the calibration techniques have been discussed in the chapter 4. For a better understanding of the results, this appendix includes a brief description of the calibration techniques implemented.

D.1 Calibration based on matrix equation

One fast and direct calibration technique is based on solving the matrix equation impose by the model [50]. The mutual coupling effect expresed in matrix form is:

$$X = M \cdot A \cdot S + W$$

Therefore, the mutual coupling effect can be understood as a missmatch between the actual and theoretical steering matrix, that yields in the following matrix equations:

$$A_{true} = M \cdot A$$

Since A is calculated and A_{true} is provided by the measurement, it is possible to calculate the mutual coupling matrix M, using the pseudoinverse concept:

$$M = A_{true} A^{*} (A \cdot A^{*})^{-1}$$

Once M is known, it is possible to interpolate A_{true} with the required resolution. It is only necessary to employ M in the original matrix equation.

D.2 Calibration based on analytical modelling

The calibration technique implemented here is based on "On the introduction of an extended coupling matrix for a 2D bearing estimation with an experimental RF system" by Anne Ferréol, Eric Boyer, Pascal Larzabal and Martin Haardt. 2007. As anticipated, this calibration technique is based on the derivation of a analytical expression for the mutual coupling and the estimation of its parameters. Furthermore, this technique also compensate the influence of the supporting structure.

The effect of the mutual coupling has been modelled with the mutual coupling matrix Z:

$$X = Z \cdot A \cdot S + W$$

Therefore, the actual steering vectors differ from the theoric ones, but can be approximated with the mutual coupling matrix. Moreover, this model can be extended including the influence of the supporting structures. Thus, the approximation of the steering vector in the θ direction is given by:

$$\tilde{a}(\theta) = Z_0 \cdot a(\theta)$$

Or its extended version:

$$\tilde{a}(\theta) = Z_0 \cdot a(\theta) + Z_b \cdot a_b(\theta)$$

Where Z_b is the MxL coupling matrix between the M antennas and L supporting elements, and $a_b(\theta)$ is the steering vector of the supporting structure. Equivalently:

$$\tilde{a}(\theta) = Z \cdot b(\theta) \ where \ b = \begin{bmatrix} a(\theta) \\ a_b(\theta) \end{bmatrix} \ and \ Z = [Z_0 \, Z_b]$$

The figure D.1 shows the mutual coupling for the case of a five-element circular array and its supporting structure. Under this model, the extended mutual coupling matrix is given by:

$$Z_0 = \begin{bmatrix} 1 & \alpha & \beta & \beta & \alpha \\ \alpha & 1 & \alpha & \beta & \beta \\ \beta & \alpha & 1 & \alpha & \beta \\ \beta & \beta & \alpha & 1 & \alpha \\ \alpha & \beta & \beta & \alpha & 1 \end{bmatrix} \quad and \quad Z_b = \begin{bmatrix} \alpha_0 & \alpha' & \beta' & \beta' & \alpha' & \gamma \\ \alpha' & \alpha_0 & \alpha' & \beta' & \beta' & \gamma \\ \beta' & \alpha' & \alpha_0 & \alpha' & \beta' & \gamma \\ \beta' & \beta' & \alpha' & \alpha_0 & \alpha' & \gamma \\ \alpha' & \beta' & \beta' & \alpha' & \alpha_0 & \gamma \end{bmatrix}$$

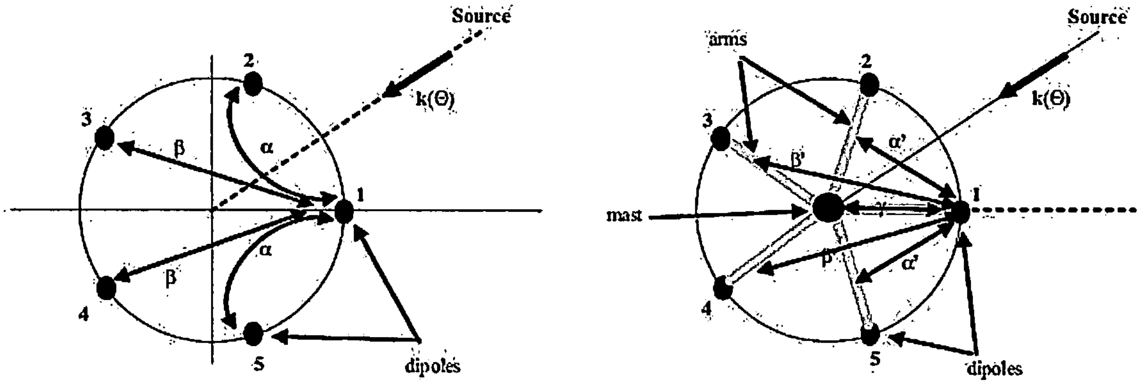

Figure D.1: Mutual coupling in the case of a five-element UCA. Coupling between the array elements and suporting structure.

Where Z_0 becomes a toeplitz matrix for a UCA, and Z_b a toeplitz matrix plus a column if the supporting structure is formed by a mast and one arm for each antenna. Moreover, it is clear that Z_0 depends only on two parameters, β, α and Z_b depends only on four parameters, α_0, α', β', γ. In fact, if vertical polarization is assumed, the mutual coupling of the structure depends only on γ.

Therefore, each row of the matrix Z can be rewritten as:

$$z_m^T = D_n \cdot c$$

Where

$$D_m = \begin{bmatrix} D_{0m} & 0 \\ 0 & D_{bm} \end{bmatrix} \quad and \quad c = \begin{bmatrix} c_0 \\ c_b \end{bmatrix}$$

$$c_0 = \begin{bmatrix} 1 \\ \alpha \\ \beta \end{bmatrix}, \; c_b = \gamma$$

And, for example:

$$D_{01} = \begin{bmatrix} 1 & 0 & 0 \\ 0 & 1 & 0 \\ 0 & 0 & 1 \\ 0 & 0 & 1 \\ 0 & 1 & 0 \end{bmatrix}, \quad D_b = 1$$

At this point, a model for the mutual coupling of a UCA has been described. The next step is the evaluation of the model parameters, that is to say, the vector $c = \begin{bmatrix} 1 & \alpha & \beta & \gamma \end{bmatrix}^T$. To this end, K pilot signals are employed. Thus, K, steering vectors, are measured: $a_e(\theta_i)$ with $1 \leq i \leq K$.

The relation between the measured vectors, $a_e(\theta)$, and the vectors estimated by the model, $\tilde{a}(\theta)$, is given by:

$$a_e(\theta) \approx \rho \cdot e^{j\varphi} \cdot \tilde{a}(\theta)$$
$$a_{em}(\theta) \approx \rho \cdot e^{j\varphi} \cdot z_m \cdot b(\theta)$$

Where ρ and φ are the amplitude and phase ambiguity respectively. Defining $c' = \rho \cdot e^{j\varphi} \cdot c$, the previous relatino becomes:

$$a_{em}(\theta) \approx t_m^T \cdot c' \;\; where \;\; t_m^T = b(\theta)^T \cdot D_n$$

Since the expression of t_n^T is analytical, and $a_{em}(\theta)$ is provided by the calibration process, the problem of finding the coupling parameters, c', can be solve as a minimization problem:

$$\hat{c'} = \underset{c}{\arg\min} \left\{ \sum_{m=1}^{M} \sum_{i=1}^{K} \left| t_m^T(\theta_i) \cdot c - a_{em}(\theta_i) \right| \right\}$$

The solution to the previous equation is:

$$\hat{c'} = (Q^\dagger Q)^{-1} Q^\dagger q$$

$$Q = \begin{bmatrix} T(\theta_1) \\ \vdots \\ T(\theta_K) \end{bmatrix} \quad where \quad T(\theta) = \begin{bmatrix} t_1^T(\theta) \\ \vdots \\ t_N^T(\theta) \end{bmatrix}$$

$$q = \begin{bmatrix} a_e(\theta_1) \\ \vdots \\ a_e(\theta_K) \end{bmatrix}$$

D.3 Calibration based on cost function minimization

As introduced in the chapter 4, some calibration techniques are based on the measurement of some actual steering vectors and the estimation of the mutual coupling matrix and/or the actual antenna characteristics via a minimization process. The method described here was introduced by See in 1996.[47]

In this technique, the mutual coupling and error in the antenna characteristics is modelled by a mutual coupling matrix M and the actual vector positions ψ. Thus, each of the measured steering vectors will follow:

$$a_m(\theta) = M \cdot a(\psi, \theta) + n_i$$

Where, n_i is the noise component, and it is assumed to have Gaussian distribution with zero mean, and covariance $\varsigma^2 I$. If the number of calibration sources is N, then the probability density function of the set of measured steering vectors corresponding to these N temporally disjoint sources at calibration angles $\theta = [\theta_1, \dots, \theta_N]$ will be:

$$p(a_m(\theta_1), \dots, a_m(\theta_N) \mid M, \psi, \sigma^2) = \left(\pi\varsigma^2\right) \cdot exp\left\{-\frac{1}{\varsigma^2} \sum_{i=1}^{N} \|a_m(\theta_i) - M \cdot a(\psi, \theta_i)\|^2\right\}$$

It can be shown that the maximum likelihood estimates (MLE) of M and ψ are the corresponding values that minimize the following cost function:

$$\hat{M}, \hat{\psi} = \underset{M,\psi}{^{arg\,min}} \|M \cdot A(\psi) - A_m\|_F^2$$

Where $A_m \triangleq [a_m(\theta_1), \dots, a_m(\theta_N)]$ and $A \triangleq [a(\theta_1), \dots, a(\theta_N)]$.

Assuming that $A(\psi)$ is of full rank and the identfiability of the problem, it is possible to minimize the cost function with respect to M, leaving ψ constant:

$$\hat{M} = A_m \cdot A^*(\psi) \cdot (A(\psi) \cdot A^*(\psi))^{-1}$$

Thus, the minimization problem is transformed in the following problem:

$$\hat{\psi} = \underset{\psi}{^{arg\,min}} Tr(P^{\perp} \cdot A_m^* \cdot A_m) = \underset{\psi}{^{arg\,min}} f(\psi)$$

This minimization problem can be solve iterative using a damped Newton method. Although, $f(\psi)$ is likely to have many local minima, if the first values of $\hat{\psi}$are close to the actual values, the estimatino will succeed. Therefore, it is possible to estimate iteratively $\hat{\psi}$, and the use this value to estimate M.

The first values of $\hat{\psi}$ are its nominal values, and it is updated in each iteration by:

$$\hat{\psi}_{k+1} = \hat{\psi}_k - \mu_k \cdot H_k^{-1} g_k$$

Where μ_k is equal to 0.5^p, and p is the smallest interger that fulfilles $f(\hat{\psi}_{k+1}) < f(\hat{\psi}_k)$. And g_k and H_k are the gradient and Hessian of $f(\hat{\psi}_k)$ respectively.

$$g = -2 \cdot Re \left\{ \begin{array}{c} vecd(A_x P^{\perp} A_m^* A_m A^* (A \cdot A^*)^{-1}) \\ vecd(A_y P^{\perp} A_m^* A_m A^* (A \cdot A^*)^{-1} \end{array} \right\}$$

$$H = 2 \cdot Re \left\{ D \cdot P^{\perp} \cdot D^{*} \odot (1_{2x2} \otimes \Xi)^{T} \right\}$$

$$D = \left[A_x^T \, A_y^T \right]^T$$

$$\Xi = (A \cdot A^{*})^{-1} A \cdot A_m^{*} A_m A^{*} (A \cdot A^{*})^{-1}$$

$$A_x = jkA \cdot \Lambda_{sin}, \quad A_y = jkA \cdot \Lambda_{cos} \quad where \quad \Lambda_{sin} = diag[sin(\theta_1), \ldots, sin(\theta_N)]^T$$

Bibliography

[1] www.cst.com Computer Simulation Technology webpage.

[2] CST User´s guide.

[3] Weiland, T.: A discretization method for the solution of Maxwell's equations for six-component fields. International Journal of Electronics and Communication AEU 31 (1977) 116–120

[4] Weiland T. , "On the Calculation of Eddy Current in Arbitrarily Shaped, Three Dimensional, Laminated Iron Cores, Part I The Method," Archiv für Elektrotechnik (AfE), vol. 60, p. 345, 1978.

[5] Weiland, T., "On the unique numerical solution of Maxwellian eigenvalue problems in three dimensions," Particle Accelerators, Vol. 17, 227–242, 1985.

[6] Weiland,T. "Time Domain Electromagnetic Field Computation with Finite Difference Methods," International Journal of Numerical Modelling, Vol. 9, pp. 295-319 (1996).

[7] Thoma, P. and T. Weiland, "Numerical stability of finite difference time domain methods," IEEE Transactions on Magnetics, Vol. 34, No. 5, 2740–2743, 1998.

[4] Richard Courant. " Lectures on the Mathematica Theory of Wave Propagation".

[5] R.F. Harrington. Field computation by Method of Moments. MacMillan, 1993.

[6] Alexander Hrennikoff. "Solution of problems of elasticity by the framework method". ASME J. Appl. March, 8, 1941.

[7] G. P. Nikishkov "Introduction to the finite element method"

[8] Schuhmann, R. and T. Weiland, "Conservation of discrete energy and related laws in the finite integration technique,"

[14] Kane Yee. "Numerical solution of initial boundary value problems involving Maxwell's equations in isotropic media" Antennas and propagation, IEEE Transactions on 14: 302-307

[15] Zienkiewicz, O. C., "A new look at the Newmark, Houbolt and other time stepping formulas. A weighted residual approach," Earthquake Engineering and Structural Dynamics, No. 5, 413–418, 1977.

[16] Zienkiewicz, O. C., W. L. Wood, N. H. Hine, and R. L. Taylor, "A unified set of single step algorithms; part 1," Int. J. for Num. Meth. in Eng., Vol. 20, 1529–1552, 1984.

[8] H.G. Schantz, "Planar elliptical element UWB dipole antenna", in IEEE APS, 2002.

[9] H.G. Schantz, "Bottom fed planar elliptical UWB antennas", Ultra Wideband Systems and Technologies, 2003 IEEE Conference on.

[10] H.G. Schantz, "The art and the science of ultrawideband antenna", Boston: Artech House, 2005.

[11] Narayan Prasad Agrawall, Girish Kumar, and K. P. Ray, “Wide-Band Planar Monopole Antennas” in IEEE Transactions on antennas and propagation, VOL. 46, NO. 2, FEBRUARY 1998

[12] C. A. Balanis, “Antenna Theory: Analysis and Design”. New York: Harper and Row, 1982.

[13] A. V. Vorobyov, A. G. Yarovoy, B. Yang, L.P. Ligthart, "Cavity – Backed UWB Antenna for Impulse Radio", submitted to IEEE TAP.

[14] Zhongfu Ye and Chao Liu, “2-D DOA Estimation in the Presence of Mutual Coupling”, IEEE Transactions on antennas and propagation, VOL. 56, NO. 10, OCTOBER 2008

[15] Anne Ferreol, Eric Boyer, Pascal Larzabal, Martin Haardt, “On the introduction of an extended coupling matrix for a 2D bearing estimation with an experimental RF system”.

[16] Andrian Andaya Lestari, Alexander G. Yarovoy, and Leo P. Ligthart, “RC-Loaded Bow-Tie Antenna for Improved Pulse Radiation”. IEEE Transactions on antennas and propagation, VOL. 52, NO. 10, OCTOBER 2004

[17] A. Lestari, A. G. Yarovoy, L. P. Ligthart, “Analysis of RC Loading Profiles for Antenna Bandwidth Improvement “ ,Antennas and Propagation Society International Symposium, 2003. IEEE

[12] Nicoláos G. Alexópoulos, and David R. Jackson. “Fundamental Superstrate (Cover) Effects on Printed Circuit Antennas”. IEEE Transactions on antennas and propagation, VOL. AP-32, NO. 8, AUGUST 1984

[13] A. Bhattacharyya and T. Tralman. “Effects of the dielectric superstrate on patch antennas”. Electronic letters VOL. 24 NO. 6 17th March 1988

[14] David R. Jackson and Nicoláos G. Alexópoulos. “Gain Enhancement Methods for Printed Circuit Antennas”. IEEE Transactions on antennas and propagation VOL. AP-33, NO. 9, SEPTEMBER 1985.

[15] Günter Kompa, “Practical Microstrip design and applications”, 2005 Artech House.

[16] David M. Pozar, “Microwave engineering”, Wyley & Sons

[17] Ralph 0. Schmidt. “Multiple Emitter Location and Signal Parameter Estimation”. IEEE Transactions on antennas and propagation, VOL. AP-34, NO. 3, March 1986.

[18] B. Friedlander. ”A Sensitivity Analysis of the MUSIC Algorithm” IEEE Transactions on Acoustics. Speech, and Signal Processing. VOL 38. NO. IO. October 1990.

[19] T. Gebauer and H. G. Gockler. “Channel-individual adaptive beamforming for mobile satellite communications” . IEEE J. Selected Areas Comm., 13, 439-48, 1995.

[20] R. W. Klukas and M. Fattouche. “Radio signal Direction Finding in the Urban Radio Environment”. Proceeding National Technical Meeting of the Institute of Navigation, 1993, pp. 151-160.

[21] J. Lo, L. Stanley , Jr. Marple. ”Observability Conditions for Multiple Signal Direction Finding and Array Sensor Localization”. IEEE Transactions on signal processing, VOL. 40, NO I I . November 1992.

[22] M. Gavish and A. J. Weiss. “Array Geometry for Ambiguity Resolution in Direction Finding” . IEEE Transactions on antenna and propagation, VOL. 44, NO. 6, June 1996.

[23] F. Athley, C. Engdahl, P. Sunnergren. ”On Radar Detection and Direction Finding using Sparse Arrays“. IEEE Transaction on aerospace and electronic systems.VOL. 43, NO. 4 October 2007.

[24] W. Xiao, X-C. Xiao, H-M Tai. ”Rank-1 DOA estimation of circular array with fewer sensors”.

[25] K-C. Tan, S. S. Goh and E-C. Tan. “A Study of the Rank-Ambiguity Issues in Direction-of-Arrival Estimation”. IEEE Transactions on signals processing, VOL. 44, NO. 4, April 1996.

[26] Y. Hua and T.K. Sarkar. "Matrix Pencil method for estimating parameters of exponentially damped/undamped sinusoids in noise". IEEE Transactions on acoustics. Speech, and Signal Processing. VOL 38. NO. 5. October 1990.

[27] N. Yilmazer, J. Koh, and T. K. Sarkar. "Utilization of a Unitary Transform for Efficient Computation in the Matrix Pencil Method to Find the Direction of Arrival" IEEE Transactions on antenna and propagation VOL. 54, NO. 1, January 2006.

[28] K. Takao and N. Kikuma. "An Adaptive Array Utilizing an Adaptive Spatial Averaging Technique for Multipath Environments". IEEE Transactions on antenna and propagation, VOL. AP-35, NO. 12, December 1987.

[29] M. Grice, J. Rodenkirch, A. Yakovlev, H. K. Hwang, Z. Aliyazicioglu, A. Lee. "Direction of Arrival Estimation using Advanced Signal Processing". IEEE 2007.

[30] L. C. Godara, Smart antennas (CRC Press LLC, 2004, 342-374).

[31] A. Ferréol, P. Larzabal and M. Viberg". On the Asymptotic Performance Analysis of Subspace DOA Estimation in the Presence of Modeling Errors: Case of MUSIC". IEEE Transactions on signal processing, VOL. 54, NO. 3, March 2006.

[32] C. Qi, Y. Wang, Y. Zhang, and Y. Han. "Spatial Difference Smoothing for DOA Estimation of Coherent Signals". IEEE Signal Processing Letters, VOL. 12, NO. 11, November 2005

[33] T-J. Shan, M. Wax and T. KAILATH. "On Spatial Smoothing for Direction-of-Arrival Estimation of Coherent Signals". IEEE Transactions on Acoustic, Speech and Signal Processing. VOL. ASSP-33, NO. 4, August 1985.

[34] N. Tayem and M. Naraghi-Pour "A Unitary MUSIC-Like Algorithm for Coherent Sources". IEEE Vehicular Technology Conference, 2007.

[35] K. Kaneko and A. Sano. "MUSIC-like iterative DOA estimation in multipath environments". IEEE Sensor Array and Multichannel Signal Processing Workshop, 2008.

[36] Monika Agrawal, Kah-Chye Tan. "Higher rank ambiguity for star arrays". 2004

[37] H. Wang, M. Kaveh. "Coherent signal-subspace processing for the detection and estimation of angles of arrival of multiple wide-band sources", IEEE Trans. Acoust. Speech Signal Process. 33 August 1985.

[38] H. Hung, M. Kaveh. "Focussing matrices for coherent signal-subspace processing". IEEE Trans. Acoust. Speech Signal Process. August 1988.

[39] M.A. Doron, A.J. Weiss. "On focusing matrices for wideband array processing". IEEE Trans. Signal Process. 40. June 1992.

[40] H.-S. Hung, C.-Y. Mao. "Robust coherent signal-subspace processing for directions-of-arrival estimation of wideband sources". IEE Proceedings of Radar, Sonar and Navigation. October 1994.

[41] Ta-Sung Lee, "Efficient wideband source localization using beamforming invariance technique". IEEE Trans. Signal Process. 42. June 1994.

[42] Fabrizio Sellone. "Robust auto-focusing wideband DOA estimation". April 2005.

[43] Jinliang Cao, Zhiwen Liu, and Yougen Xu. "New Algorithm Requiring No Preprocessing for Wideband DOA Estimation" IEEE ICSP2008 Proceedings.

[44] S. Valaee and B. Champagne, "Localization of wideband signals using least-squares and total leastsquares approaches," IEEE Trans. Signal Processing, vol. 47, no. 5, May 1999.

[45] Shoko Araki, Hiroshi Sawada, Ryo Mukai and Shoji Makino. "DOA estimation for multiple sparse sources with normalized observation vector clustering". ICASSP 2006.

[46] J. Pierre and M. Kaveh, "Experimental performance of calibration and direction-finding algorithms," in Proc. IEEE Conference on Acoustics, Speech, and Signal Processing (ICASSP), 1991, pp. 1365-1368.

[47] Boon Chong Ng, and Chong. "Meng Samson See Sensor-Array Calibration Using a Maximum-Likelihood Approach". IEEE Transactions on Antennas and Propagation, VOL. 44, No. 6, June 1996.

[48] K. Pensel, H. Aroudaki, and lA. Nossek, "Calibration of smart antennas in a GSM network," in Proc. Signal Processing Advances in Wireless Communications (SPAWC), 1999.

[49] Andreas Kortke, "A new calibration algorithm for smart antenna arrays," in Proc. Vehicular Technology Conference, Apr. 2003.

[50] Tao Su, Kapil Dandekar, and Hao Ling. "Simulation of mutual coupling effect in circular arrays for Direction-Finding applications". IEEE Microwave and Optical Letters. Vol 26, No. 5. September 2000.

[51] Konstantinos V. Stavropoulos and Athanassios Manikas. "Array calibration in the presence of unknown sensor characteristics and mutual coupling". 2000.

[52] Anne Ferreól, Eric Boyerb, Pascal Larzabal, Martin Haardt "On the introduction of an extended coupling matrix for a 2D bearing estimation with an experimental RF system". September 2007

[53] Maria Lanne, Astrid Lundgren and Mats Viberg. "Calibrating and Array with Scan Dependent Errors Using a Sparse Grid". IEEE Conference on Signals, Systems and Computers, October 2006.

[54] Min Lin and Luxi Yang. "Blind Calibration and DOA Estimation With Uniform Circular Arrays in the Presence of Mutual Coupling" IEEE Antennas and Wireless Propagation Letters, VOL. 5, 2006.

[55] De-yuan Gao, Bu-hong Wang, and Ying Guo. Comments on "Blind Calibration and DOA Estimation With Uniform Circular Arrays in the Presence of Mutual Coupling". IEEE Antennas and Wireless Propagation Letters, VOL. 5, 2006 566

[56] Min Lin and Luxi Yang Reply to the Comments on "Blind Calibration and DOA Estimation With Uniform Circular Arrays in the Presence of Mutual Coupling" IEEE Antennas and Wireless Propagation Letters, VOL. 5, 2006 568

[57] Yuhei Shimada, Hiroyoshi Yamada and Yoshio Yamaguchi. "Blind Array Calibration Technique for Uniform Linear Array Using ICA"

[58] Takeshi Amishima, Atsushi Okamura, Shinichi Morita and Tetsuo Kirimoto. "Tracking Based ICA Permutation and its Experiment on Blind Radio Source Separation". Proceedings of the 5th European Radar Conference.

[59] A.Manikas, A.Alexiou, and H.R. Karimi. "Comparison of the ultimate direction-finding capabilities of a number of planar array geometries" Radar, Sonar and Navigation, IEE Proceedings. Dec 1997.